GLOW DISCHARGE CHARACTERISTICS OF NON-THERMAL MICROPLASMAS AT ABOVE ATMOSPHERIC PRESSURES AND THEIR APPLICATIONS IN MICROSCALE PLASMA TRANSISTORS

A Thesis

by

DANI GHASSAN WAKIM

Submitted to the Office of Graduate Studies of
Texas A&M University
in partial fulfillment of the requirement for the degree of

MASTER OF SCIENCE

Chair of Committee,	David Staack
Committee Members,	Debjyoti Banerjee
	Harlan Harris
Head of Department,	Andreas Polycarpou

August 2013

Major Subject: Mechanical Engineering

ABSTRACT

A microscale plasma transistor capable of high speed switching was manufactured using microfabrication techniques and operated using microplasma discharges. Such a device has feature sizes on the order of 25 μm, is robust against spikes in power, high temperatures, as well as electromagnetic interference and capable of low cost production through microfabrication. In this work two aspects of the Microscale Plasma Device development were investigated; (1) the microplasma properties and (2) the manufacturing of the MPD.

To study the required plasma discharges and develop them to become better suited for the task at hand, Direct Current (DC) plasma discharge characteristics were investigated under pressures from atmospheric to 1.65 MPa while varying current from 0.1 mA to 4.5 mA and gap length from 5 μm up to 250 μm. This testing was carried out in a high pressure test chamber fitted with a micrometer for variable electrode spacing and gas inlets and outlets for varying the working gas and pressure. Voltage and current measurements along with microscopic imaging and optical emission spectroscopy were taken for discharges in the varying gases to determine discharge V-I characteristics, sizes and temperatures. Data gathered was used to understand the microdischarge characteristics and tailor the plasma for application in the microtransistor. Discharges with diameters as small as 7 μm have been achieved in Nitrogen and 16.7 μm in Helium by operating at low current, 0.5mA, and at pressures of 1.65 MPa and 0.34 MPa respectively. Paschen type, Pd, scaling is observed both in breakdown voltages, steady state voltage, and discharge size from 0.1 MPa to 1.65 MPa. The discharges operated in

a normal glow regime with near constant normalized current densities and relatively flat voltage current characteristics indicating normal glow discharge behavior in the microplasmas.

During device development small diameter metal wires, 25 μm and 50 μm, were used to carry out experiments on the microscale device to aid in electrode and substrate material selection. Robust electrode and substrate materials were required to withstand high discharge temperatures in order to prolong the device life time. As material selection was narrowed down microfabrication techniques were utilized to achieve smaller electrode geometry and electrode gap spacing with greater consistency. Photolithography coupled with thin film deposition using metal evaporation and electroplating resulted in electrodes with features and electrode gap spacing on the order of 25 μm and film thicknesses of 35 μm. Aluminum, Nickel, Copper and Titanium were deposited onto Alumina (Al_2O_3) and Ceria Stabilized Zirconia (CSZ) ceramic substrates, where only the latter two electrode materials proved to be robust enough to withstand the discharge temperatures. Superficial oxide layers on the electrode surfaces provided a protective coating, prolonging electrode lifetime in atmospheric air from 360 seconds to greater than 400 seconds without metal evaporation occurring. The oxide coating also acted as a dielectric barrier and increasing the resistance of the electrode surfaces to the order of 300 MΩ in some cases thus acting as a ballast resistance, compensating for stray capacitance and helped stabilize the plasma discharge.

ACKNOWLEDGEMENTS

First and foremost I must express my gratitude to my graduate advisor Dr. David Staack, whose brilliance in the topic coupled with an incredible sense of enthusiasm and excitement towards the research was incredibly motivating. His hands on approach, commitment and encouragement made the research interesting and fun. The success of this research is largely due to his guidance throughout the past two years.

Furthermore, I must express my gratitude to my parents, siblings and girlfriend for their never ending love and constant support throughout the past years, it made all the difference.

I would also like to thank my fellow PEDL lab mates for all their help and support throughout this research and in classes. They made it possible to maintain a fun and professional working environment.

TABLE OF CONTENTS

Page

LIST OF TABLES

Page

LIST OF FIGURES

Page

1. INTRODUCTION

1.1 Introduction to Transistors

A transistor is an electronic device used to amplify and / or switch electrical signals as well as electrical power. Transistors are used in many electronic devices such as calculators, radios, cellular phones and computers amongst many other electronic devices in daily use [1]. Transistors came about initially as Vacuum Tube transistors resembling a light bulb in shape and comparable to that in structure and size. The advantages of these early vacuum tube transistors was their robust nature and reliability, yet vacuum tube transistors come with several disadvantages such as warm-up time requirements and relatively large sizes. Solid state transistors came along due to the high demands on faster switching frequencies. Solid State transistors are usually semiconductor devices, although they can be manufactured out of different materials, with at least three electrodes that can be connected to external circuits and act as amplifiers or switches [2]. Solid state transistors can achieve much higher switching frequencies making them advantageous over vacuum tube transistors. Moreover solid state transistors can be mass produced making them readily available and fairly inexpensive. They are however susceptible to spikes in voltages and current as well as electromagnetic interference thus rendering them not as robust as their vacuum tube counterparts. Devices with the ability to combine the advantages of both vacuum tube and solid state transistors while staying clear of their short comings are in demand, specifically in the case of this project, by the Department of Defense (DoD). A

Microscale Plasma Device (MPD) was fabricated to act as a microscale transistor using microplasma discharges for switching. Examples of various MPDs such as a microtransistor [3] and microscale devices used for the application of glow discharge optical emission spectroscopy [4,5] that have been modeled and fabricated in the past were looked at along with their various fabrication techniques [6-10]. Many of these MPDs have been used for glow discharge optical emission spectroscopy [4-6,11-15]. The microplasma transistor fabricated by Chen and Eden [3] utilizes a microhollow cavity constraining the discharge to a diameter of 500 μm. The glow discharge used in this device achieved electron densities of $10^{12}\ cm^{-3}$. Device fabrication techniques varied between the two microplasma transistors studies by Chen and Eden and studied in this thesis. Microglow discharge inducing devices such as the ones fabricated by Mitra *et al* and Hopwood *et al* are similar to the one studied in this thesis in in terms of fabrication techniques utilized, device features achieved and materials used for substrates and electrodes [6,7]. However differences in achieved current densities occur due to both microglow discharge devices were only able to achieve electron densities on the order of $10^{14} cm^{-3}$ at most.

Plasma discharges utilized in microscale devices must have small discharge sizes with high electron and energy densities while having fast switching frequencies, approaching 10GHz in the case of the microscale plasma transistor presented in this work. The microplasma devices will combine the high power and robust switching of the vacuum tube transistors with the small size and low manufacturing cost of the solid state transistors. In order to advance towards the goal of manufacturing and testing these

MPDs, several microfabrication techniques such as Photolithography and Vacuum Metal Evaporation were used in addition to parallel testing of the plasma discharges themselves in pressurized test chambers. Device substrate and electrode materials were tested with the goal of determining materials able to withstand high discharge temperatures while keeping electrode degradation at a minimum. Substrate materials were tested for robustness to high temperature while having high thermal conductivity and high electric resistances. High thermal and electrical conductivity as well as high melting points were the driving factors in finding a suitable electrode material.

1.2 Motivation and Thesis Statement

Microplasma transistors were first studied by integrating a controllable solid state electron emitter with a microplasma confined in a 500 μm diameter microcavity, Chen & Eden, 2008 [3]. The aim of this work is to design and manufacture a microscale plasma device that can be used for higher frequencies and higher current density while still being robust and capable of withstanding spikes in power and electromagnetic interference. Targeted frequencies of this transistor are on the order of 10 GHz, with device feature sizes on the order of 20 μm and charge carrier densities of $10^{18}\,1/cm^3$. Photolithography, metal evaporated thin film deposition and electroplating were used to fabricate the device features and electrode patterns [6,7]. In order to achieve these, the microscale plasma device operates in high pressure conditions up to 1.62 MPa, as tested. Shown in this work, operation under such high pressures allows for the attainment of microplasmas with glow like discharge characteristics [16-18] due to the nature of Paschen's scaling laws [19-25]. In the process of designing and manufacturing the

microscale plasma transistor, the characteristics of Glow Discharges under varying pressures and gases / gas mixtures were studied. Investigations were carried out pertaining to initiation of discharges and the ability to sustain them in higher than atmospheric pressures.

The purpose of this thesis is to present the work carried out towards manufacturing the microscale plasma transistor and investigating the nature of glow discharges in higher than atmospheric pressure for their application in such a device [6,7,26-28]. These microplasma Glow Discharges are characterized by their high energy densities and small discharges sizes [16,17,29], on the order of 10 μm in diameter, thus making them ideal for use in the microplasma transistor.

2. BACKGROUND AND LITERATURE REVIEW

2.1 What is Plasma

Plasma is a gas that exists in the fourth fundamental state of matter. Once a gas has enough energy added to it, by heating it, its molecules and / or atoms may be ionized and thus become charged [30,31]. Other methods of turning a gas into plasma are by applying a strong electromagnetic field [30,32]. Plasmas are comprised of positively charged ions, negatively charged electrons and neutrals and fall under several categories according to their size, temperature, and electrical characteristics. Plasmas are generally classified as Thermal or Non-Thermal Plasma. Thermal and Non-Thermal Plasmas are classified by the temperatures of their electrons and the bulk gas, where Thermal Plasma exist with their electrons and gas in thermal equilibrium, while in Non-Thermal plasma, gas temperatures are much lower than electron temperatures [30]. Ionization degrees play a factor in the classification of Thermal and Non-Thermal Plasmas, where Thermal Plasmas are almost completely ionized while Non-Thermal Plasmas have a small fraction of ionization.

Plasma discharges are also grouped according to the ambient pressure they exist in, ranging from low (vacuum), to atmospheric and high pressure plasmas. Arcs, Coronas and Dielectric Barrier Discharges (DBDs) are typical types of atmospheric plasmas [30,32]. Arcs, such as lighting or arc welders, have high energy densities and are considered Thermal Plasmas with temperatures on the order of 10,000 K [30]. Coronas are Non-Thermal Plasmas and usually occur as high voltage leaks on sharp electrode

tips. Similar to Coronas, DBDs are non-thermal plasma induced by high voltages across short electrode spacing, where a nonconductive partition (dielectric barrier) stops the discharge from becoming an arc. In these non-thermal plasmas, electron temperature Te = 1000 K and the gas temperature Tgas = 300 K, an example of low pressure non-thermal plasmas are Glow discharges. These plasma discharges are generated by a direct current electric field between two conductive electrodes. Glow discharges are a commonly used plasma discharge and can be seen in application such as fluorescent lights. Under conditions of high electrode temperatures and increasing pressures, they will undergo a glow to arc transition accompanied with higher currents and lower voltages. Microplasmas are another classification of plasma discharges with sizes on the order of 10s-100s of micron and can exist as both Thermal and Non-Thermal Plasmas [26,30,32]. Glow discharges under certain conditions, achieved with the use of external circuits of high resistance, can be classified as microplasmas under high pressures [16,17,33,34].

2.1.1 Thermal and Non-Thermal Plasmas

2.1.1.1 Thermal Plasma

Electrons initially gain energy from an electric field and transfer a portion of that energy through collisions with the heavier particles, ions and neutrals, in the plasma. If a sufficient number of collisions take place and energy is transferred, a local thermal equilibrium between the electrons and heavy particles will form [6,32]. Plasmas with electrons and heavy particles at thermal equilibrium are considered to be Thermal

Plasmas with temperatures usually ranging between 6000 K to 10000 K [30,32]. Thermal Plasmas usually have high ionization levels and are considered partially to fully ionized. A simple representation of Thermal Plasmas can be seen in the following temperature inequality, $T_e = T_{gas}$.

2.1.1.2 Non-Thermal Plasma

If plasma has not reached thermal equilibrium between the electrons and heavier particles due to insufficient time or insufficient energy, it is considered to be a Non-Thermal Plasma. In these plasmas, the electron temperature Te is much greater than the particle temperatures. Non-Thermal plasmas tend to have lower fractions of ionization and are thus considered to be weakly ionized [6,30,32]. The following inequality is simple summation of the temperature ranges for a Non-Thermal Plasma, $T_e > (T_{vib} = T_{elec}) > (T_{gas} = T_{rot})$.

2.1.2 Plasmas and Ambient Pressure

Many aspects of plasma discharges are determined by the environmental pressure. Ambient pressure plays a crucial role in affecting discharge temperature, energy densities, voltage current characteristics and discharge diameter [16-18,30,32,35,36]. Plasmas are usually categorized according to what pressure they most commonly occur in, such as Glow Discharges occurring in lower than atmospheric pressures. Studies of such classifications were carried out in the course of the project and the application of Glow Discharges in higher pressures for a microscale plasma device transistor was considered.

2.1.2.1 Paschen Scaling Laws

Direct Current Glow Discharges such as the ones utilized in the microscale plasma transistor generally occur at pressures well below atmospheric, on the order of 13 Pa to 130 Pa [33]. Operation at atmospheric pressures and above atmospheric pressures has been achieved, yet is susceptible to transitioning to an arc due to cathode heating [20,33]. The effects of pressure on plasma discharge are governed by Paschen's scaling law, describing the required voltage for breakdown to occur across a spark gap. Paschen's law states breakdown voltage is dependent upon the discharge gap length, the surrounding gas being operated in and the ambient pressure. Paschen's governing equation for breakdown voltage as a function of the product Pressure-Distance is expressed in equation 1 below.

$$V_{br} = \frac{B\,Pd}{\ln\left(\frac{A\,Pd}{ln(\frac{1}{\gamma}+1)}\right)} \quad (Eq\ 1)$$

In the above Paschen equation breakdown voltage V_{br} is a function of pressure P, electrode gap spacing d, γ is the secondary electron emission coefficient which depends on the cathode material and A and B which are constants specific to the gas composition [22,37]. The gas specific constants used in the Paschen equation can be seen in table 1 below with the resulting plot shown in figure 1 below.

Table 1: Gas dependent constants A and B for Paschen curve plotting [22]

Gas	A (1/Torr-cm)	B (1/Torr-cm)
Air	26.7	249.3
N2	9.3	230.6
H2	17.3	550.6
He	5.3	60
Ar	21.3	318

Paschen Curves plotted for Air, Hydrogen, Nitrogen, Helium and Argon are shown in figure 1 below using equation 1 and the gas constants given in table 1 above.

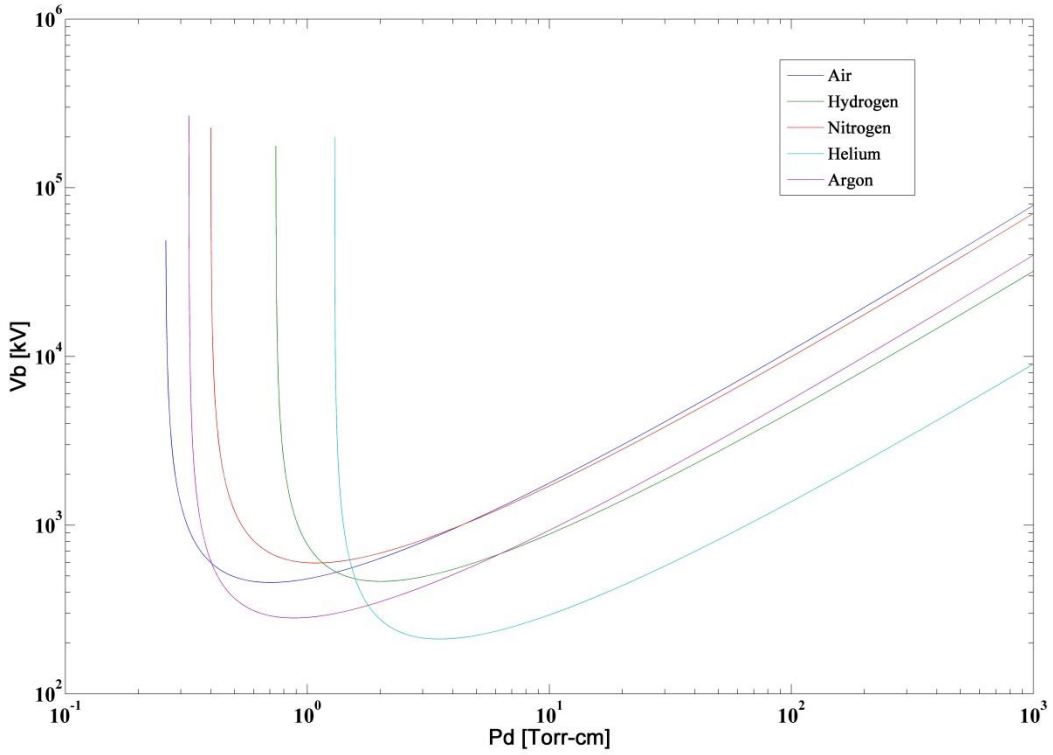

Figure 1: Paschen Curve Plots, Breakdown Voltage vs Pressure-Distance Air, Hydrogen, Nitrogen, Helium and Argon curves

Figure 1 above illustrated how increasing the ambient pressure increased the required voltage for breakdown at constant gap lengths in varying gases. A product of pressure and distance is used to obtain breakdown voltages. The product Pd is a non-dimensional parameter used due to being a simple representation of the particle density in the spark gap. Breakdown across the spark gap occurs due to Townsend breakdown mechanism that is a cascading avalanche of electrons. Once an electric field is applied across the spark gap, electrons are emitted from the cathode surface and travel towards the anode. As the applied voltage across the spark gap increases, the electrons traveling from the cathode to the anode gain enough energy to cause ionization and further release of electrons leading to the electron avalanche. Breakdown takes place and a Glow Discharge occurs when the applied voltage across the spark gap is sufficiently high, this minimum required voltage is referred to as the breakdown voltage. As the particle density increases due to an increase in pressure electrons traveling from the cathode to the anode across the spark gap will lose their energy due to an increased collision frequency. In order to have sufficient energy to cause further ionization and thus breakdown, the applied voltage across the spark gap must be increased.

The Pd parameter is a representation of the Knudsen Number Kn, shown in equation 2 below, which is the ratio of a particles mean free path to a characteristic length. For the application of Glow Discharge breakdown, the characteristic length is the electrode gap spacing d while λ, the mean free path, is the distance the electron will travel between collisions.

$$K_n = \frac{\lambda}{d} \quad (Eq\ 2)$$

This equation for the Knudsen number can be integrated into finding the Pd parameter used in Paschen scaling with the use of the ideal gas equation by following the steps in equations 3-5 leading to equation 6.

$$P = nK_bT \quad (Eq\ 3)$$

$$n = \frac{1}{\sigma\lambda} \quad (Eq\ 4)$$

$$Pd = nK_bT\ d = \frac{K_bT\ d}{\sigma\lambda} = \frac{K_bT}{\sigma}\frac{d}{\lambda} \quad (Eq\ 5)$$

$$Pd = \frac{K_bT}{\sigma}\frac{1}{K_n} = \frac{C}{K_n} \quad (Eq\ 6)$$

where K_b = Boltzmann's Constant, n = number of molecules, T = gas temperature and σ = collisional cross section swept by a particles traveling in space.

In order to have sufficient energy to ionize particles upon striking them the electron must have a sufficiently long mean free path, thus a low collision frequency. As pressure is increased the mean free path of the electron is decreased. The increased collision frequency dissipates the electrons energy thus lowering its ability to ionize gas particles. As can be seen in figure 1 above, there is an increase in breakdown voltage associated with shorter spark gaps. This is due to a large Knudsen Number, or in other words the electron mean free path is too long in comparison with the electrode gap spacing d. Each gas or gas combination has a specific E/N ratio, which is a constant value for Glow

Discharges. The E/N ratio is the ratio between the electric field, E, and the neutral particle density. The mean energy of electrons traveling across the spark gap is a function of E/N. In order to keep E/N constant as the gas density N increases, due to increasing pressure, the applied electric field E must also be increased by the same factor.

2.1.2.2 Low Pressure Plasmas

Low pressure plasmas, as the name suggests, occur at lower than atmospheric pressure. There is a wide array of plasma discharges that fall under the low pressure plasma category. Amongst low pressure plasma discharges are Glow Discharges. Low pressure plasmas have various commercial applications such as in cathode tubes, fluorescent and luminescent lighting [30,32].

2.1.2.3 Atmospheric Plasmas

Atmospheric plasmas are discharges that are usually known to occur at atmospheric pressures. Arcs, Coronas and Dielectric Barrier Discharges are all examples of atmospheric pressure plasmas [30,32]. Application of atmospheric pressure plasmas can be in metallurgy (melting metals), welding and surface treatments such as plasma spray coating, to name a few.

2.1.2.4 High Pressure Plasmas

Although uncommon, higher than atmospheric pressure plasma do occur. Pressure plays a strong role in determining a plasma discharge's characteristics such as V-I characteristics, discharge size and plasma temperatures [17,18,29,33]. As part of the

studies carried out in this thesis Glow Discharges, normally classified as lower than atmospheric pressure plasmas, were studied in higher than atmospheric pressures on the order of 10 MPa. These discharges will be studied while their characteristics and behaviors will be compared to conventional low pressure glow discharges.

2.1.3 Discharge Type

Plasma discharges fall under several categories depending on discharge energy, size, temperature and ambient pressures to name a few. Plasma discharges can be classified as Microplasma Discharges, Glow Discharges, Arcs and / or Sparks, Coronas or Dielectric Barrier Discharges (DBD) [30,32].

2.1.3.1 Microplasma

Microplasma discharges as so called due to their sizes, ranging from several micrometers to several thousand micrometers. Microplasma discharges can occur under varying pressures and in varying temperatures, thus they fir in both Thermal and Non-Thermal plasma categories. Ignition of microplasma discharges is governed by Paschen's law of breakdown [17-19,30].

2.1.3.2 Glow Discharge

A Glow Discharge is a luminous Non-Thermal plasma discharge [30,38] that can be generated by passing a current, with sufficient voltage, through a gas between a positively charged anode and a grounded or negatively charged cathode. A Glow Discharge consists of a negative glow at the cathode, a faraday dark space and a positive column. The dominant mechanism of electron emission in Glow Discharges is

secondary electron emission. Glow discharges conventionally operate at lower than atmospheric pressure but can occur at both atmospheric as well as high pressures.

2.1.3.3 Arcs and Sparks

An Arc discharge, such as lightning, is a type of thermal plasma that has industrial uses such as illumination and in metallurgy (used to melt metals and cut rocks). Arcs occur when current densities are very high and plasma and electrode temperatures rise. At this stage, the discharge moves from a Glow Regime to an Arc Discharge regime as the main mechanism of electron emission is Hot Cathode Thermionic Emission.

2.1.3.4 Corona

A corona discharge is a weakly luminous discharge, and in some cases not very visible to the naked eye. Coronas appear at atmospheric pressures near sharp electrodes or points where the electric field is very high. The electron emission mechanism in Coronas is secondary electron emission. Coronas appear in the Dark Discharge Regime.

2.1.3.5 Dielectric Barrier Discharge (DBD)

A Dielectric Barrier Discharge (DBD) is a plasma discharge that occurs between two conductive electrodes with one or more dielectric barriers located between the electrodes in the current path. DBDs are normally alternating current discharges at high voltages, although they can be achieved through the use of direct current. DBD often occur at atmospheric pressure.

2.1.4 What is a Microplasma

A Microplasma discharge, or microdischarge, is often regarded as a plasma discharge within a size of 1000 μm. Plasma size, diameter and length can be controlled by varying the ambient pressure the discharge takes place in and the electrode gap spacing. Microplasma discharges have numerous applications varying from commercial and industrial application to medical applications.

2.1.5 What is a Glow Discharge

A Glow Discharge is a type of stable self-sustaining luminous plasma discharge formed by passing current through a gas, normally at lower than atmospheric pressure [30,32]. A Glow Discharge occurs when a potential difference is applied between two metal or conductive electrodes where the current is typically higher than the threshold for Townsend breakdown. The breakdown voltage varies depending on ambient gas, ambient pressure, electrode gap spacing and electrode materials. As previously mentioned, the breakdown criteria of a glow discharge is governed by Paschen's law of breakdown. As an electric field is applied across the spark gap, positively charges ions will bombard the negatively charged cathode and release electrons. As electrons escape from the cathode surface they travel across the spark gap towards the anode. Depending on the electrons mean free path, the electrode gap spacing and the applied electric field, once the electron has enough energy it will ionize the gas particles upon collisions and release more electrons allowing an electron avalanche to take place. Once the applied external voltage has reached the minimum required breakdown voltage, breakdown takes

place and a Glow Discharge occurs. The Glow Discharge, as seen in figure 2 below, occurs between the positively charged Anode and the negatively charged Cathode.

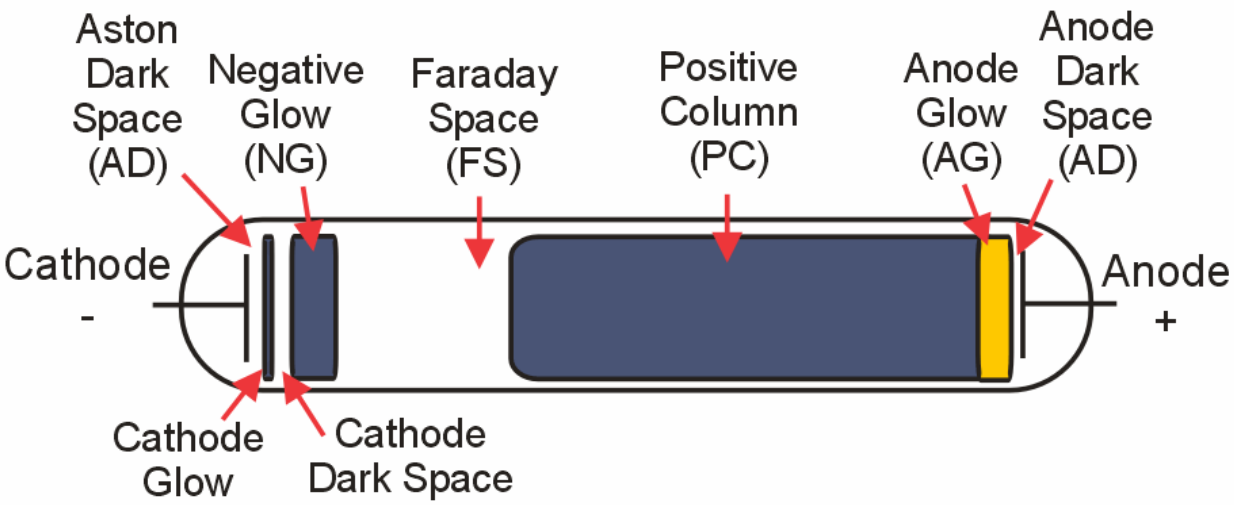

Figure 2: Glow discharge with highlighted features [38]

The typical Glow Discharge has features that are unique to it. Most noticeable of these features are the Negative Glow occurring over the cathode, the faraday Dark Space and a Positive Column. The positive column can sometimes be seen with noticeable striations. Glow Discharges are most commonly powered in a Direct Current (DC) mode. Direct currents were utilized since they are the simplest form of achieving a Glow Discharge and in order to maintain a constant cathode - anode configuration [30,39]. In Glow Discharges, voltage, current and the product of pressure and distance go hand in hand while only two can be controlled at a time while having the third parameter as a variable. Glow Discharges most commonly occur in lower than atmospheric pressures although in these studies they are achieved under high pressure. As pressure is increased electrode cooling methods may become necessary to reduce the transition from

secondary electron emission to hot cathode thermionic emission, causing the discharge to transition from a glow to an arc [6,20,34,40-43]. Glow Discharges were utilized in the microscale plasma transistor due to being widely studied and predictable, having the ability to achieve high electron and current densities and being able to occur as microplasma discharges under high pressure thus allowing for compact device design. Normal Glow Discharges occur at relatively low voltage of ~400-500 V with currents varying between $10^{-5}A\ to\ 10^{-2}A$. Throughout this current range the discharge voltage remains relatively constant and the discharge exists in the Normal Glow Regime. As current is increased beyond ~$10^{-2}A$, the discharge voltage will start to increase along with current and the discharge enters an Abnormal Glow Regime. An Abnormal Glow Discharge can also occur when the discharge diameter becomes on the order of the electrode diameters, since discharge diameter typically increases along with increasing current. Typical current densities of Glow Discharges range between $10^{8} - 10^{14}\ A/cm^{2}$ where the Glow Discharge utilized in the microscale plasma transistor presented in this thesis achieves current densities of $10^{18}\ A/cm^{2}$.

2.2 Modes of Excitation

For discharge to be able to self-sustain, it must have a constant supply of electrons usually coming from the electrodes [44,45]. There are three modes of supplying electrons to the plasma discharge, Secondary Electron Emission, Photoemission and Thermionic Electron Emission, the latter being the much more efficient process [6,20,40,41,46]. Electron emission modes depend upon plasma temperatures, thermal

equilibriums and operating pressure to name a few parameters that effect electron emission.

2.2.1 Secondary Emission

During the glow microdischarge regime electrons are supplied to the plasma discharge by secondary electron emission [6,34]. Electrons supplied via secondary electron emission come from the cathode surface. This mode of electron emission occurs when positively charged ions are accelerated through the space charge region and hit the cathode surface. Upon impacting the cathode, electrons are knocked off the surface. This mode of electron emission is favored at low pressure operating conditions where collision frequencies are lower [6,46].

2.2.2 Photoemission

During the photoemission process ultra violet photons, emitted from the discharge, cause electron emission from the cathode surface to occur due to photoelectric emission [6].

2.2.3 Thermionic Emission

The third source of electron emission occurs due to overheating of the cathode surface and causes the glow discharge to transition to an arc. During the cathode surface bombardment by positively charged ions the cathode surface temperature rises thus causing thermionic emission, also called field assisted thermionic emission [6,46]. Thermionic electron emission is a much more efficient process than secondary electron emission, thus Arc discharges are much more energy efficient discharge, however are

much higher in temperature due to attaining thermal equilibrium and higher degrees of ionization.

2.3 Glow-To-Arc Transition

Glow to Arc transitions occur due to the shift in mode of electron emission from secondary electron emission to thermionic electron emission. This shift in electron emission modes is caused by the heating of the cathode due to bombardment by positively charged ions [20,34,40,41,46].

3. EXPERIMENTAL SETUP

3.1 Chapter Summary

In order to experiment with the plasma discharges a testing chamber was assembled out of stainless steel sanitary fittings fitted with gas inlet and outlet ports, high-voltage wire, gate wire and ground wire ports, and viewing windows for spectroscopic data acquisition as well as ICCD photography. The test chamber allowed the experimental gases to be changed in order to gain a deeper understanding of how gas type affected the discharge characteristics such as size, breakdown and sustainability voltages and switching frequencies. In addition to varying the gases the chamber allowed pressure to be varied from atmospheric to 1.65 MPa allowing smaller discharge diameters to be achieved. The test chamber was equipped with a micrometer allowing the electrode gap length to be varied in increments of 5 μm. Figure 3 serves as an illustration of the test chamber used for varying gas, pressure and electrode spacing during plasma testing.

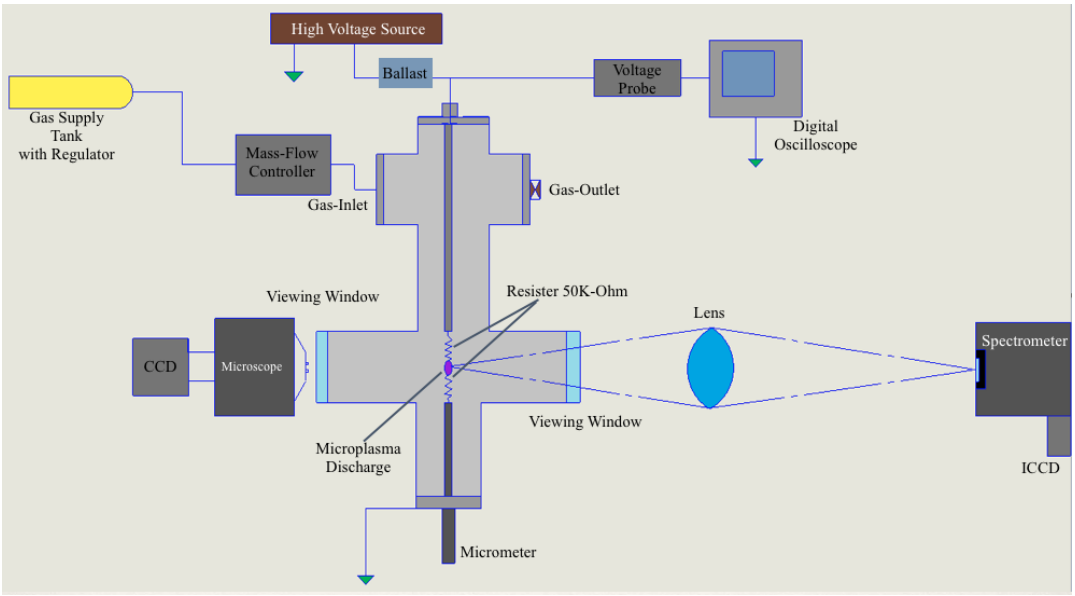

Figure 3: Complete chamber set-up overview

As can be seen in figure 3, an external circuit was connected to the test chamber in order to be able to achieve the desired stable discharges in addition to diagnostic purposes. A 2.1 MΩ ballast resistor was connected in series upstream of the plasma discharge in order to obtain a stable discharge and to compensate for stray capacitance that occurs due to the nature of the circuit itself. Additional 50 kΩ resistors were directly upstream and downstream of the discharge to further "combat" the stray capacitance. An ICCD camera mounted on a microscope along with a spectrometer were used to observe the plasma through viewing windows for diagnostics to obtain information such rotational and vibrational temperatures as well as discharge sizes. A digital oscilloscope along with a high voltage probe was used to get switching frequencies of the discharge

by obtaining voltage breakdown and current rise times. A current sensing resistor was integrated into the external circuit in order to obtain discharge voltages

3.2 External Circuit

In order to achieve the required plasma discharges an external circuit was used. A high voltage high current power supply capable of applying 5 mA and -20 kV was initially used. This was later replaced with a power supply capable of a 10 mA and 40 kV output. The output of the power supply was connected to a 2.1 MΩ ballast resistor, seen in figure 3 labeled as Rb, for power division, increased discharge stability and for compensating for stray capacitance. Stray capacitance that occurred due to the nature of the external circuit and was modeled into the external circuit and can be seen in figure 3 as "C" and highlighted in a light gray shade. The stray capacitance was dealt with by using shorter wires and by inserting a 50 kΩ resistor upstream and downstream of the discharge gap. Stray inductance also occurred due to the use of round wires and can be seen modeled as L1 and L2 in figure 4 below. Stray inductance in future work can be dealt with the use of flatter wires. A current sensing resistor was integrated into the external circuit, 500 MHz, in order to obtain the voltage with in the circuit and thus calculate the voltage drop across the discharge gap. A current transformer, 500 MHz, was also integrated into the circuit for diagnostic purposed. 10 kV and 6 kV voltage probes were hooked up to the circuit and connected to a LeCroy Waverunner Digital Oscilloscope for further diagnostics.

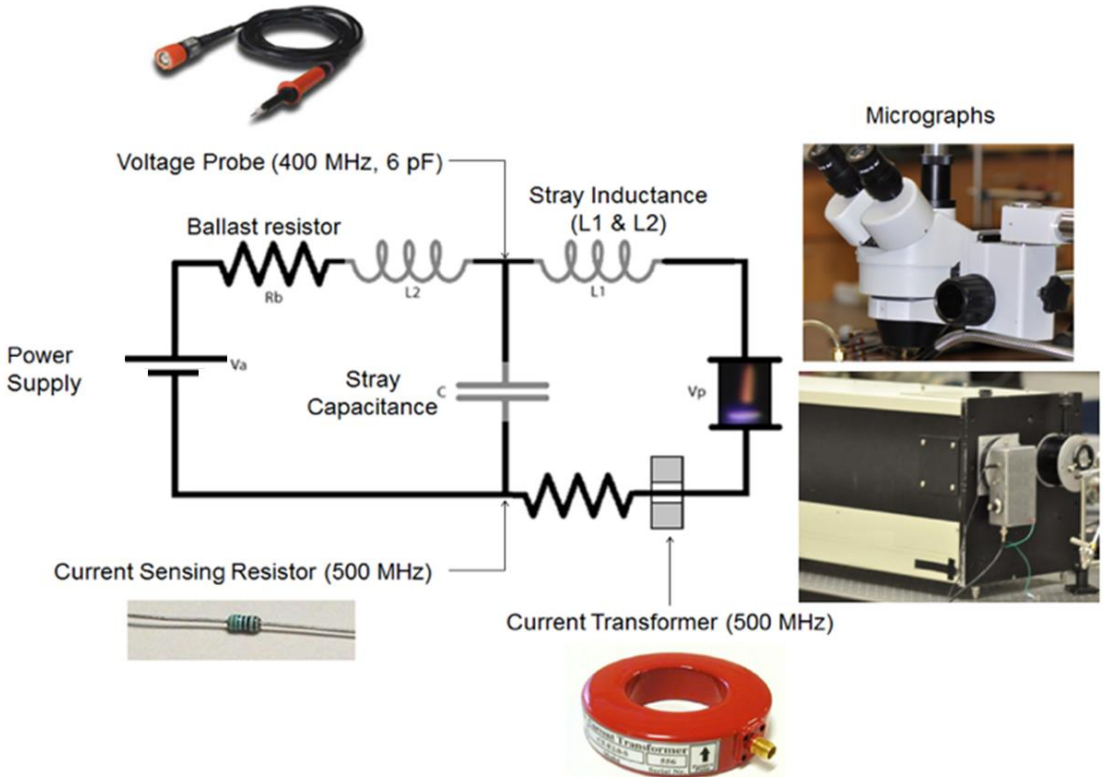

Figure 4: External circuit with ballast resistance, discharge gap, stray capacitance and stray inductance including diagnostic tools.

3.2.1 Controlling Stray Capacitance and Inductance

Capacitance is the ability of a body to store an electrical change, where any object that can be electrical charged can carry capacitance. Inductance occurs when change in current in an electrical conductor creates a voltage in the conductor itself an in nearby conductors. In the experimental setup, stray capacitance and stray inductance occurred due to the nature of the external circuit. Stray capacitance can cause signals to leak between circuits that are supposed to be isolated from one another and can be a limiting factor for the circuit to function properly.

3.2.2 Stable Discharge Inducing External Circuit

The components of the external circuit determine the stability of the plasma discharge occurring within the chamber or on the microscale plasma devices. In order to achieve discharge stability, high ballast resistance of 2.1 MΩ was included in the external circuit with an additional 50 kΩ resistors upstream and another 50 kΩ resistor downstream of the discharge. The inclusion of the 50 kΩ resistors was to compensate for stray capacitance that occurs due to the nature of the external circuit. In order to compensate for stray inductance, the use of flatter wires was suggested. This is still an aspect of the external circuit that may be dealt with in future work on the project.

3.2.3 Transient Discharge Inducing External Circuit

The external circuit for the transient discharge was very much the same as it was for the stable discharge. To take advantage of the external circuit's stray capacitance, the two 50 kΩ resistors upstream and downstream of the discharge gap were shorted. In order to increase the operators control on the capacitance in the circuit, 10 pF and 100 pF capacitors were individually inserted into the external circuit in parallel with the discharge gap. The value of the intentionally added capacitance to the circuit was greater than the stray capacitance and thus proved to be the dominating capacitance factor in the external circuit. The introduction of these capacitors allowed for the studying of the transient nature of the discharge, thus yielding a deeper understanding on achievable device switching frequencies.

3.3 Diagnostics

Diagnostics measures were taken to gain a deeper understanding of the nature of plasma discharge as well as the behavior of the external circuit and its effects on the discharge characteristics. External circuit diagnostics in addition to plasma discharge diagnostic techniques were used. Circuit diagnostics yielded information about the current and voltage of the electrical circuit. Optical Emission Spectroscopy (OES) along with the use of a Charge-Coupled Device (CCD) camera were used for plasma diagnostics. These tools were used due to being both non-invasive, thus not affecting the plasma discharge itself, and accurate ways of measuring discharge temperatures and sizes.

3.3.1 Plasma Diagnostics

Both a Charge-Coupled Device (CCD) cameras and an Intensified Charge-Coupled Device (ICCD) camera were used to measure discharge sizes. These cameras were mounted onto a microscope in order to obtain micrographs of the discharges. The micrographs were used to determine discharge gap spacing, sizes and diameters in addition to electrode degradation during experimentation. Optical Emission Spectroscopy (OES) readings were taken in order to obtain data regarding discharge temperatures and intensities. Results of the OES can be seen in the Effects of Gases on Microplasma Discharges chapter. Voltage-Current diagnostics were carried out by acquiring power supply voltage and current data in LabView. External circuit voltage and current data associated with the ballast resistor were also collected in LabView. The ballast resistor was factored out of data acquired from the power supply to yield the

Voltage-Current characteristics of the plasma discharge. Results of the V-I acquisition can be seen in the Effects of pressure on Microplasma Discharges chapter.

3.3.2 External Circuit Diagnostics

External circuit diagnostics were carried with the use of a current transfer and a current sensing resistor, both rated to 500 MHz. In addition a 10 kV and a 6 kV voltage probe were hooked up to the external circuit and connected to a digital oscilloscope. The use of the digital oscilloscope yielded external circuit voltage current measurements. Voltage drop off and current rise times were obtained with the use of the oscilloscope and used to obtain discharge switching and transients as well as giving an insight to discharge stability.

3.4 High Pressure Test Chamber

A high pressure test chamber was assembled out of stainless steel sanitary fitting. The test chamber was fitted with gas inlets and outlets allowing for both pressure and the ambient gas to be controlled. The gas inlet was used to control the type of gas and the ratio of gas mixtures the experiments were run in. The flow controllers were in part also used to control the pressure inside the test chamber. A needle valve was fitted on to the gas outlet to act as a pressure release valve. A stainless steel plate was welded to the inside of the chamber and the anode electrode was placed on a 1/4 inch thick acrylic platform which was then secured onto the stainless steel plate. The stainless steel nub anode was connected to the chamber with a 50 kΩ resistor. The chamber was then in turn grounded to a stainless steel top optical table. A hand made micrometer was inserted

into one of the chambers openings adjacent to the anode. The micrometer served as an adjustable cathode allowing for a variable electrode gap spacing capable of being adjusted in increments of 5 μm. The chamber was equipped with viewing windows allowing for micrographs and Optical Emission Spectroscopy (OES) to be taken of the plasma discharges.

3.4.1 Gas Control

Two Alicat flow controllers were used to control gas flow rates and gas combination ratios inside the test chamber, these flow meters can be seen in figure 5. This allowed for device testing to be conducted under varying gases and gas combination in order. Plasma characteristics such as breakdown voltages and discharge transients as well as electron and energy densities change according to what gas the environment consists of, thus the test chamber was filled with different gases in order to gain a further understanding of what gases and gas combination might be beneficial to achieving the targeted switching frequencies. On a materiel standpoint, plasma temperatures vary depending on what gas the discharge is in. With lower discharge temperatures, higher power discharges maybe achieved without overheating the device electrodes. In addition, inert gases decrease electrode oxidation and degradation thus increasing the device lifetime.

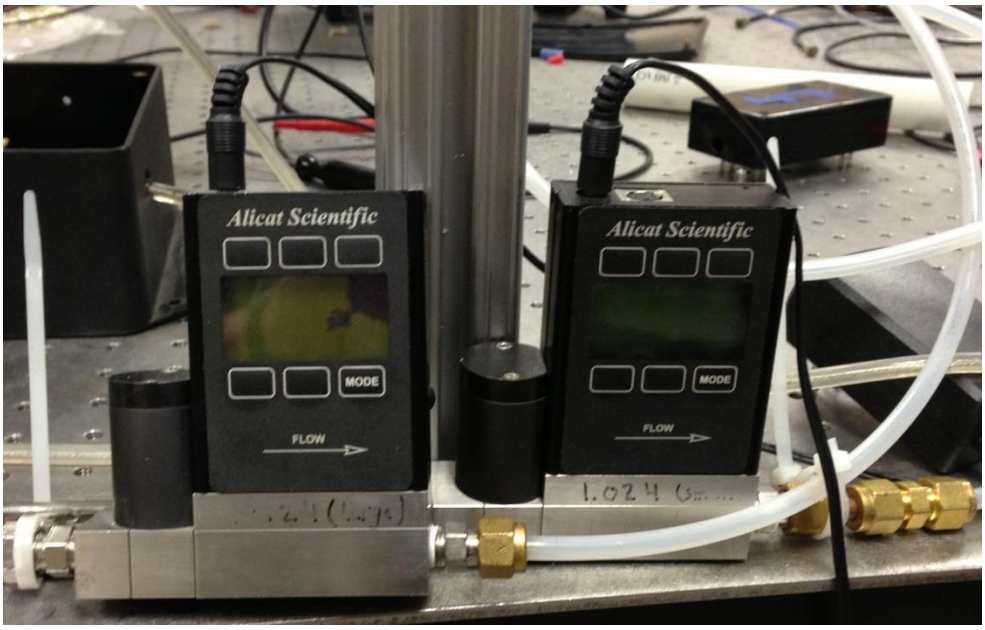

Figure 5: Alicat flow meter regulating gas flow rate and gas mixture ratios flow rate values are 10.24 SLPM and 1.024 SLPM

3.4.2 Pressure Control

To control pressure inside of the test chamber, the Alicat flow controllers shown in figure 5 above were used to control the gas flow rates in accordance with both the exit gas flow rate due to both the opening of the needle pressure release valve and leak rates that occurred due to the chamber not having perfect seals at its flanges. A gas outlet port was integrated into the high pressure test chamber and fitted with a needle valve in order to control the outlet gas flow rate. As inlet and outlet gas flow rates were controlled, so was the internal pressure of the test chamber.

3.4.3 Electrode Gap Spacing

The high pressure test chamber was fitted with a micrometer with an extension shaft acting as the cathode and a stationary 1/4 inch stainless steel nub acting as the anode. The micrometer was hand made from a stainless steel shaft with the use of a lathe and was given 40 threads per inch. With 40 threads per inch, every full revolution would change the electrode gap spacing by 635 μm. The end of the micrometer shaft was fitted with a nylon standoff which was in tern fitted with a stainless steel electrode tip. The nylon standoff caused the stainless steel electrode tip to be isolated and act as a floating electrode. This electrode tip, acting as the cathode, was then connected to the high voltage power supply with a 50 kΩ resistor used to compensate for stray capacitance. A radial dial was drawn in Solid Works with 127 increments and placed around the parameter of the micrometer shaft. As the micrometer was turned to change the electrode gap spacing, an indicator line was used by lining it up with the radial dials increments. This allowed electrode gap spacing to be changed in increments of 5 μm.

3.4.4 Microfabricated Device Test Chamber

The devices that were microfabricated using photolithography and thin film deposition were testing in an identical high pressure test chamber that was lacking a micrometer cathode and 1/4 inch stainless steel nub cathode. Since the electrodes were deposited right onto the substrate surface, the micrometer cathode and nub anode were not required as electrodes. A substrate testing clamp was made out of a machinable ceramic. The ceramic clamp was comprised of a bottom section with a recessed surface in the size and shape of the ceramic substrates and a top section to hold the ceramic

substrate in place. The two sections of the clamp were fastened together using small diameter non-conductive screws. The bottom section replaced the 1/4 inch thick acrylic originally under the anode nub and was fastened to the stainless steel plate that was welded into the inside of the test chamber. The top section of the clamp was machined to hold three aluminum electrode connections to connect to electrodes on the substrate surface and a central hole to view the discharge. Figure 6 below show the components of the ceramic clamp and how it was used to house the ceramic substrates with the deposited thin metal film electrodes.

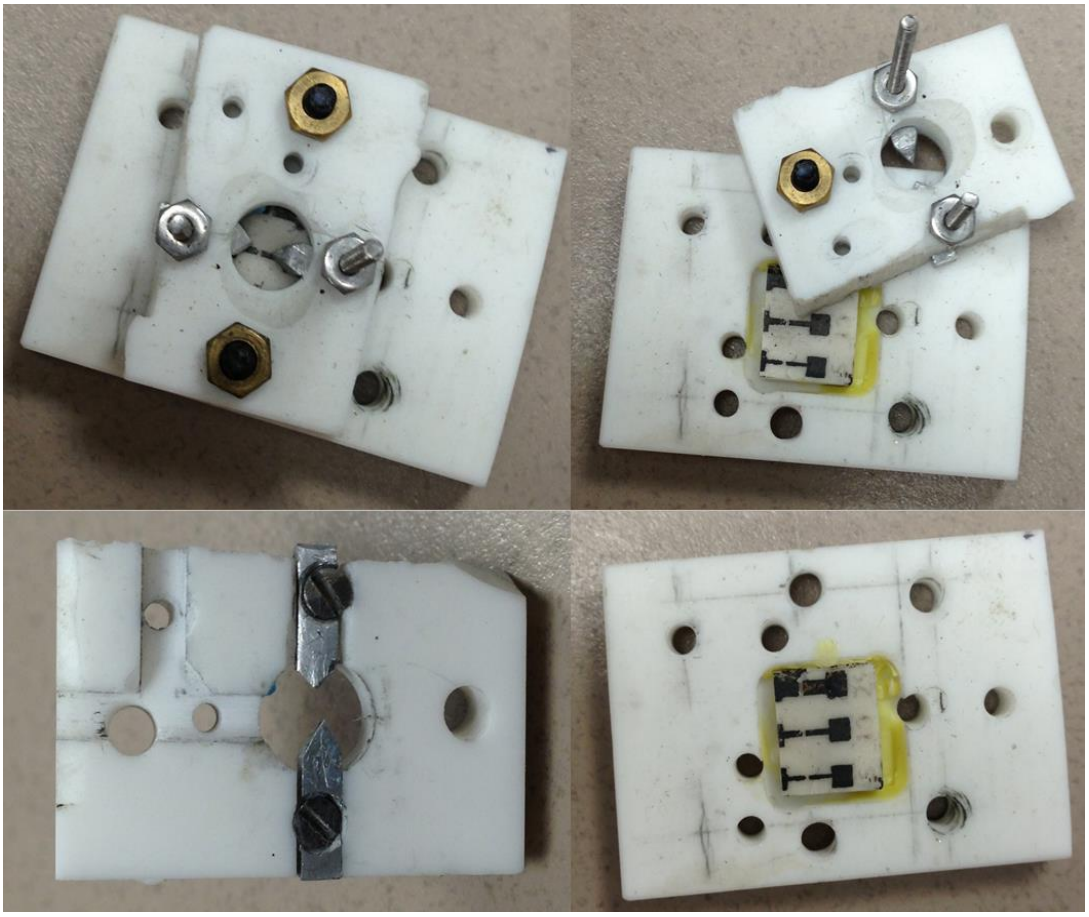

Figure 6: Microfabricated device on CSZ substrate with Copper-Copper Oxide electrodes housed in machinable ceramic clamp

4. DEVICE DEVELOPMENT AND EVOLUTION

4.1 Chapter Summary

In order to study both the plasma discharges and its characteristics along with the material requirements for manufacturing devices such as plasma transistors, several testing chambers were constructed. Substrate-electrode combinations were also made and tested in order to learn what substrate material worked best along with suitable electrode materials. Substrate materials were selected based upon melting points as well as electrical and thermal conductivity. The substrate had to be robust and able to withstand temperatures on the order of several thousand Kelvin yet it must not be electrically conductive to avoid current leaks through the substrate rather than through the plasma discharge. Aluminum Oxide (Alumina, Al_2O_3) was the initial choice to be used as a suitable substrate. With low electrical conductivity and a high melting point, Alumina was able to withstand the discharge temperatures. Initial testing for electrode material started off by using two 50 μm gold, silver, platinum and tungsten (Au, Ag, Pt, and W) wires. These wires were simply placed on the substrate surface at varying electrode gap lengths between 20 μm and 200 μm and held in place by Aluminum lead plates. The Aluminum plates served the purpose of holding the wires in place while acting as heat sinks to stop the electrodes from overheating. Early testing revealed that the wires over heated, evaporated and deposited material onto the substrate surface. In the three electrode configurations, a high voltage source electrode, a gate electrode and a grounded drain electrode were used to have control over the switching initiation and thus

frequencies. The gate electrode potential was on the order of half the potential of the source electrode and was controlled by opening and closing its circuit. The discharge initially occurred between the high voltage source and the gate and then proceeded to discharge to the drain as the circuit upstream of the gate is opened.

In parallel to the wire electrode experiments, photolithography and metal evaporation techniques were used to deposit metal electrodes onto the Alumina surface, as was the case in MPD fabricated by J. Hopwood [7] as an atmospheric-pressure microplasma source in air. Electrode patterns with varying geometries and electrode spacing were made using photolithography and Aluminum, Copper and Nickel were each evaporated onto the Alumina surface. Complications with mismatched coefficients of thermal expansion lead to the evaporated metals peeling off the Alumina substrate once certain thickness were achieved. Ceria Stabilized Zirconia ceramics were then selected as the new substrate material due to their high melting points, low electrical conductivity and better matched coefficient of thermal expansion. The metal evaporation coupled with photolithography method was continued with an emphasis on copper electrodes. Deposited electrode thicknesses of 800 nm to 1 μm were achieved yielding more robust electrodes. Copper was then oxidized to yield Copper-Copper Oxide electrodes. The oxide coated electrodes proved to be more robust to high power discharges due to the protective Copper Oxide layer. This outer oxide layer also served the purpose of providing a resistance that stabilized the discharge, due to dielectric properties of the oxide layer [42,47], and dealt with stray capacitance which occurred due to the nature of the external circuit. Three electrode configurations were achieved using the

photolithography and metal evaporation techniques in order to continue three electrode testing

4.2 Electrodes

The microscale plasma transistor device feature size was to be on the order of 1-20 μm. To achieve such feature sizes, device electrodes were on the same order of magnitude in size. In order to achieve a durable and robust microscale device, such small electrodes must have a high melting point to cope with high discharge temperatures, high thermal conductivity to help shed heat and minimize overheating of the electrode and a high electrical conductivity. Early testing to better understand the power loads of the plasma discharges did not put electrode size into consideration thus two stainless steel tips were used at electrodes. As electrode size was factored into the experiments the move to small diameter wires, 25 μm and 50 μm, was made using materials such as Ag, Au, Pd, W and eventually Pt-13%Rh due to a combination of favorable melting points, thermal and electrical conductivity. Testing with these small diameter wire electrodes consisted of manually orienting them in gaps varying between 10 μm to 100 μm apart in two and three electrode configurations. This was done in parallel with early metal evaporator deposition. Once geometric tolerances and configuration consistency of the two and three electrode configurations were limited due to the manual process of placing the wires by hand, photolithography and thin film deposition became the lead method of manufacturing the test devices. Changes to the metal evaporation process coupled with electroplating lead to thicker electrode. Thermally induced formation of superficial oxide layers enhanced durability of the electrode films.

4.2.1 Micrometer and Stainless Steel Anode

The high pressure test chamber was fitted with a floating, electrically isolated, 1/4 inch stainless steel nub that was polished to a mirror like finish in order to reduce surface roughness and make post experiment oxidation and degradation easy to find and identify. This stainless steel nub served as the cathode and was connected to ground. A sharp, ~15 μm diameter tip, stainless steel spring loaded and linearly displacing shaft was positioned by a micrometer and could be moved in increments of 5 μm in order to change electrode gap spacing. This shaft was connected to a high voltage negative power supply and acted as the cathode electrode. This configuration can be seen in figure 7 below.

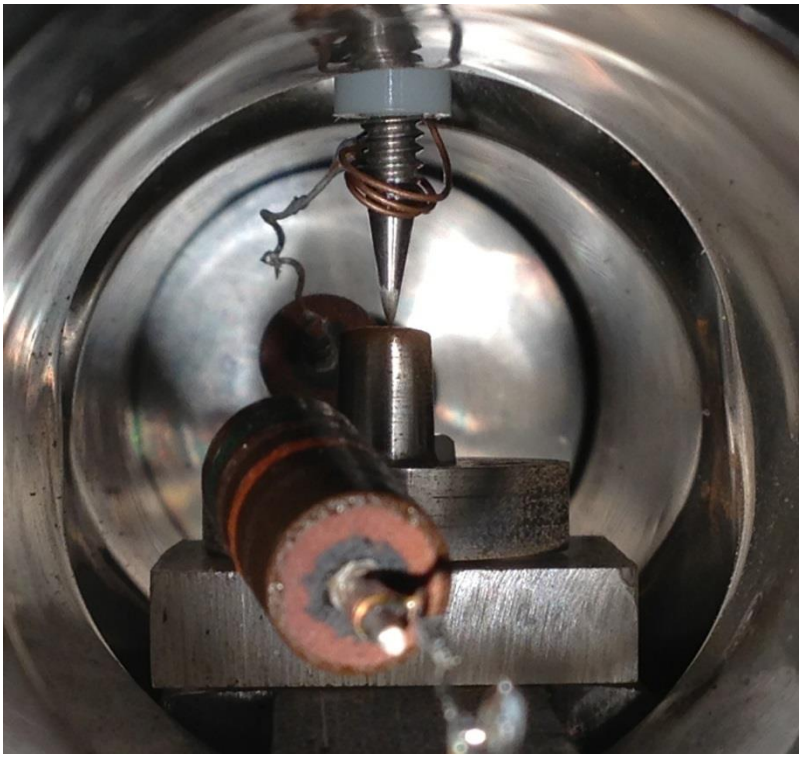

Figure 7: Micrometer mounted Cathode (top) with 50 kΩ resistor (top coil) with grounded anode (bottom) and 50 kΩ resistor (front)

4.2.2 Small Diameter Wire Electrodes

Small diameter wire electrode testing was conducted in order to gain an understanding of how microscale electrodes behave when exposed to high plasma temperatures and when coping with the discharge power demands. Initial testing started with the use of Pd electrodes due to Palladium's high thermal and electrical conductivity and relatively high melting point. The Palladium electrode was able to withstand testing with a current-voltage load of 1 mA and 2.5 kV. Tests with increased power, 1.5 mA and 3 kV, resulted in the electrodes overheating, evaporated and deposited onto the substrate surface [11,38]. As the electrode material overheated, evaporated and condensed on the substrate surface, electrode gap spacing was changed. An example of an experiment with Palladium wire resulting in material evaporation and increased gap spacing is given in figure 8 below. The two 50 μm diameter wire electrode setup was assembled by hand with an initial electrode gap spacing of 186 μm. After being exposed to a plasma discharge at 1.74 mA and 4 kV the anode began to overheat glowing bright yellow. After 200 seconds of testing, the plasma was switched off and the post discharge electrode gap spacing was 548 μm. These measurements were made through the use of a micrograph, where electrode gap spacing was verified through comparison with the electrode diameter.

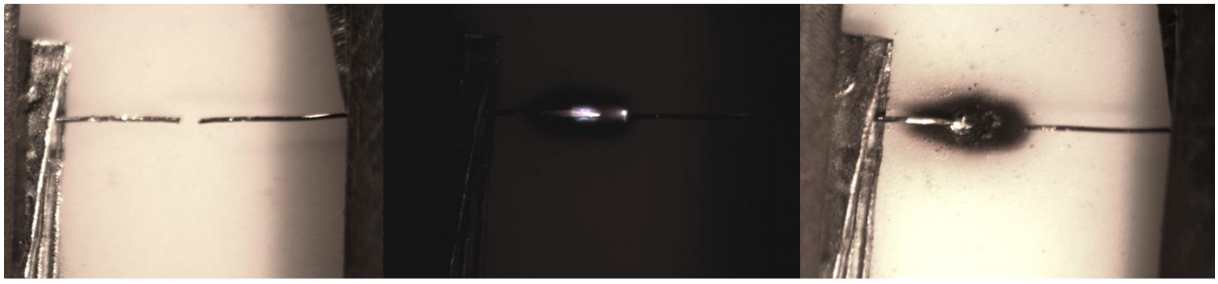

Figure 8: 50 µm diameter Pd wire testing in Air, 1.74 mA and 4 kV, Alumina substrate 200 second experiment duration initial electrode spacing 168 µm, final electrode spacing 548 µm

Similar testing was conducted with 50 µm diameter palladium in Nitrogen at atmospheric pressure at 2 mA and 4.3 kV. The starting electrode gap spacing for the setup was 65 µm and had grown to ~130 µm after 200 seconds. This experiment run in Nitrogen can be seen in figure 9 below. Electrode material sputtering that occurred during experimentation can be seen in figure 9 (c).

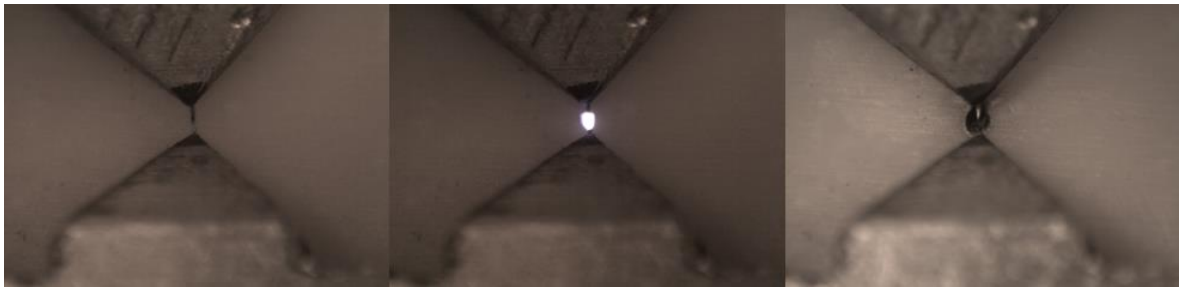

Figure 9: 50 µm diameter Pd wire testing in Nitrogen, 2 mA and 4.3 kV, Alumina substrate 200 second experiment duration initial electrode spacing 65 µm, final gap spacing 130 µm

Various wire material and ambient gas combination tests were carried out in order to gain a deeper understanding of the threshold current-voltage loads each material can handle. Once a deeper understanding was obtained through experiments run with

different wires in different gases experiments with three electrode gated configurations were carried out using a Platinum-Rhodium alloy (Pt-13%Rh). These experiments serve the purpose of having a third electrode act as a gate, thus switching the discharge on and off. The third electrode would switch between being a floating gate and having a potential roughly half that of the source electrode. In order to fit the gate electrode between the source and drain electrodes, its feature size was to be smaller thus a 25 μm diameter wire was used. This configuration can be seen in figure 10 below.

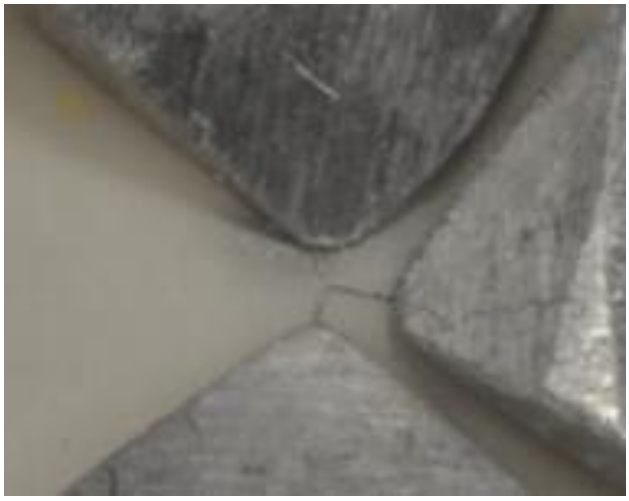

Figure 10: Three electrode setup using Platinum-Rhodium wires with a source electrode (top), gate electrode (right) and a drain electrode (bottom).

4.2.3 Thin Film Deposition Electrodes

Progressing forward with the project, electrodes were to be attached permanently on top the substrate surface thus making the device one solid piece rather than a substrate with electrode wires pressed on its surface. Thin film deposition was utilized to achieve electrodes permanently attached to the substrate surface. This was achieved by using a

vacuum metal evaporator. When depositing thin metal films using a metal evaporator patterns can be made by masking the substrate. Early patterns were achieved by simple masking techniques using high temperature shadowing materials such as high temperature tape, small diameter metal wires and glass wool fibers. These masking materials were used to the electrode shapes and more importantly the electrode gaps. Using these techniques, feature sized on the order of 10 μm were achieved, however this masking technique yielded inconsistent electrode patterns and gap spacing.

In order to consistently achieve such fine electrode patters and gap spacing photolithography was used. Two and three electrode configuration patterns with electrode gap spacing ranging from 25 μm to 200 μm were drafted in SolidWorks and printed on clear overhead projector paper. These were used as a shield from a UV lamp during photolithography resulting in the negative of the patterns on the substrate materials. The substrate with the negative pattern was inserted into the metal evaporator and a thin metal film covered the entire substrate surface. After the thing film deposition, the photoresist material was removed along with the metal deposited on it revealing the substrate with the required patterns. Varying metals such as Nickel as seen in Figure above, Copper, Aluminum and Titanium were deposited in order to test a variety of thin film electrode materials. Examples of these different deposited materials can be seen in figure 11, figure 12, figure 13 and figure 14.

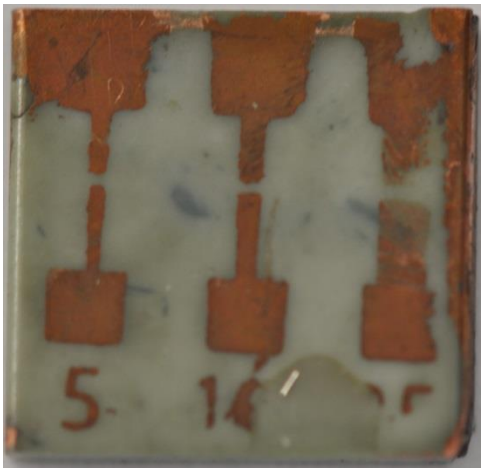

Figure 11: 2-Electrode configurations Copper electrode thin film deposition on Ceria Stabilized Zirconia

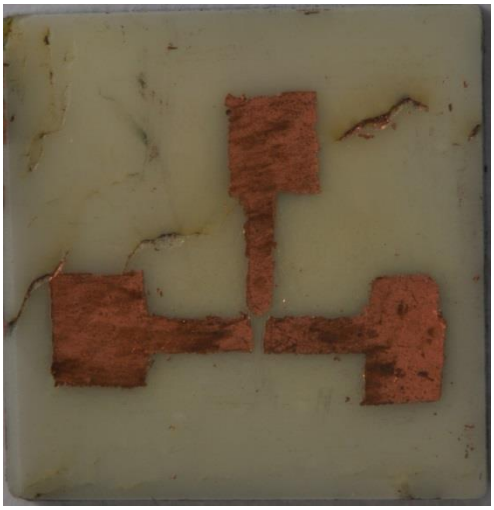

Figure 12: 3-Electrode gated configuration Copper electrode thin film deposition on Ceria Stabilized Zirconia

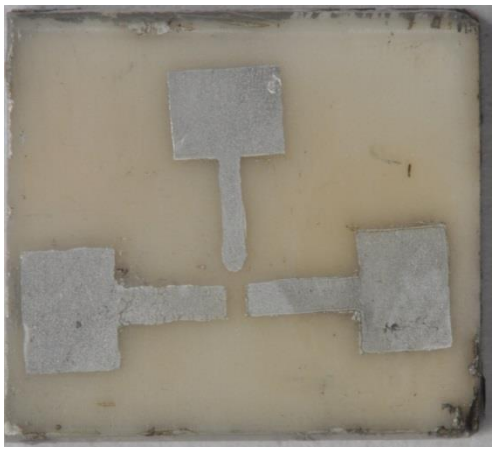

Figure 13: 3-Electrode gated configuration Aluminum electrode thin film deposition on Ceria Stabilized Zirconia

Figure 14: 2-Electrode configuration Titanium electrode thin film deposition on Ceria Stabilized Zirconia

Early metal film deposition yielded electrode thicknesses of ~50 nm. In the case of the copper electrode with thicknesses on the order of 50 nm, native oxide layers would form and have a thickness on the order of that of the film, thus oxidizing all the way

through to the substrate surface. Testing such thin films caused the electrodes to overheat and sputter away within a few seconds of being exposed to the plasma discharge. Modification to the internal geometry of the metal evaporator bringing the substrate closer to the source metal coupled with both multiple and longer runs eventually yielded thin film electrodes with thickness on the order of 0.8 µm to 1 µm. As shown in figure 15 and figure 16 below once the films reached significant thicknesses, internal stresses caused the film to peel back from the substrate surface after deposition during cooling. This was due to mismatched coefficients of thermal expansion between the deposited films and the substrate material as well as the high level of surface roughness of the Alumina substrate. This eventually prompted the moved to a more suitable substrate material.

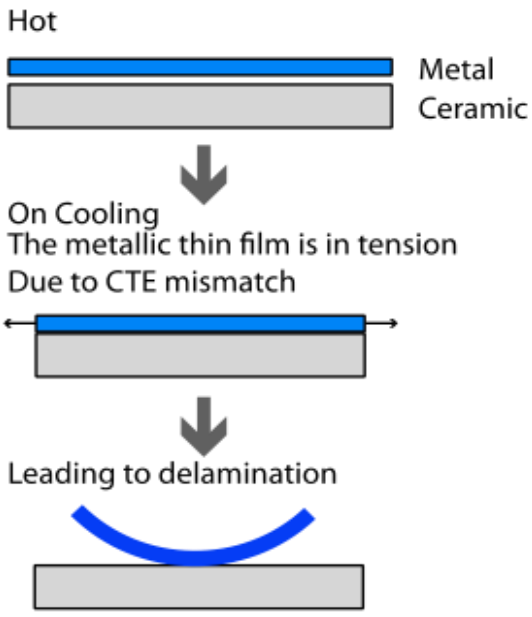

Figure 15: Illustration thin film delamination due to mismatched coefficients of thermal expansion

Figure 16: Delaminated Nickel film on Al_2O_3 substrate

With the use of more suitable substrate material, thicker films were achieving while avoiding film delamination during the cooling process. Although the thicker films were more robust and could handle higher powered plasma discharges, they were still not robust enough to cope with the high temperatures resulting in film sputtering and increasing electrode gap spacings. In order to increase electrode robustness, a superficial oxide layer was developed on the electrodes by placing the device in an oven allowing. The oxide layer provided a protective coating able to withstand the plasma temperatures without sputtering. Moreover the oxide layers provided an additional resistance of 300 MΩ per electrode in series to the external circuit connected to the device, thus yielding more stable discharges and compensating for stray capacitance from the external circuit. An example of Copper-Copper oxide electrode device is presented in figure 17 below.

Figure 17: 2-Electrode Configuration Copper-Copper Oxide Electrode ceria Stabilized Zirconia

4.3 Substrate Material Selection

Substrate materials were selected based upon high melting points in order to withstand the plasma temperatures, low electrical conductivity and high thermal conductivity. The substrate materials must be able to dissipate the temperature of the plasma to help cool the device and prolong the lifetime of the electrodes. Aluminum Oxide (Alumina, Al_2O_3) was first used as a substrate when performing the small diameter wire testing. Alumina's white color proved to be a good background when observing and photographing electrode tests in addition to spotting any electrode material that may have sputtered onto the substrate surface. As the move towards thin film deposition was made to manufacture device electrodes, silicon wafers and glass were used as substrates due to their smooth surfaces. The low surface roughness of the glass and silicon wafers allowed accurate film thickness measurements to be made with

the use of a profilometer. Once film thickness and deposition rates were known, the Alumina substrates were polished to reduce surface roughness and thin metal films were deposited onto them. As film thickness was increased to the order of 1 μm and internal stresses caused film delamination, new substrate materials had to be used. The search for a substrate material with a high melting point, high thermal conductivity and high electrical resistance with a more suitable coefficient of thermal expansion lead to the use of Ceria Stabilized Zirconia

4.4 Microfabrication Techniques

With device feature sizes and scaling being on the micrometer level, microfabrication techniques were used to consistently achieve fine detailed electrodes with electrode gap spacing down to 25 μm. SolidWorks 2D drawings of the electrode patterns and gap spacing were drafted to scale. High quality patterns were printed onto clear overhead projector paper and used as shielding patters during photolithography. Once the required electrode patterns were transferred onto the substrate surface, the substrate was placed in a metal evaporator where thin metal film deposition covered the substrate. After cleaning, the devices were ready for testing.

4.4.1 Photolithography

Photolithography was utilized as a means to achieve high quality device features that were repeatable. The consistency and repeatability of the allowed for identical devices to be manufactured using various electrode materials and then compared through similar tests. The photolithography process required several iterations before it was perfected for

the specific task at hand. Proposer storage of the photolithography materials such as the photoresist, resist thinner, resist developers and the resist remover required refrigeration however before use they were warmed up to room temperature. Appropriate lighting such as yellow incandescent, gold or white fluorescent was to be used along with a yellow or orange filter to avoid premature polymerization of the photoresist. A hood with orange acrylic sheets was used as a light filter and all photolithography took place within the hood. The substrate had to be properly prepared to insure the absence of dust and organic materials that can alter the results and insure proper adhesion of the photoresist to the surface. After cleaning with water in a sonicator and alcohol, the substrate was dried at 190 C for 22 minutes and then placed on a sterile metal plate to aid in cooling. The substrate was left to cool down for 10 minutes before being placed on a spin coating rotor plate. Two separate spin coatings were done at 600 rpm and then 1800 rpm for 15 seconds and 25 seconds respectively. This insured a uniform thickness coating over the substrate surface. Once the photoresist was applied, the substrate was prebaked for 27 minutes as 125 C. The prebake step proved to be the most problematic and required many trials at varying temperatures and times to achieve the right amount of adhesion of the photoresist to the substrate. After the photoresist was prebaked the substrate was left to cool down for 5 minutes. The printed device electrode patterns on the clear overhead projector paper were used as masking during the photoresist exposure step. An Ultra Violet (UV) lamp was used to polymerize the photoresist with an exposure of 30 seconds. The exposure time depended upon the type of light source and the light source intensity. Once polymerization of the photoresist was achieved, the

substrate was soaked in the developer for 1 minute and then in IPA to remove the developer and stop the development of the photoresist. Once the developer was removed, the substrate was postbaked in order to remove residual photoresist that had not been exposed to the UV lamp. The substrate with the photoresist was postbaked for 15 minutes at 130 C. The postbaking process left the substrate exposed in the pattern of the required electrodes. A three electrode configuration example of a substrate prepared using photolithography can be seen in figure 18 below, where the dark yellow region indicate the remaining photoresist.

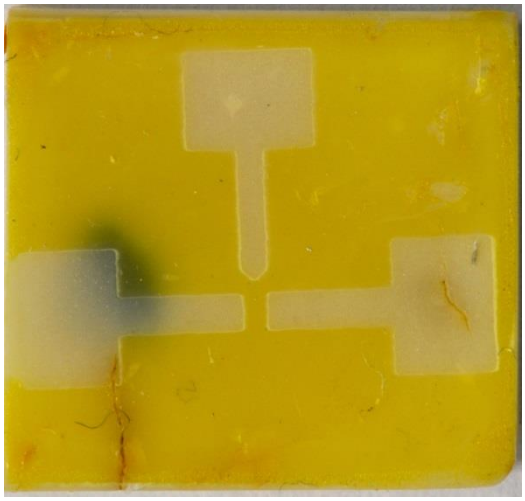

Figure 18: 3-Electrode configuration on CSZ ceramic substrate achieved using photolithography, 150 µm electrode gap spacing

4.4.2 Metal Evaporation

A Vacuum Metal Evaporator was used to achieve thin metal film deposition onto the substrate and photoresist surface. After postbaking in the photolithography process, the

remaining photoresist shielded the substrate surface from metal atoms being deposited in unwanted regions. Various metals such as Aluminum, Copper, Titanium and Nickel were used in the metal evaporator to make up the device's thin metal film electrodes.

During the thin film deposition process using the metal evaporator, the source metal to be used as the electrode material was placed in a tungsten boat. The metal evaporator vacuum chamber was prepped with vacuum grease in order to hold a vacuum down to 7E-6 Torr. Liquid nitrogen was used for cryogenic pumping to insure a high vacuum was achieved. A high vacuum is necessary to insure the evaporated metal particles do not collide with preexisting particles in the chamber. This allows the evaporated metal particles to travel almost directly to the substrate where they condense and build up. A good vacuum along with a smooth substrate surface free of dust and organic materials insures better control over metal film thickness and deposition rates. During the evaporation process, the evaporated metal particles leave the tungsten boat in a wide view angle, thus not all the evaporated particles will coat the substrate and most will end coat the inside of the evaporator chamber. For maintenance reasons, aluminum foil was used to shield the inside of the vacuum chamber during runs intended for thick film deposition. Early film deposition thickness was on the order of 50 nm and would oxidize all the way to the substrate surface. In order to stop complete film oxidation, Nickel and Aluminum were used. Looking at Aluminum, as an example, a layer of Aluminum Oxide would form at a thickness of 3 nm to 5 nm and shield the underlying layer of Aluminum from oxidizing. Once tested, such thin metal films sputtered under the intense heat of the plasma discharges. Evaporation due to the high plasma discharge

temperatures occurred with deposited electrodes of all materials listed, thus it was evident thicker metal films had to be achieved to obtain more robust electrodes. In order to achieve thicker metal films, more source material was placed in the tungsten boats allowing for longer deposition runs. Once the source material was completely evaporated, the chamber was pumped up to atmospheric pressure with the aid of a nitrogen tank and source material was added into the boats and the chamber was prepped and evacuated again to a vacuum. This allowed for multiple runs that would build up layers of the deposited metals. Silicon substrates were partially masked and placed in the evaporator along with the substrates. The low surface roughness of the silicon substrates allowed for accurate film thickness measurements to be made using a profilometer. Film thickness on the order 200 nm to 300 nm was achieved. Discharge testing however indicated film thicknesses were still not too low to yield robust electrodes capable of coping with discharge temperatures. To achieve required film thickness nearing the micron level, the internal geometry of the metal evaporator vacuum chamber was changed using a steel stand that was placed inside the vacuum chamber. These internal geometry changes allowed the substrate to be placed much closer to the tungsten boat with the evaporating source material. By doing so, a higher percentage of the evaporated particles will condense on the substrate surface. The steel stand used to hold the substrate close to the source material can be seen in figure 19 below along with a coated Alumina substrate sample in figure 20.

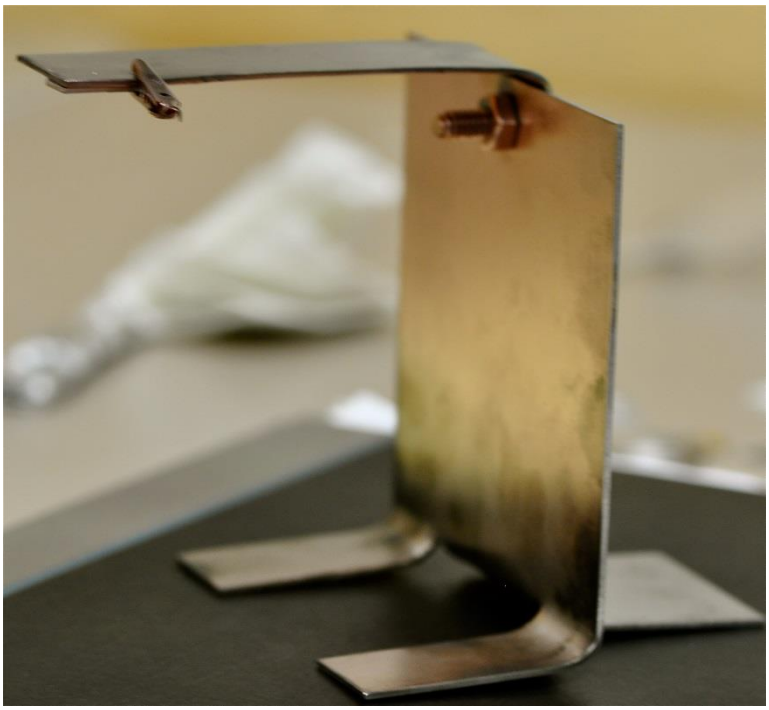

Figure 19: Steel stand to optimize evaporation chamber internal geometry

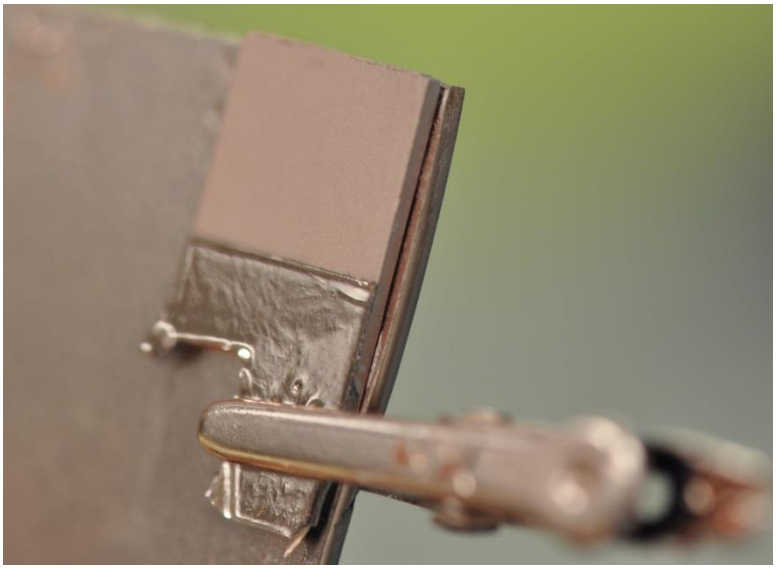

Figure 20: Zoomed in view of Al_2O_3 substrate post Copper deposition mounted on steel stand for closer geometry

Post deposition at the new internal geometry of the vacuum chamber, the substrates were taken out so the photoresist material can be removed. An Aluminum three electrode configuration substrate can be seen in figure 21 below as an example before removal of photoresist material. Once photoresist material, along with the deposited metal film on its surface was removed, the substrate will have the required electrode pattern remaining. In order to remove the photoresist material, the substrate was placed in an oven at 400 C in order to remove all organic material. An example of the substrate post photoresist removal is presented in figure 22.

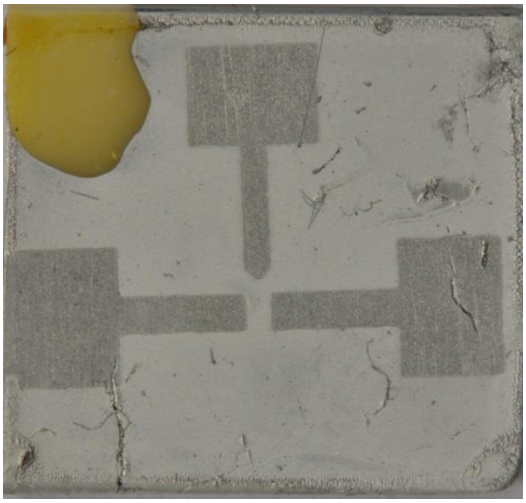

Figure 21: Aluminum deposition on CSZ substrate 3-electrode configuration post, thick film deposition

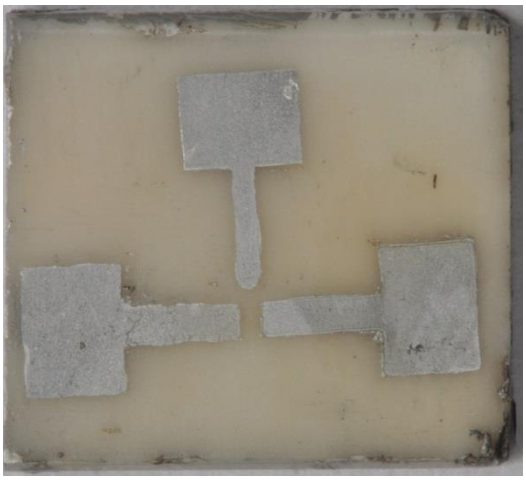

Figure 22: Aluminum 3-Electrode configuration on CSZ substrate post photoresist material removal

The internal geometry changes along with multiple runs achieved film thickness on the order of 0.8 μm to 1 μm, in the case of Aluminum deposition, verified with the use of a profilometer. Scanning Electron Microscope (SEM) cross sectional inspection of a Copper electrode deposited on a Ceria Stabilized Zirconia substrate using the new internal geometry of the vacuum chamber along with multiple runs can be seen in figure 23 and shows a film thickness of ~2 μm.

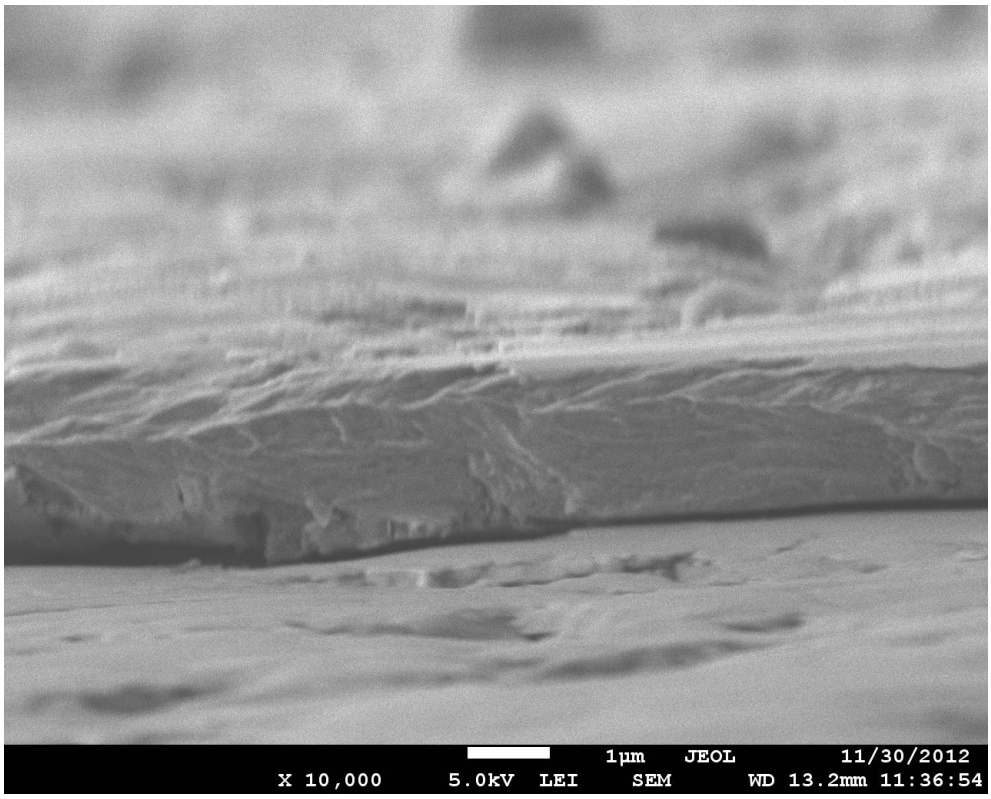

Figure 23: SEM image of Copper thick film deposition on CSZ substrate, 2 µm film thickness

Such thick films proved to be more robust and were able to withstand higher power discharges, up to 2.1 kV and 0.65 mA for longer periods of time up to 6 minutes. Two different processes of photoresist removal were executed yielding different results for testing. Photoresist was removed by burning off the organic material and leaving behind the metal electrode patterns. This removal process was done through manual scraping or with a hotplate in a vacuum chamber. The vacuum chamber heating insured that the electrodes would not oxidize due to the absence of oxygen while the manual scraping process avoiding heating up the electrodes all together. Substrates with identical film thicknesses and electrode material, Copper, were placed in a non-vacuumed over to

remove the organic photoresist. In this photoresist removal process, the electrodes were exposed to air when heated thus causing a superficial oxide layer to form on the electrode surface. A result comparison of the two processes can be seen in figure 24 below.

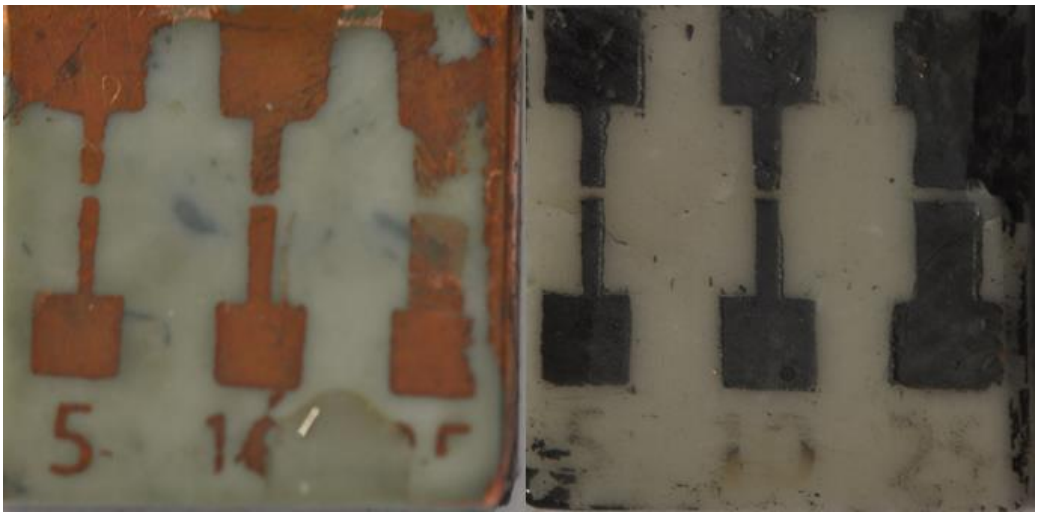

Figure 24: Copper (left) and Copper-Copper Oxide (right) electrodes deposited on CSZ substrates, 2µm thick films on both substrates photoresist removal: in absence of oxygen (left) and in presence of oxygen (right)

4.4.3 Electroplating

Electroplating was utilized to achieve thicker electrodes after using the thing film deposition. Thin film deposition achieved with the metal evaporator was used as an initial layer in order to have a conductive receiving surface on the ceramic substrate surface. Once the conductive film was deposited onto the substrate surface it was polished with soap water and then in ethanol to remove dust and organic material such as

finger oils to insure a clean surface ready for electroplating. The clean substrate with the thin deposited film was attached with an alligator clips to the negative terminal of a power supply making it the cathode in the system. A cleaned and polished Copper tube was used as the anode terminal to be used as the source material for platting. Initially vinegar was used as the electroplating solution yielding electroplated film thickness on the order of a few microns. Early testing of the electroplating system was done on brass substrates with polished surfaces. This was done as a test run in order to gather data on different electroplating solutions as well as the film thickness and deposition rates achieved while using them without sacrificing any microscale devices. After several test runs enough data and trends were gathered to make final decisions on the electroplating solution and how much power would be required according to substrate surface area.

The final electroplating solution consisted of 10 g Copper-Sulfate in 150 ml distilled white vinegar, 100 ml water, and 4 drops of dish soap to act as a brightener. In order to achieve lower surface roughness during electroplating low power was used with a current of 0.1 A and voltage of 2 V. After 2 hours of electroplating in the electroplating solution at the specified voltage and current, electrode film thicknesses were increased from 2 μm to 35 μm. An image of the a Copper film peeled off a substrate surface after electroplating can be seen in figure 25 along with a 50 μm diameter wire for size comparison.

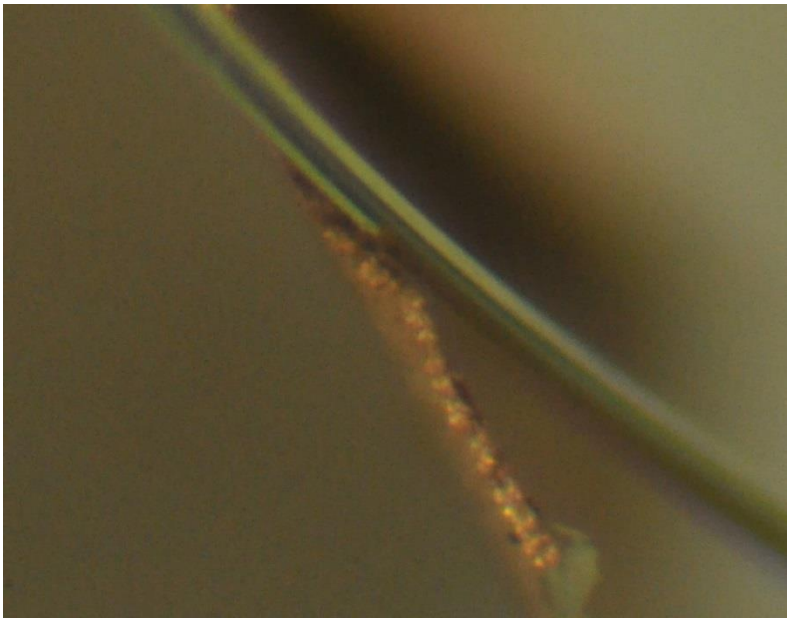

Figure 25: Electroplated Copper film peeled off CSZ substrate ~35 µm thickness, in comparison with 50 µm diameter wire

5. DEVICE TESTING

5.1 Chapter Summary

Two wire configurations were set up on Alumina substrates in order test the electrode materials. Wires were initially Ag, Au, Pd and W and were selected as such due to their high electrical and thermal conductivity as well as high melting points, in the case of tungsten. Early testing revealed that wires would overheat and start to melt and sputter onto the Alumina substrate surface after extended periods of testing durations around 5 to 20 minutes with currents around 1 mA and 2 kV voltages. Wire material selection while still using Alumina substrates, moved towards Pd-13%Rh at diameter of 50 μm. These new wire alloys proved to be robust and could handle the temperatures presented by the discharge. Three electrode configurations were then tested with a 25 μm diameter Pt-13%Rh wire used as a gate electrode. In order to achieve consistent electrode spacing and move towards producing larger quantities of test cells, two electrode configurations were manufactured with the use of photolithography techniques and thin metal film deposition on the Alumina using a metal evaporator. The thin metal film would deteriorate and oxidize virtually overnight. Due to insufficient film thickness, the oxide layer that would form would end up being proportional in thickness to that of the metal film itself. Initial metal film consisted of Nickel, Copper, Aluminum and Titanium with thickness ranging from 50 nm to 150 nm depending on evaporator currents selected and deposition time. Limitations with the metal evaporator were the amount of the film material the tungsten boats could contain and the spread of

evaporated metals. Slightly thicker film deposition on Alumina substrates was achieved through increasing metal evaporation timing and runs. Once thicker films were achieved, an oxide layer would form and only be a fraction of the overall film thickness, thus acting as a protective coat for the rest of the deposited material. Once tested, plasma discharges would disintegrate the electrodes and sputter them away due to still relatively low film thickness and insufficient het shedding. Thicker film deposition on Alumina was attempted in order to have thicker and thus more robust electrodes, yet once film thickness became thick enough to increase robustness, the thickness started to have enough internal stresses in the film to cause it to peel back and away from the substrate due to large differences in coefficient of thermal expansion. Selection of substrate moved from Alumina towards Ceria Stabilized Zirconia ceramics due to their better matched coefficients of thermal expansion, while still having favorable thermal and electrical conductivities. Modifications during evaporation process such as evaporation rate, controlled by temperatures due to the selected current, and increased deposition time yielded thicker films on the order of 0.8 μm up to 2 μm. Results of these modified evaporation techniques resulted in deposited metal films with increased robustness, but still unable to withstand extended periods of discharges. Aluminum and copper metal films were oxidized in an oven in order to promote the development of a protective oxide layer and speed up a natural occurring process. Titanium-Titanium Oxide and Copper-Copper Oxide electrodes proved to be best thin film deposition results yet, withstanding 1 mA and 3 kV in the case of Titanium-Titanium Oxide and 1 mA and 3.3 kV for Copper-Copper Oxide for relatively long periods of time and showing no signs of

deterioration or degradation. Discharges using Copper-Copper Oxide electrodes seem to be more stable, possibly being attributed to the ~250-360 M-Ohm resistance of the superficial oxide layer [42,47]. This oxide layer also served the purpose of compensating for stray capacitance and acted as a larger ballast resistor. Electroplating was used on the thin film deposition starting with a thickness of ~2 μm as an initial conductive surface and increasing its thickness, thus achieving film thicknesses 35 μm. Controlled surface oxidation of these copper electrodes added a protective layer with a high electrical resistance. Future work along these lines is to replicate these experiments and achieve similar results with Pt-13%Rh alloys in place of the copper electrodes.

5.2 Unit Cell

The unit cell to serve as a microscale plasma transistor must be able to fulfill the following criteria:

a. High robustness to operating environments. Able to withstand 3000 K discharge temperatures, Electrical / Electro-Magnetic interference and spikes in voltage and current.
b. Small device features on the order of 1-20 μm.
c. Low cost - high rate manufacturability.
d. High level of device uniformity.
e. Sustain high electron and energy density microplasma discharges
f. Fast switching on the order of 100 ps (current rise time)

5.3 Fabrication

Several stages of device fabrication took place depending on what aspect of the device was being tested. When testing the discharge characteristics high pressure stainless steel test chambers were assembled for testing both steady and transient discharges. The nature of the discharge, whether steady or transient, depended on the nature of the external circuit. The high pressure test chambers were also used to test the effects different gases and varying ambient pressures have on the discharge size, temperatures and electrical characteristics. In addition, the high pressure test chambers were used to test what degradation effects the plasma discharge would have on the electrodes.

Once the discharges were better understood, small diameter wires were manually placed onto Alumina substrates with electrode gap spacing on the order of 50 μm. These wires were later replaced with thin metal film electrodes. These metal film electrodes were achieved through the use of photolithography and vacuum metal evaporation.

5.3.1 Robust Materials

To insure long operating lifetime, the microscale plasma device was to be manufactured out of robust material able to withstand the plasma discharge. Plasma temperatures were on the order of 3000 K, thus robust materials were to be selected for both the substrate and the electrodes. High melting points along with high thermal conductivities were decision making factors when choosing appropriate substrate and

electrode materials. A high electrical conductivity was desired in the electrode materials while a high electrical resistance was required for the substrate material.

5.3.1.1 Substrates

An Aluminum Oxide, Alumina, substrate was originally selected for use as substrate due to its high thermal conductivity, high electrical resistance and high melting point. The Alumina substrate was used for initial device testing coupled with small diameter wire testing and early thin film deposition. During thin film deposition, films with greater than 300 nm thickness would begin to delaminate. High surface roughness in combination with miss matched coefficients of thermal expansion was believed to have caused delamination of deposited metal films during post deposition cooling process. To continue project progress, a more suitable substrate material with lower surface roughness and a better matched coefficient of thermal expansion was selected. The new ceramic, Ceria Stabilized Zirconia (CSZ) proved to be a more suitable substrate material with the required high melting point, thermal conductivity and electrical resistance. Small diameter wire testing along with thicker metal film deposition experiments continued with the use of CSZ as the substrate material.

5.3.1.2 Electrodes

Electrode testing was carried out in order to obtain an understanding of what materials would be suitable for electrodes to be used in the microscale plasma transistor. Electrode material selection experiments were conducted with the use of small diameter wires. 50 μm diameter wires of differing materials Silver, Gold, Palladium, Tungsten

and a Platinum-Rhodium alloy (Ag, Au, Pd, W and a Pt-13%Rh Alloy respectively) were individually used as electrodes to test their durability. Melting point, electrical, and thermal conductivities were all determining factors to choose an appropriate material. To enhance thermal conductivity and the ability for the electrodes to shed heat generated by the discharge, Aluminum brackets were used to hold down the electrode wires while acting as a heat sink. The 2-electrode configurations were tested at varying gap lengths in atmospheric pressure air and inert Nitrogen gas, all with similar power loading. These tests were recorded and compared to one another to determine which materials would be more favorable for the task at hand. Silver and Gold were initially selected, despite relatively lower melting points, due to their superior electrical and thermal conductivity. It was believed high thermal conductivity coupled with a heat sink could be sufficient in shedding the temperatures generated by the plasma discharge. Early testing with silver indicated a high melting point coupled with the high electrical and thermal conductivity was important to avoid sputtering of the electrode tips.

Other materials such as Tungsten (W) were superior in withstanding high temperatures but were hard and brittle to work with in addition to oxidizing rather quickly. Palladium, Pd, electrode testing yielded better results than the Silver testing, however eventual evaporation under increased discharge power occurred. The material chosen to carry on testing with was the Pt-13%Rh alloy due to its high thermal conductivity and high melting point. 3-electrode gated configurations were eventually assembled with the use of 50 μm Pt-13%Rh electrodes for a source and drain and a 25

μm Pt-13%Rh electrode serving as the switching gate, this can be seen in figure 26 below.

Figure 26: 3-Electrode gated configuration using 50 μm Pt-13%Rh alloy wire before (left), during (middle) and post switching (right)

5.4 Film testing

Glow Discharge, although regarded as non-thermal plasmas, can achieve relatively high temperatures depending on discharge power and the ambient gas the discharge occurs in. These high temperatures along with electron emission mechanisms of the discharge cause electrode degradation, primarily to the cathode. Under the right conditions, power and ambient gas, Glow Discharge temperatures can surpass the melting point of the electrode. Once the discharge reached that temperature the electrode will melt and deform due to being sufficiently heated. Electrode melting results in the deformation of the electrode shape as it melts and resolidifies in addition to a change in the electrode gap spacing. Electrode melting can be avoided by running the discharge at a lower power, by pulsing the discharge or by varying the ambient gas. As temperature is

further increased beyond the electrode material's melting point, electrode vaporization occurs. At sufficiently high temperatures the discharge causes the electrode to evaporate and condense onto the substrate surface. Evaporation results in deformation of the electrode geometry, changes to the electrode gap spacing and may cause condensed electrode material on the substrate to connect the cathode and anode, effectively shorting the gap and eliminating the discharge. Sputtering is another form of electrode degradation which occurs when the cathode surface is bombarded by neutrals and positively charged ions. As an electric potential is applied across the spark gap, positively charged ions will migrate towards the negatively charged cathode. Due to the large number of neutral atoms, as the ions travel towards the cathode they may strike neutral atoms and transfer some of their energy to the neutrals. A combination of ions and neutral atoms will strike the cathode redistributing their energy to it causing free atoms to be ejected from the cathode surface. Sputtering causes pitting to occur on the cathode surface which leads to changes in the cathode geometry and discharge location.

Gas selection is an important parameter for controlling discharge temperatures since different gases have different heat transfer coefficients which affect the gas temperature, vibrational temperature and electronic excitation temperature. Changes in pressure also have an effect on discharge temperatures, as pressure increases so do the particle density and collision frequency. At higher collision frequencies, the discharge will reach a thermal equilibrium between the electron temperature and the gas temperature effectively increasing the plasma temperature.

During testing of the Aluminum electrodes, the increased film thickness was still not sufficient enough to cope with and dissipate the heat generated by the plasma discharge. The 1 μm thick Aluminum electrodes evaporated ~ 11 seconds after the discharge was turned and electrode gap spacing rapidly increased by ~ 1mm. When testing both Copper and Copper-Copper (II) Oxide electrodes, both performed better than lower film thickness electrodes, however after about 6 minutes of testing, electrode gap spacing of the non-oxidized Copper would increase due to electrode sputtering while the Copper-Copper (II) Oxide electrodes did not sputter, thus maintaining constant electrode gap spacing. Testing of Titanium electrodes gave similar results as the Copper-Copper (II) Oxide testing, most likely due to the much higher melting point of the Titanium electrodes. However discharge stability seemed to be the greatest in the Copper-Copper (II) Oxide electrodes. This is believed to be due to the increased electrical resistance of the electrodes due to the superficial oxide layer, adding ~250 MΩ to 350 MΩ per electrode. Comparative testing of the thick film Aluminum, non-oxidized Copper electrodes, Copper-Copper Oxide electrodes, and Titanium electrodes with similar electrode gap spacings are summed up in table 2.

Table 2: Comparison of thick film deposited electrodes of varying materials: Aluminum, Copper, Copper (II) Oxide and Titanium

	I (mA)	V (kV)	Time (s)	Electrode Evaporation	Increase in Electrode Gap Spacing (μm)
Al	0.01	1.3	11	Y	1000+
Cu	1.12	2.1	363	Y	150
	0.99	2.8	-	Y	150
	0.82	2.2	370	Y	150
	0.65	2.6	365	Y	100
	0.57	1.8	377	Y	150
	0.43	3.4	358	Y	100
Cu-CuO	1.0	3.3	t > 400	N	N/A
	1.0	2.6	t > 400	N	N/A
	0.92	2.5	t > 400	N	N/A
	0.75	2.8	t > 400	N	N/A
	0.7	2.1	t > 400	N	N/A
	0.6	1.9	t > 400	N	N/A
	0.5	1.7	t > 400	N	N/A
	0.4	1.7	t > 400	N	N/A
TiO	1.0	3.0	t > 400	N	N/A
	0.85	2.8	t > 400	N	N/A
	0.75	2.6	t > 400	N	N/A
	0.65	2.4	t > 400	N	N/A
	0.55	2.2	t > 400	N	N/A
	0.45	2.1	t > 400	N	N/A
	0.35	1.8	t > 400	N	N/A

Control and consistency over the metal evaporation process was incredibly important to insure proper film deposition with required thicknesses. After evaporated metal deposition took place, film thickness measurements were made with the use of a profilometer. Data associated with the metal evaporation process such as the weight of

the source metal placed in the boat, current passing through the tungsten boat, vacuum chamber pressure, evaporation run time and the number of runs performed was collected. The collected data in addition to preexisting data was used to acquire film deposition rate and build trends for the metal evaporator to accurately depict the film thickness. The note taking was specific per metal being evaporated to insure accuracy. Once the deposition rates were used to obtain film thickness, the profilometer was used to verify film thickness estimates.

In table 2 above, the tested Aluminum films had a thickness of ~3 μm, according to Aluminum deposition rate data. The initial electrode gap spacing was 100 μm and ~ 1mm post testing due to electrode overheating and sputtering. Copper and Copper-Copper Oxide film thicknesses, as depicted by acquired deposition rates and verified by with a profilometer and Scanning Electron Microscope (SEM), were on the order of 2 μm. The presented experimental result for the non-oxidized copper electrodes at 0.43 mA and 3.4 kV was at a gap spacing of 200 μm, while the 0.57 mA and 1.8 kV experiment was carried out at an electrode gap spacing of 100 μm. The rest of the experiments presented in table 2 above were conducted at an electrode gap spacing of 150 μm.

For Copper-Copper Oxide film testing resulting with 0.75 mA - 2.8 kV and 1.01 mA - 3.3 kV was carried out at an electrode gap spacing of 150 μm. The rest of the Copper-Copper oxide testing presented in table 2 was carried out at an electrode gap spacing of 100 μm. Titanium -Titanium Oxide electrode film thickness of approximately 800 nm

testing resulted in 0.35 mA- 1.8 kV, 0.45 mA - 2.1 kV and 0.55 mA - 2.2 kV at an electrode gap spacing of 100 μm. Testing at 150 μm electrode gap spacing yielded 0.65 mA - 2.4 kV, 0.75 mA - 2.6 kV, 0.85 mA - 2.8 kV and 1 mA - 3 kV. Evaporation was determined by viewing the discharge and electrodes under a microscope mounted camera. The estimated accuracy of using the acquired micrographs was about 10 μm.

5.4.1 Thin Film Testing

Once film thickness was sufficient enough to not oxidize down to the substrate surface, the thin film electrodes resulting from the early stages of metal film deposition using the vacuum metal evaporator were tested with plasma discharges. An alligator clip was clamped onto the output of the ballast resistor and simply clamped onto the surface of the electrode, giving a mechanical contact with the electrode. Another alligator clip was then clamped onto the adjacent electrode and connected to the stainless steel surface of optical table for grounding. Current and Voltage were slowly increased until breakdown occurred and the adjusted in order to maintain a minimal powered discharge. As the discharge between the two deposited electrodes took place, the electrodes overheated and sputtered away thus increasing the electrode gap spacing. In addition, the discharge was not steady and resembled a spark. Examples of Nickel thin film electrode testing can be seen in figure 27 and figure 28. In figure 27, the substrate material is the Ceria Stabilized Zirconia ceramic with an electrode film thickness of ~120 nm. In comparison with similar film thickness of Nickel electrodes deposited on an Alumina substrate in figure 28, it can be seen that a greater degree of delamination of the electrodes occurred with the Alumina substrate. This can be attributed to the greater

surface roughness on the Alumina substrate and lower adhesion of the electrode film due to the mismatched coefficients of thermal expansion as discussed in the substrate material selection section above.

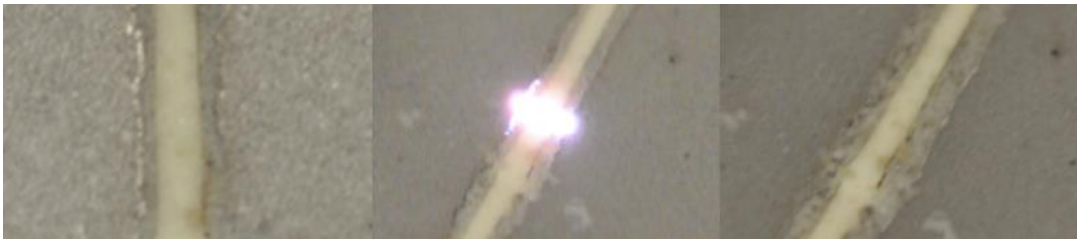

Figure 27: Nickel on CSZ substrate before, during and after 120 nm thick layer 250 µm gap pre-test and ~500 µm gap post-test

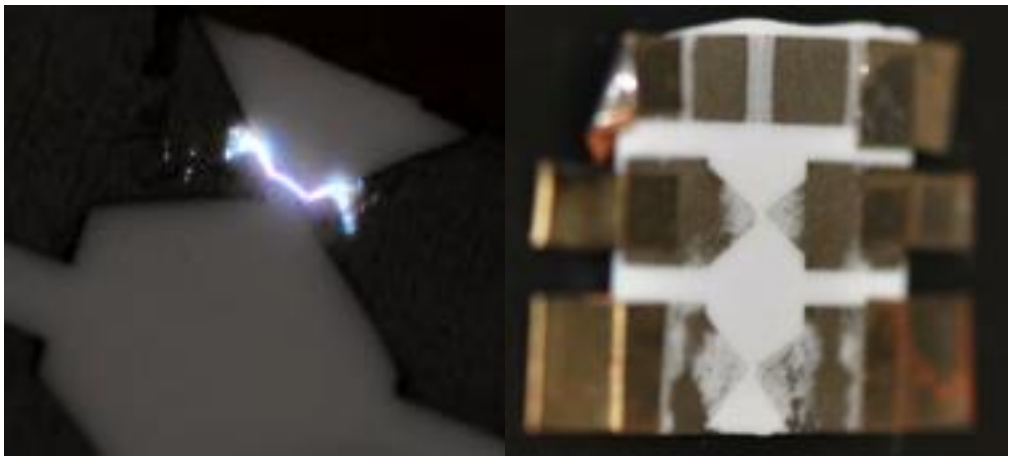

Figure 28: Thin deposited Nickel film on Alumina substrate during and post experimental testing, ~150 nm film thickness

5.4.2 Thick Film Testing

After increased deposition times, multiple runs and modifications to the internal geometry of the metal evaporator's vacuum chamber, thicker electrode films were achieved on the order of 0.8 μm to 2 μm. These thicker films were tested under similar conditions to initial deposited film testing. Thick Aluminum deposited films, despite having high thermal conductivity, were unable to shed the heat generated by the discharge and the electrode sputtered thus increasing the electrode gap spacing. Thicker Copper film deposition proved to be more robust than the thinner Copper film electrode, however as was highlighted in table 2 above, lasted approximately 6 minutes before apparent film sputtering was occurring. An example of thick Copper film deposition is presented in figure 29 below, where sputtering and electrode gap spacing changes are apparent. A more comprehensive and detailed summation of thick metal film testing has been covered in table 2 above.

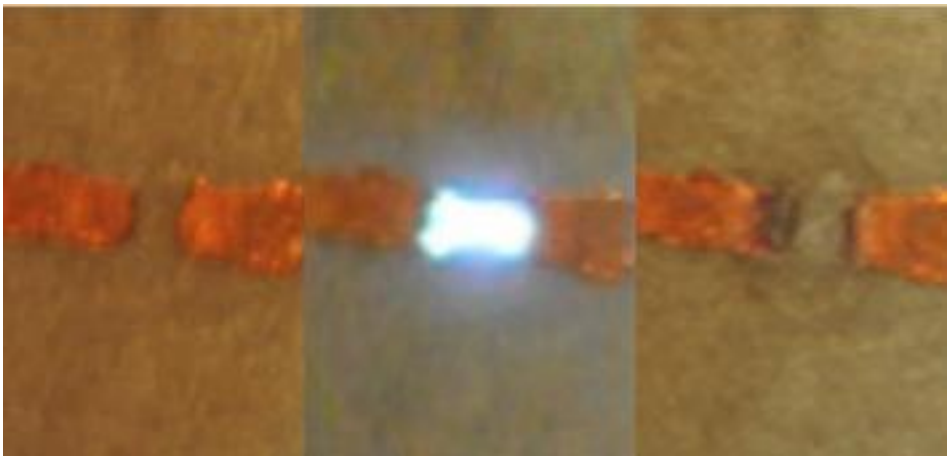

Figure 29: Sputtering of deposited copper electrode causing increase in electrode gap spacing

Increasing the deposited electrode film thickness yielded more robust and longer lasting electrodes capable of withstanding discharges at 1.2 mA and 3.1 kV for longer periods of time before noticeable electrode degradation took place. As electrode film thickness increases the overall cross sectional area of the electrode film increases at an identical rate. In order for energy to be maintained, the energy gained by the electrode from the plasma discharge in the form of heat must be dissipated. This dissipation of energy takes place in the form of thermal conduction within the electrode, thermal conduction between the electrode and the substrate, thermal convection with the surrounding gas, thermal radiation with the surrounding surfaces and through mass transfer for the case of evaporation. As the cross sectional area of the electrode increases, conduction within the electrode is increased, thus energy is dissipated from the electrode tip to the rest of the electrode. This causes the electrode to have a more uniform temperature while the temperature at the electrode tip, where melting and evaporation occur, will decrease. With a more uniform temperature the electrode can dissipate the energy more effectively via conduction to the substrate surface, convection with the surrounding gas and via radiation all through a larger surface area. Conduction within the electrode itself is governed by Fourier's law of heat transfer shown below in equation 7.

$$Q^{"} = K\ A\ \frac{dT}{dX}\ \ (Eq\ 7)$$

where:

$Q^{"}$ = Heat Flux

K = Thermal Conductivity (Material Dependent Constant)

A = Unit Area (Cross sectional Area of Electrode)

T = Temperature

X = Distance

A larger cross sectional area caused a higher heat flux throughout the electrode yielding the uniform electrode temperature and increases localized energy dissipation from the electrode tip to the rest of the electrode. Energy dissipation to the surrounding gas occurs via convection. Equation 8 below illustrates the heat flux from the electrode surface to the surrounding gas due to convection.

$$Q^{"} = h\, A_s \left(T_s - T_g\right) \ (Eq\ 8)$$

where:

$Q^{"}$= Heat Flux

h = Heat Transfer Coefficient (Fluid Dependent Constant)

A_s= Electrode Surface Area (Exposed to Surrounding Gas)

T_s= Electrode Surface Temperature

T_g= Surrounding Gas Temperature

When testing thin film electrodes the electrode tip temperature is high and the difference in temperature between the electrode tip and the surrounding gas is large, yet the rest of the electrode material is relatively cool and the surface area for convection is very small. As thicker electrode films were achieved and larger electrode cross sectional areas lead to higher convection and more uniform electrode temperatures, the temperature difference between the electrode and the surrounding gas is not as great as it was with the hot electrode tip. However the overall product of *As (Ts - Tg)* is greater, thus when multiplied with the gas constant h yields a larger amount of convection. The same concept holds true for radiation from the electrode surface to surrounding bodies. The radiation heat transfer equation is presented in equation 9 below.

$$Q^{"} = A_s \sigma E (T_s^4 - T^4) \quad (Eq\ 9)$$

where:

$Q^{"}$ = Heat Flux

A_s= Electrode Surface Area (Exposed to Surrounding Surfaces)

σ = Radiation Coefficient (Material Dependent $0 \leq \sigma \leq 1$)

E = View Factor ($0 \leq E \leq 1$)

A_s= Electrode Surface Temperature

T = Temperature of Surrounding Surfaces

5.4.3 Thick Film with Superficial Oxide Layer Testing

A metal oxide coated electrode was integrated into the microscale plasma transistor. A metal oxide coated electrode would, in addition to the use of already high temperature robust materials, further ensure the thermal integrity and of the device. The dielectric nature of the oxide coating would also add resistance to the circuit of the device, yielding discharge stability and compensating for stray capacitance. During the post metal deposition photoresist removal stage, the substrate was inserted into a convection oven at 400 C to burn off the organic materials (the photoresist). During the photoresist removal, the electrodes were exposed to oxygen in the air while at 400 C, this caused a

superficial oxide layer to occur that was thicker than a naturally occurring oxide layer. In order to stop oxidation on selected substrates with deposited electrodes to be used as control experiments, the photoresist was removed in a vacuum oven or manually. It was noticed that Titanium-Titanium Oxide, seen below in figure 30, and Copper-Copper Oxide electrodes withstood discharges of similar power to the non-oxide coated electrodes for longer periods of time. In the testing time, no electrode sputtering was notice and no electrode gap spacing changes were observed. Moreover, discharges occurring between the oxidized electrodes seemed to be more stable than those occurring between the non-oxidized electrodes. A more comprehensive and detailed summation of thick metal film testing including test duration and discharge power has been covered in table 2.

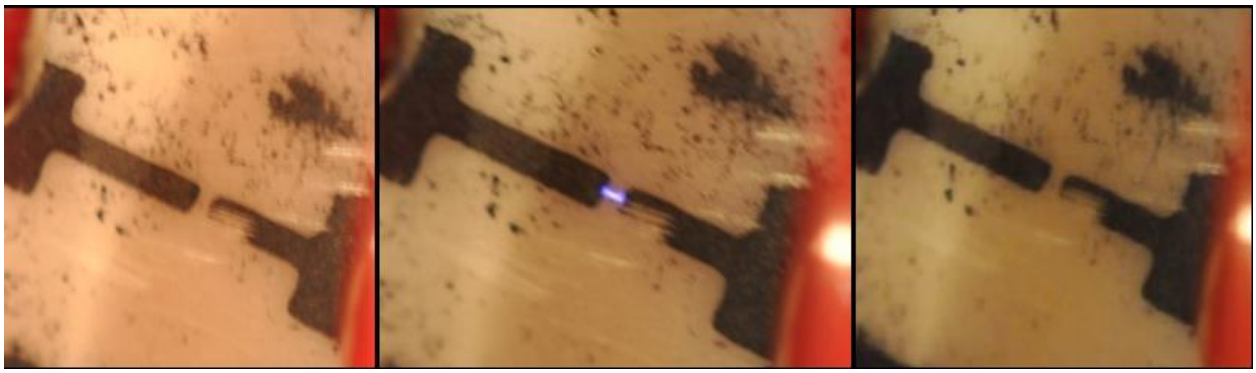

Figure 30: Titanium Titanium-Oxide on CSZ before, during and after discharge 800 nm thick layer with 150um gap, 0.75 mA and 2.6 kV coating oxidized during photoresist removal

6. EFFECTS OF PRESSURE ON MICROPLASMA DISCHARGES

6.1 Chapter Summary

There are many different parameters and characteristics of a plasma discharge affected by pressure [30-26]. Experiments where pressure was a variable parameter were carried out to study microplasmas in varying atomic and molecular gases. Studies of direct current normal glow discharges have shown the main change in the discharges while extending its length by changing the electrode spacing is an increase in the length of the positive column while other features (faraday dark spot and negative glow) remain unchanged. Pressure variation testing in these studies has shown that the gas temperature increases from ~650 K to 1300 K as pressure was increased while vibrational temperature slightly increases with pressure 3300 K to 3900 K. Further studies have highlighted the effects that pressure change has on direct current normal glow discharges showing that as pressure is increased the current density increases [16,17,46,48,36] until it reaches the threshold for the development of instabilities, leading to a transition to the arc phase. Additional observations have shown that high pressure discharges in atomic and lighter element gases are typically more stable [16,17]. This is believed to be due to faster diffusion times and slower energy transfer from electronic to translational energy modes. Stabilities of the plasma discharges with increasing pressure is a topic to be further studied in the future. Table 3 below highlights microplasma discharge diameters that have been achieved in addition to electrode spacing that have been utilized.

Operating pressures for plasma discharges that have been achieved in previous studies are additionally highlighted in table 3.

Table 3: Previously achieved discharge diameter, electrode spacing and operating pressures

Author	Discharge Diameter (um)	Electrode Spacing [discharge length] (μm)	Pressure (MPa)	Gas
[17]	100	400	0.101	H2
[43]	-	100	0.101	N2
[41]	-		1.317	H2
[33]	175	200	0.101	He
[49]	-	-	0.203	H2
[26]	250 (constrained)	10 to 100	0.101	He/Ar
[18]	100	20	0.101	Air
[50]	100 (constrained)	500	0.101	Ar
[10]	13 (constrained)	-	0.16	Ne

The change in required voltages for breakdown was investigated in pressures greater than atmospheric at varying gap lengths. As pressure is increased, while maintaining a constant electrode gap spacing, the voltage required for breakdown also increases. Increased pressure leads to an increase in the gas density since more molecules and atoms exist within a certain volume. As particle density increased the mean free path of the particles, the averaged distance a particle travels without colliding with another particle, decreases. With increased collisions electrons will collide with many more particles reducing the electrons energy as it travels along the electric field from the cathode to the anode. This requires higher voltages to sufficiently energize the electron for it to be capable of ionizing particles it collides with [30,32,36]. The breakdown

voltages were recorded and plotted verses constant values of Pd in order to construct Paschen curves, yielding further insight into the effects pressure have on microplasma glow discharges. As highlighted by already established Paschen curves breakdown voltages increase with increasing pressure in additional to increasing sustainability voltages. To further understand the behaviors of the discharges under high pressures, voltage current characteristics were plotted using gathered data at pressures of 0.345, and 0.689 MPa over gap lengths of 50, 100, 150 and 200 μm in Nitrogen.

Once the collected data was plotted, it yielded a negatively sloped portion as well as a flat portion of V-I curve, both highlighted in later figures. The negatively sloped portion of the plots signifies the self-pulsing mode of the plasma discharge while the horizontal portions represent the steady state operation where the plasma is regarded as a normal glow discharge. Optical Emission Spectroscopy was used to obtain temperature readings of the discharges. The rotational and vibrational temperatures of the microplasma discharge were estimated using a customized temperature model compared with experimentally acquired spectra (using emission spectroscopy) from the microplasma system. Table 4 summarizes the effects increased pressure had on both the discharge diameter and the rotational temperature.

Table 4: Discharge size and temperature variation with increasing Nitrogen pressure [16]

Discharge size and temperature variation with nitrogen pressure			
Discharge Current = 0.5 mA, R= 2.1 MΩ, d= 150 µm			
Pressure (MPa)	Discharge Voltage (V)	Discharge Size (µm)	Rotational Temp (K)
0.103	312	41	1186
0.207	324	35	1463
0.345	327	34	1652
0.517	332	28	2361
0.621	334	22	2682
0.827	322	13	2666
1.034	323	12	2728
1.241	325	10	2822
1.379	325	9	2840
1.655	324	7	2894

6.2 Effects of Pressure on Breakdown

As seen in Paschen Law, changes in pressure have a direct relation with discharge breakdown and sustainability voltages. Breakdown voltage is increased almost proportionally with the increase in the product of pressure and electrode gap spacing, Pd in Torr-cm. Similarly, increase in pressure lead to an increase in discharge current densities. Thus pressure also has an effects on overall plasma discharge Voltage-Current measurements.

6.2.1 Effects of Pressure on Breakdown and Sustainability Voltages

Breakdown voltages in Nitrogen were studied under varying pressures and varying gap lengths in order to further the understanding of the effects pressure had on the discharge characteristics. Testing was carried out at gap lengths of 5 µm up to 1000 µm

at pressures of 0.101 MPa, 0.474 MPa, 0.819 MPa, 1.508 MPa and 1.853 MPa and breakdown voltages were collected for each pairing of pressure and gap length resulting in a Pd value which would be used to plot the Paschen curve seen in figure 31. As was expected, breakdown voltages increased with the increase in pressure. As pressure increased, breakdown voltages were found to increase at a faster rate once gap lengths were greater than ~45 μm, showing that pressure changes had greater effects on the breakdown voltages as the gap length increased. As pressure was increased further and the discharge gap was small, Pd values were achieved that are usually achieved through the combination of low pressure and large gap lengths. At these same Pd constituting of extremely high pressures and incredibly small discharge sizes, achieved breakdown voltages were as expected and as is seen in Pd values obtained at large gap lengths and low pressures. After breakdown was achieved the voltage was lowered causing the discharge to become voltage limited and the sustainability voltages were recorded. Overall sustainability voltage trends showed a positive relationship with pressure and steadily increased with the increase in pressure. Currents after breakdown were additionally looked at in order to gain an understanding of power requirements at breakdown. As was the case with the voltages, currents once breakdown occurred showed a positive relationship with pressure and increased in magnitude at a roughly equal rate as the increase in breakdown voltage.

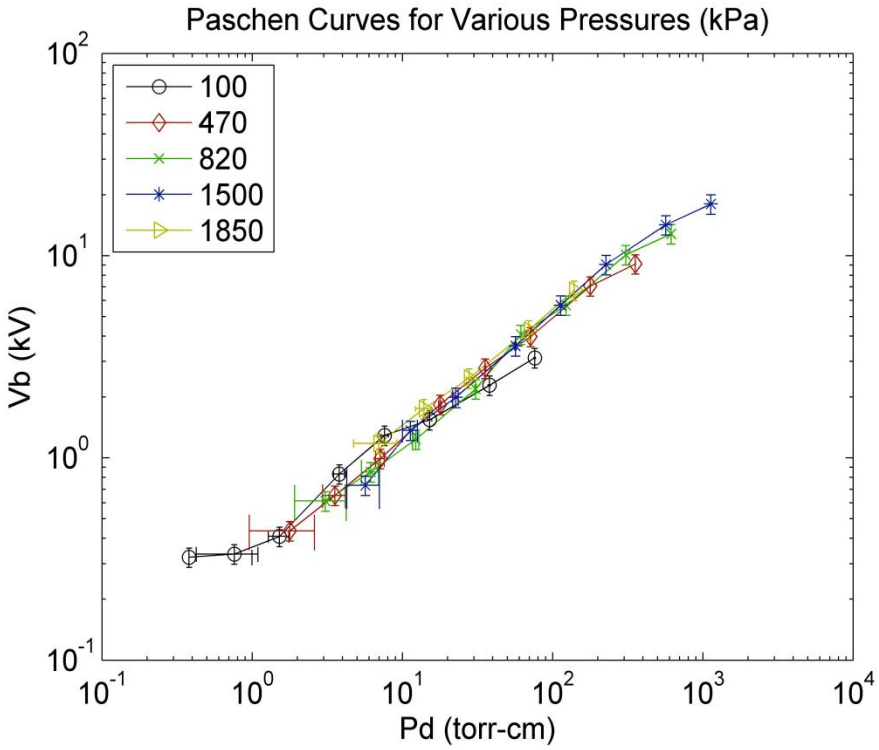

Figure 31: N2 Paschen curves plot

Error bars were constructed in order to account for error and potential offsets in the testing equipment. The observed offset with the pressure reading was approximately an 8.34% error while the calculated error in the electrode spacing was approximately 4.67%, yielding an overall Pd error of 9.56%, represented by the horizontal error bars. Breakdown voltage reading was calculated for the same Pd value 30 times in total and both the average breakdown voltage and the standard deviation in the breakdown voltages were calculated. The standard deviation was then divided by the average and a percent error of 5.58% and is represented by the vertical error bars. Looking at the constructed Paschen curve in figure 31, it can be seen that at very high operating pressures and electrode spacing as small as 5 μm, predicted breakdown voltages were

obtained at Pd values that can be generated at lower than atmospheric pressure and larger gap lengths. Thus, although the testing parameters are far past normal levels, particularly for operating pressures, normal like discharge characteristics are achieved at constant Pd values.

6.2.2 Effects of Pressure on Voltage-Current Characteristics

Voltage current data was collected at varying gap lengths and varying pressures in order to construct graphs of the voltage current characteristics of the DC plasma discharge in the normal glow regime in a Nitrogen filled environment. Tests were carried out at both 0.345 MPa and 0.689 MPa while gap lengths were 50 μm, 100 μm, 150 μm and 200 μm. To collect the data at each pressure gap length pairing, the chamber was pressurized to the target pressure and the gap length set and current was maxed out on the power supply to 5 mA to assure current was not the limiting factor and the voltage was slowly ramped up until breakdown occurred. Once breakdown was achieved, the current was then decreased from its maximum achieved current of 4.5 mA to 0.5 mA at increments of 0.1 mA and then brought back up to its maximum value while any hysteresis was recorded. The discharge voltage current characteristics were recorded from the power supply on a LabView program that took into account the ballast resistance upstream of the discharge and recorded the data at a rate of 100 data points per second.

The voltage current curves were plotted for the normal glow discharges in high pressure nitrogen and were used for measuring voltage current characteristics as well as

other basic discharge parameters. As was seen in the Paschen curves for Nitrogen, breakdown voltage increased with increasing pressure, between 0.345 and 0.689 MPa. The sloped portion to the right of the V-I plots shows the self-pulsing mode for the plasma discharge while the flat portions are representative of the normal glow regime of the plasma discharge. Looking at the normal glow regime, it can be seen that the results, in comparison to low pressure normal glow discharges, are very similar despite incredibly high operating pressures. In the normal glow regime of both tested pressures, the discharges seem to have a similar constant value for resistance per unit area of the plasma discharge. This is indicated by the consistent voltage value for the normal glow regime.

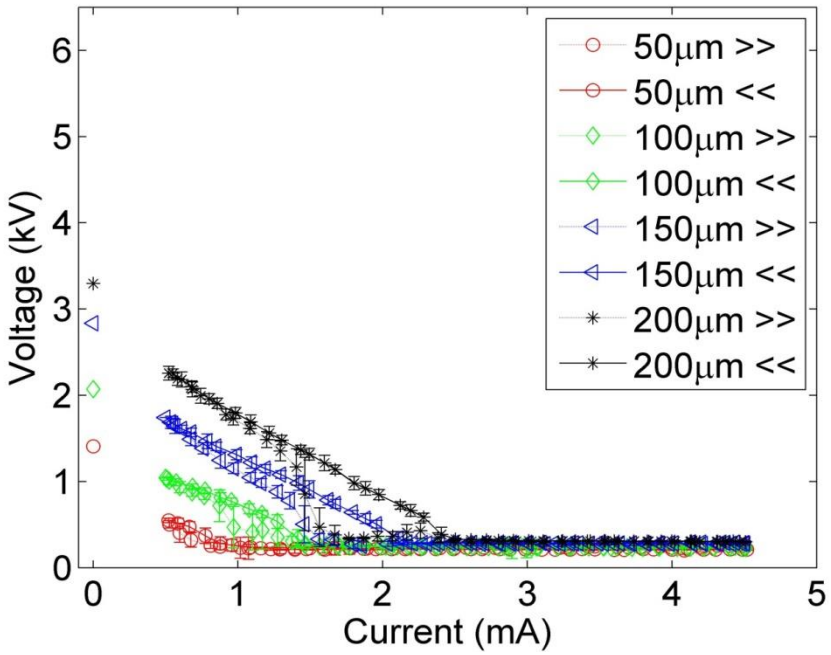

Figure 32: 0.345 MPa V-I characteristic plot in N2

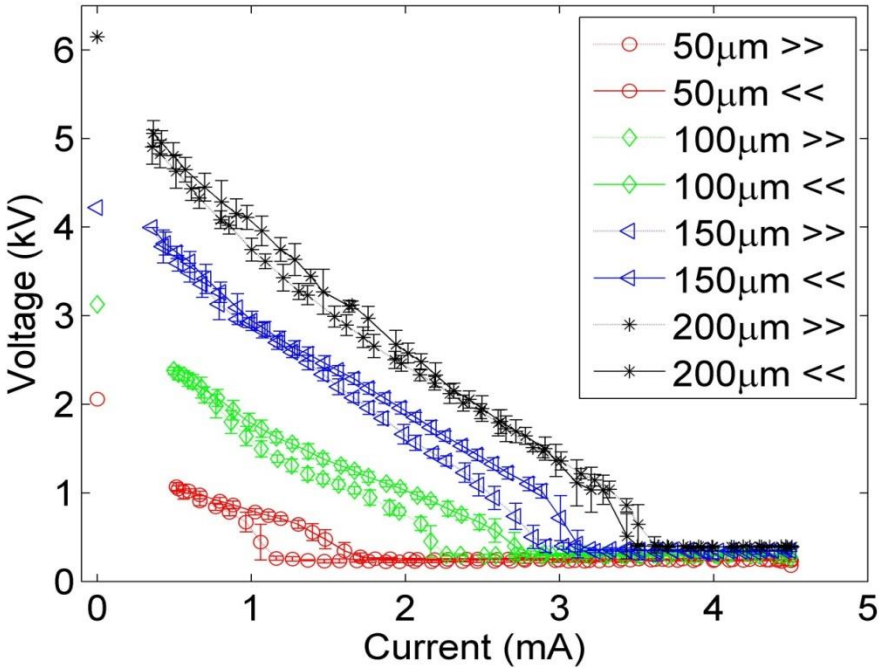

Figure 33: 0.689 MPa V-I characteristic plot in N2

In figure 32 and figure 33 as pressure was increased it can be seen that attainment of a normal glow discharge became more difficult, requiring higher current, thus as pressure was increased while maintaining a constant gap length, the power requirements of the plasma also increased. In addition to the increase in power required, the slope indicating the self-pulsing mode became sharper with the increase in pressure moving from a slope of -0.104 kV/mA at 0.345 MPa to ~ -1.31 kV/mA at 0.689 MPa. Both discharge resistance slopes were calculated using the data obtained from the nitrogen testing at 0.345 MPa and 0.689 MPa at a gap length of 200 μm (top black lines). This increase in the resistance of the discharge may account for the increase in power

required since power and resistance are directly proportional, as seen in equation 10 below [51]

$$P = I^2R \ \ (Eq\ 10)$$

The increase in the grade of this slope indicates an increase in the resistance of the plasma with an increase in the pressure of the surrounding environment. When looking at constant values of Pd for the different pressures, 25.9 Torr-cm and 51.7 Torr-cm, it can be seen that the negative slopes of the self-pulsing mode are constant. This is due to the discharges having the same breakdown voltages at that particular Pd value and similar currents at which the discharge becomes a normal glow. This is further evidence that the characteristics of the discharges are consistent and normal when operating at vastly varying values of pressure and gap lengths that yield a constant Pd value. Figure 34 below illustrates the voltages seen in the normal glow section (flat section) of figure 32 and figure 33 and how they vary with Pd at a current of 4 mA. The same trend of increasing breakdown voltage with increasing Pd values seen in the Paschen curve is seen here where the normal discharge voltage increases from 0.22 kV to 0.30 kV at a pressure of 0.35 MPa along with an increase in Pd, while as Pd increases, normal discharge voltage at 0.69 MPa increased from 0.25 kV to 0.39 kV.

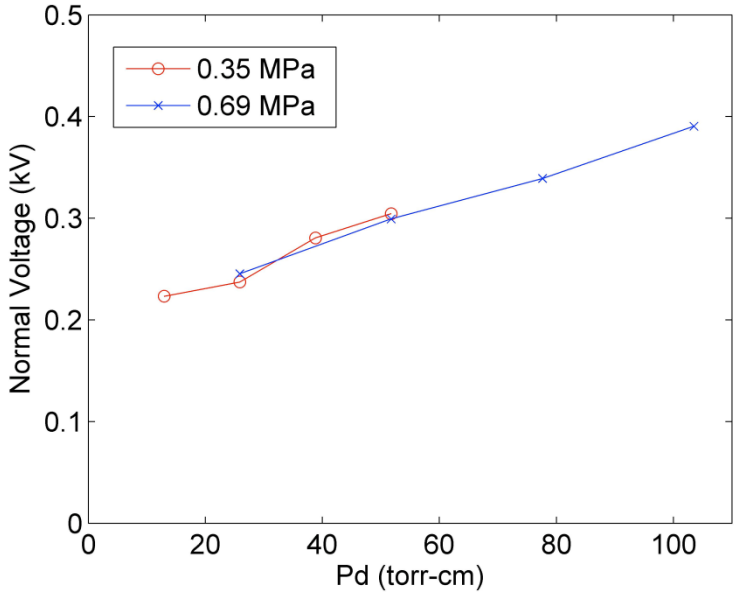

Figure 34: Pd vs normal voltage in Nitrogen at 4 mA current

6.2.3 Effects of Pressure on Discharge Transients

As various experiments were carried out, it was noticed that an increase in pressure can cause a discharge to become unstable. As Voltage Current characteristics of the discharge changed due to pressure, the discharge would enter different regimes due to changing electron emission mechanisms. As the V-I characteristics of the discharge changed and the discharge diameters change, the plasma will transition from switching self-pulsing regime, to a steady state operation and eventually to an Arc Regime.

6.2.4 Breakdown and Switching

As can be seen when comparing the breakdown voltages in figure 32 at 0.345 MPa and the breakdown voltages in figure 33 at 0.689 MPa, breakdown voltage increased with increasing pressure. These results go hand in hand with what was expected in

accordance with Paschen's law. Experiments in different gases were carried out in order to observe effects the operating gas has on the plasma discharge. During testing, the pressure for each gas or gas mixture was increased from 0.104 MPa to 1.01 MPa. At higher pressures breakdown would still occur, yet voltages and currents that yielded stable discharges at lower pressure would yield switching discharges. In order to avoid switching discharges during experiments, the required breakdown voltage and the associated current for the gas or gas mixture at 1.01 MPa was set and used throughput all the experiments.

6.2.5 Transition to Steady State Regime

As can be seen in figure 35 below, there are various regimes a discharge can occur in. Initially, the discharge is in the Dark Discharge section of the plot highlighted between points A-E. In this portion, the discharge is in the Townsend regime, where the gas is being ionized but breakdown has not occurred yet, in this section Coronas will occur between points D-E. As breakdown occur due to secondary electron emission, the discharge moves towards a normal-glow regime in the Glow Discharge portion of the plot.

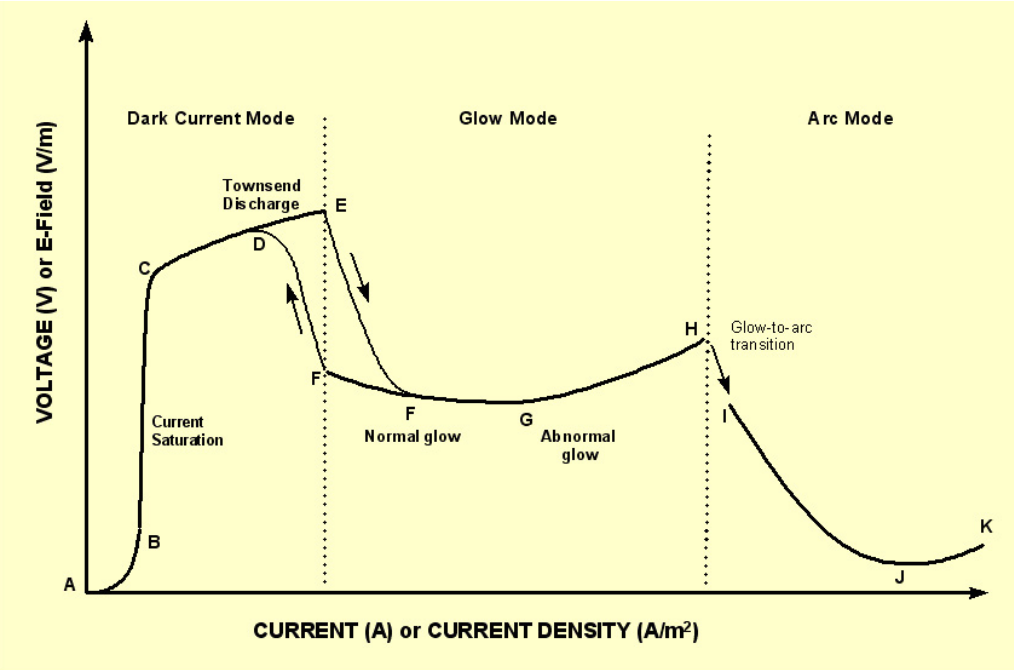

Figure 35: Glow-to-Arc transition, highlighted by points H to I [24]

Figure 36 below highlights experimentally obtained data points for voltage current measurements of the plasma discharge between points E-G in Figure above. The sloped portion of the plot represents the self-pulsing mode where the discharge is transient and switching. As current is increased the discharge moves to the normal glow regime, shown as points F-G in figure 35 above. In the Normal-Glow regime, the discharge has achieved steady state operation, represented by the flat portion of the plot in figure 36 below.

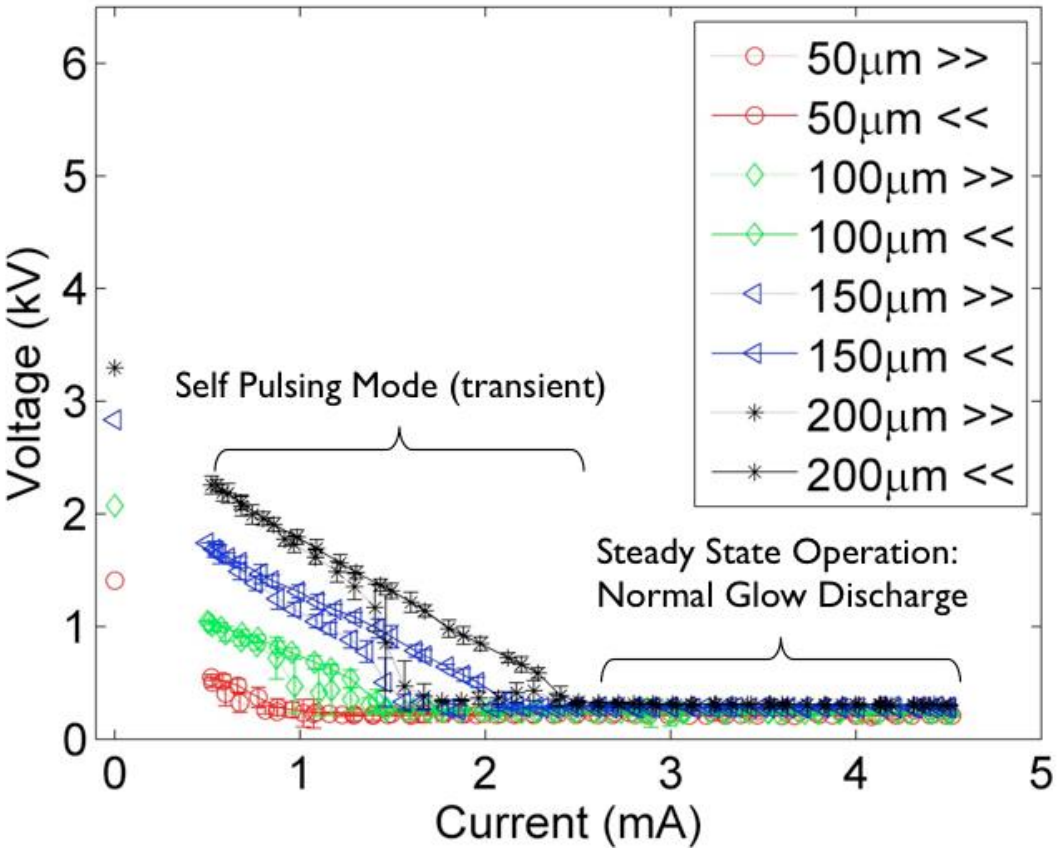

Figure 36: 0.345 MPa V-I plot in N2

As current was increased furthermore plasma temperature continue to rise and the electron emission mechanism goes from secondary electron emission to thermionic electron emission. At this stage, highlighted by point H-I in figure 36, the plasma discharge enters the Arc Discharge regime becoming a Thermal plasma. Increases in pressure tend to cause the plasma discharge to lean towards transmission to the Arc mode.

6.3 Effects of Pressure on Discharge Size

As pressure was changed a negative relationship with discharge diameter was observed. An increased in the working pressure caused the plasma discharge to decrease in diameter. These experiments were conducted in various gases while maintaining constant electrode gap spacing.

6.3.1 Discharge Diameter

Data obtained from previously run experiments carried out in both Helium and Nitrogen show the trend the discharge diameter takes as the testing chamber pressure was changed. Data from Helium testing plotted in figure 37 below, shows the changing discharge diameter as pressure was increased from 0.1 MPa to 0.689 MPa. As pressure was increased the discharge diameter shrunk from 350 μm to 100 μm at a near linear rate.

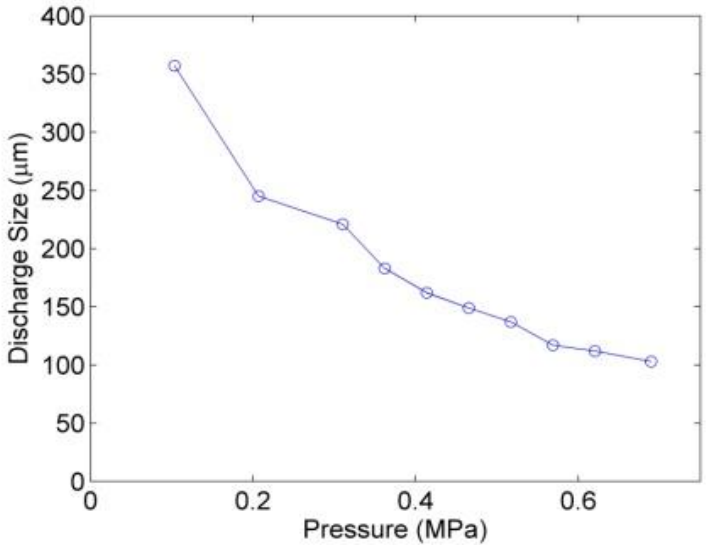

Figure 37: Increased pressure testing in Helium constant electrode gap spacing [16]

A similar trend to that seen in figure 37 above for Helium can be seen in increased pressure testing in Nitrogen discharges. As seen in figure 38 below, Nitrogen testing indicated a decrease in discharge diameter from 88 μm to 26 μm as pressure again was increased between 0.1 MPa to 0.689 MPa. Further testing with increasing pressure, up to 1.66 MPa, shows a minimum diameter of the plasma discharge in Nitrogen of 7 μm. The data presented in figure 37, figure 38 and figure 39 was obtained in previous related experiments carried out by [16]. The data was extracted, verified with further experimentation and then replotted.

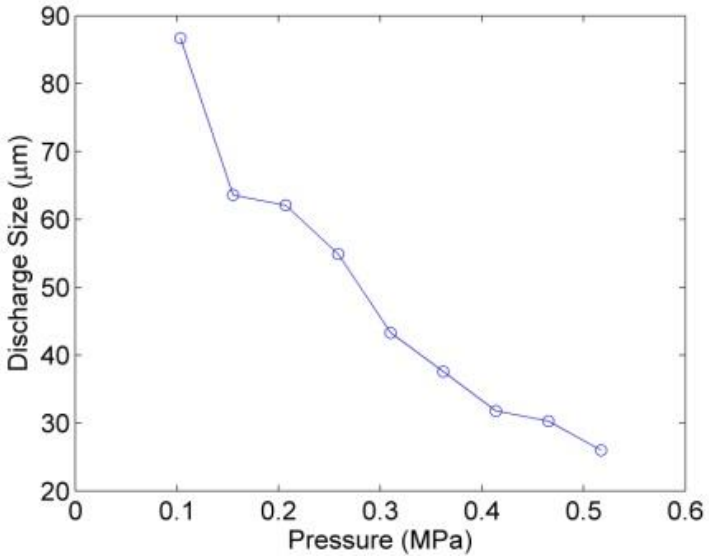

Figure 38: Increased pressure testing in Nitrogen constant electrode gap spacing [16]

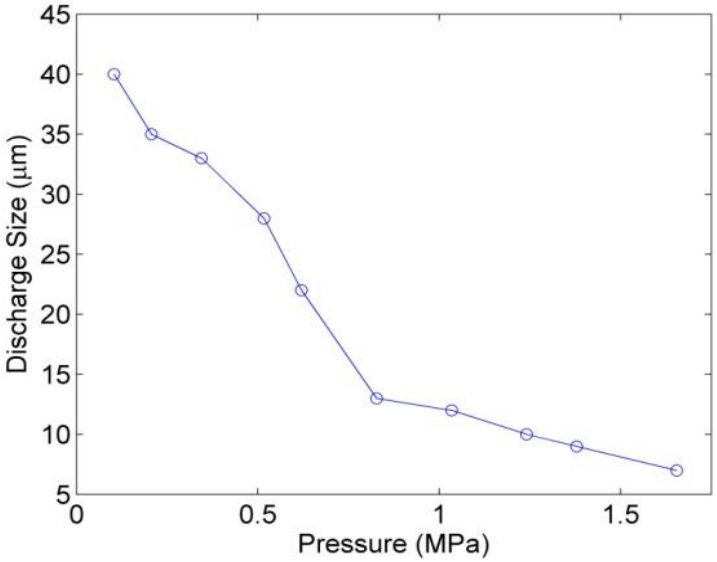

Figure 39: Further increase in working pressure, testing in Nitrogen constant electrode gap spacing [16]

6.3.2 Current and Energy Densities

During experimental testing a positive relation between current density and operating pressure was observed. As the operating pressure in the test chamber as increased, the plasma discharges current density increased. Increasing the pressure caused the discharge diameter to decrease, as stated in the previous section, while the discharge current and voltage remained constant. With constant discharge current and decreasing discharge diameter, the discharge current density increased. This is summed up in table 5 below.

Table 5: Discharge size and current density variation with increasing Nitrogen pressure [16]

Discharge size and Current Density variation with increasing nitrogen pressure		
Discharge Current = 0.5 mA, R= 2.1 MΩ, d= 150 µm		
Pressure (MPa)	**Discharge Size (µm)**	**Normalized Current Density (µA/cm^2*torr^2)**
0.103	41	811.6
0.207	35	403.3
0.345	34	208.2
0.517	28	262.6
0.621	22	381.1
0.827	13	606.7
1.034	12	477.1
1.241	10	510.6
1.379	9	517.1
1.655	7	616.4

6.4 Effects of Pressure on Discharge Temperature

Previous and current studies have shown changes in pressure yield changes in temperatures associated with the plasma discharges. Increase in pressure has shown a

trend towards and eventually achieving thermal equilibrium. This is due to higher levels of particle confinement under high pressure. With higher particle densities, collision frequency is increased thus allowing for energy to be exchanged a thermal equilibrium to be reached.

6.4.1 Rotational and Vibrational Temperatures

With increase in pressure, there was an increase in the rational temperature of the plasma while vibrational temperature decreased. After the initial upward sloping region in the rotational temperature, the temperatures converged towards almost equal values. The change of the rotational and vibrational temperature and their convergence is evident in Figure below where the rotational temperature rise was from 1200 K to 2900 K and the vibrational temperature dropped from a maximum of 4200 K to 3070 K. At pressure values greater than 0.689 MPa, the rotational temperature and vibrational temperatures are measured to be extremely close to each other, within about 500 K. This result points towards a transition of the plasma from a non-thermal non-equilibrium plasma to an equilibrium plasma with rotational and vibrational temperatures comparable to each other. The attainment of thermal equilibrium is due to higher particle densities due to the increased pressure leading to higher collision frequencies and more energy transfer. The data in figure 40 and table 6 below were collected in related previous studies [16] studied and replotted for the projects experimental purposes.

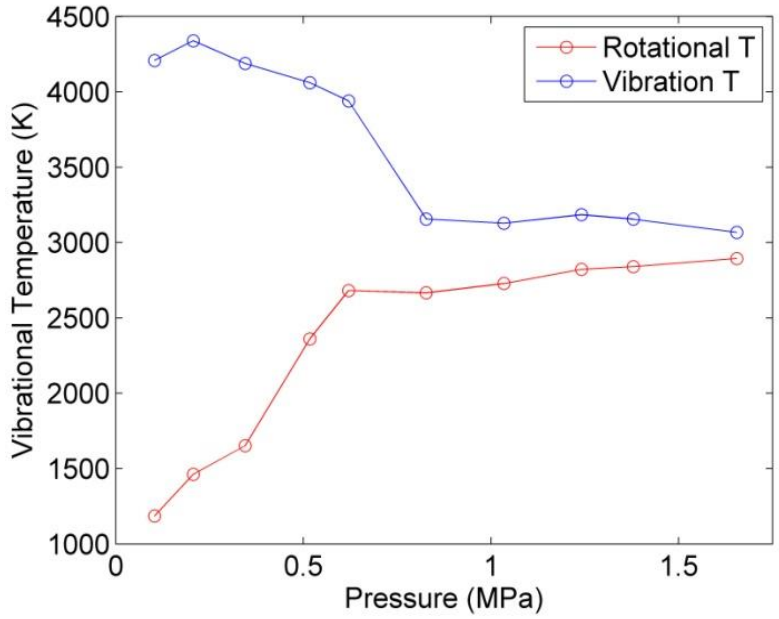

Figure 40: Rotational and vibrational temperatures attainment of thermal equilibrium [16]

The results from the spectral analysis are summarizes in table below with the overall variations in pressure observed in Nitrogen. While the discharge current was kept constant at 0.5 mA, there was a decrease in the discharge size with an increase in the pressure. Along with the decrease in discharge size, an increase in the plasma's rotational temperature was observed while the vibrational temperature decreased. The rotational temperature went from 1186 K to 2894 K over the 0.103 to 1.655 MPa pressure range investigated. Vibrational temperature decreased to 3068K at 1.655 MPa after remaining greater than 4000 K till 0.621 MPa. The trends in the change of the rotational and vibrational temperatures are graphically presented in figure 40.

Table 6: Variations with increasing Nitrogen pressure [16]

Discharge size and temperature variation with increasing nitrogen pressure				
Discharge Current = 0.5 mA, R= 2.1 MΩ, d= 150 μm				
Pressure (MPa)	**Discharge Voltage (V)**	**Discharge Size (μm)**	**Rotational Temp (K)**	**Vibrational Temp (K)**
0.103	312	41	1186	4208
0.207	324	35	1463	4339
0.345	327	34	1652	4187
0.517	332	28	2361	4061
0.621	334	22	2682	3940
0.827	322	13	2666	3156
1.034	323	12	2728	3128
1.241	325	10	2822	3185
1.379	325	9	2840	3155
1.655	324	7	2894	3068

7. EFFECTS OF GASES ON MICROPLASMA DISCHARGES

7.1 Chapter Summary

The type of gas a discharge occurs in effects the characteristics of the discharge just like the pressure of the environment the discharge occurs in. As can be seen by looking at the Paschen curve in figure 1, breakdown voltages vary depending on the ambient gases. In addition to breakdown and sustainability voltages plasma characteristics such as power requirements, stability, discharge size and switching frequencies are affected by the ambient gas. Experiments carried in Nitrogen revealed that discharges became more stable with increasing pressure. In addition, when comparing discharges with the same parameters such as Voltage and Current as well as electrode spacing and pressure, higher current and energy densities occurred in discharges in Nitrogen than did in Helium discharges. Again under similar testing conditions between Nitrogen and Helium smaller discharge diameters were achieved in Nitrogen, down to 7 um, then in Helium with the smallest discharge diameter of 17 μm in comparison. On a diagnostic stand point, Nitrogen testing provided temperature readings with the use of OES due to the second positive band of Nitrogen. A comparison of the gas temperatures in normal glow discharges between Helium and Nitrogen shows that Nitrogen has a higher gas temperature than Helium, believed to be due to the higher number of internal energy modes in Nitrogen in addition to the higher thermal conductivity of Helium.

Other aspects of testing in different gases to keep in consideration were the effects the gases have on the electrodes themselves and not just the plasma discharges.

Experiments run in air would cause the electrodes to oxidize and in some cases sputter and burn away. These issues to some degree can be avoided by running the discharge in an inert gas such as Nitrogen or Helium. Ambient gases also play a key role in the plasma temperatures which in turn plays a key role in the electrode temperatures themselves. Experiments run in Argon caused degradation and pitting to occur on the electrode surfaces, specifically the cathode, due to the high atomic mass of the Argon atoms. Issues that may arise when testing in Hydrogen rich environments occur when Hydrogen is ionized to become a hydride, H- an anion of Hydrogen which can bond with metals and metalloids

7.2 Optical Emission Spectroscopy in Different Gases and Gas Mixtures

Experiments were carried in varying gases and gas combination in order to gain an understanding of the affects the ambient gas has on the discharge. Tests were run in a variety of gases at a constant electrode gap spacing of 20 μm. The pressure of each gas and gas combination was varied from 0.104 MPa to 1.01 MPa. Optical Emission Spectroscopy was taken for each experimental run and results were plotted showing wavelength emittance v.s a relative intensity of the emitted wavelengths. The results of these experiments are presented in the following sections.

7.2.1 OES of 100% N2

As can be seen in figure 41 below, as pressure was increased it is clear that the discharge's relative intensity decreased. The relative intensity is a measure of how much light was shed from the discharge. As the discharge diameter decreased due to increasing

pressure from 0.104 MPa to 1.01 MPa, the discharge emitted less light thus lowering its relative intensity. The dominant lines seen in figure 41 below having the highest relative intensity are due to the N2 2nd positive system. The N2 2nd positive system ranges from 300 nm to 420 nm [17,"12,15]. The second set of relative peaks occurs between 600 nm and 900 nm and is attributed with the N2 1st positive system.

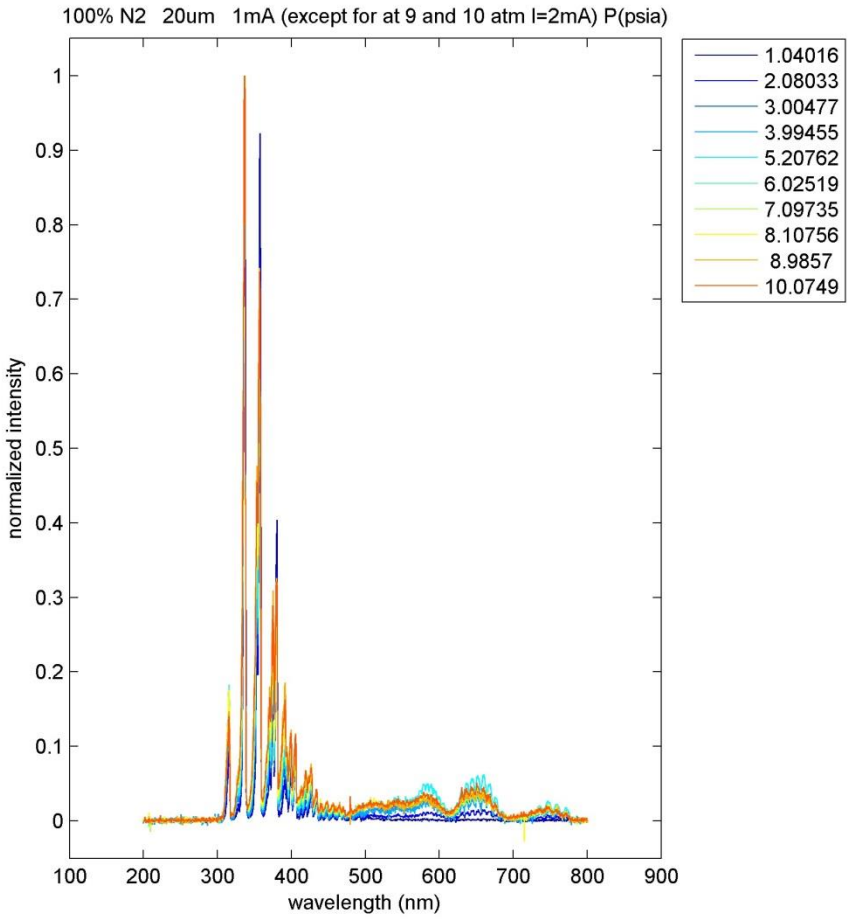

Figure 41: 100% N2 OES, 0.104 MPa to 1.01 MPa

7.2.2 OES of 1% N2 99% H2, He and Ar

Testing in various gases was carried out to obtain spectral emission lines from plasma discharges in those gases. Nitrogen was introduced into the gas to make a mixture containing 1% N2 by volume. This was done to take advantage of N2's 2nd positive system for temperature measurements. As can be seen in figure 42 below, the strongest standing lines yielding the highest relative intensities are associated with atomic Hydrogen and are due to the Balmier series. These are visible at 400 to 600 nm, specifically 656 nm. Peaks due to N2 2nd positive column are still evident in the 300 to 400 nm range. Again, as noticed in figure 41 above with the increased pressure Nitrogen testing, as pressure was increased from 0.104 MPa to 1.01 MPa, the relative intensities of the peaks decreased. This is again due to decreasing plasma discharge diameters, thus emitting less intense light. Stability issues occurred when obtaining OES for 99% Hydrogen at 8.1 MPa to 1.01 MPa. This will be revisited in future work.

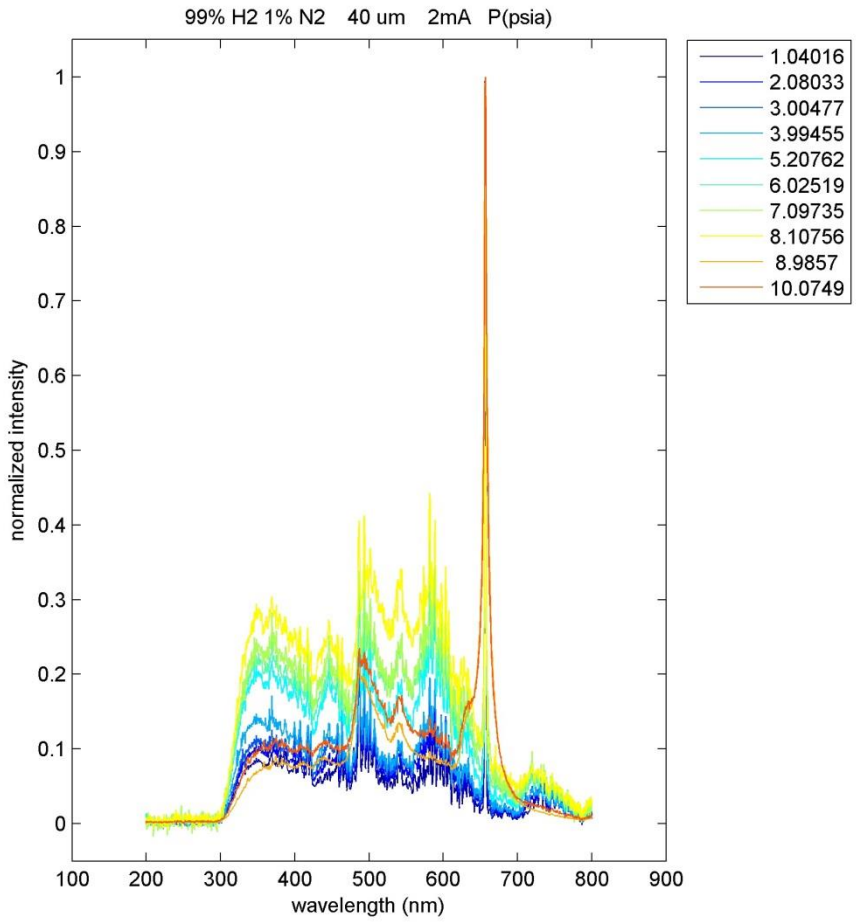

Figure 42: 99% H2 - 1% N2 OES, 0.104 MPa to 1.01 MPa

Optical Emission Spectroscopy was taken for plasma discharges in a gas mixture of 99% He and 1% N2. The most dominant peak occurs at 300 to 400 nm range due to the occurrence of the 1% N2. Less dominant but relative high intensities at 587 nm, 667 nm and even smaller at 706 nm can be seen to some degree in figure 43 below. These peaks are due to the atomic emissions of Helium. The Helium used in testing was not of 100%

purity. The use of non-ultra high purity Helium may explain the higher than expected peaks associated with N2 2nd positive column.

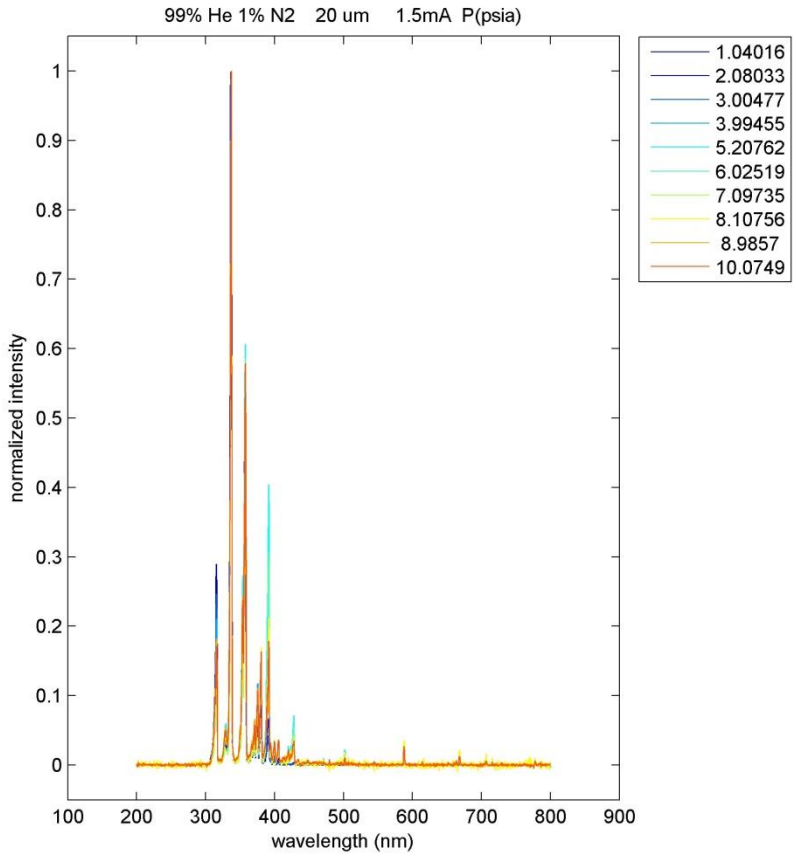

Figure 43: 99% He - 1% N2 OES, 0.104 MPa to 1.01 MPa

OES of Plasma discharges in 99% Argon and 1% Nitrogen was obtained and plotted, this can be seen in figure 44 below. The highest peaks seen are due to Atomic Argon in the 700 nm to 800 nm range. Peaks in the 300 nm to 400 nm range are evident, again due to the mixing with 1% N2.

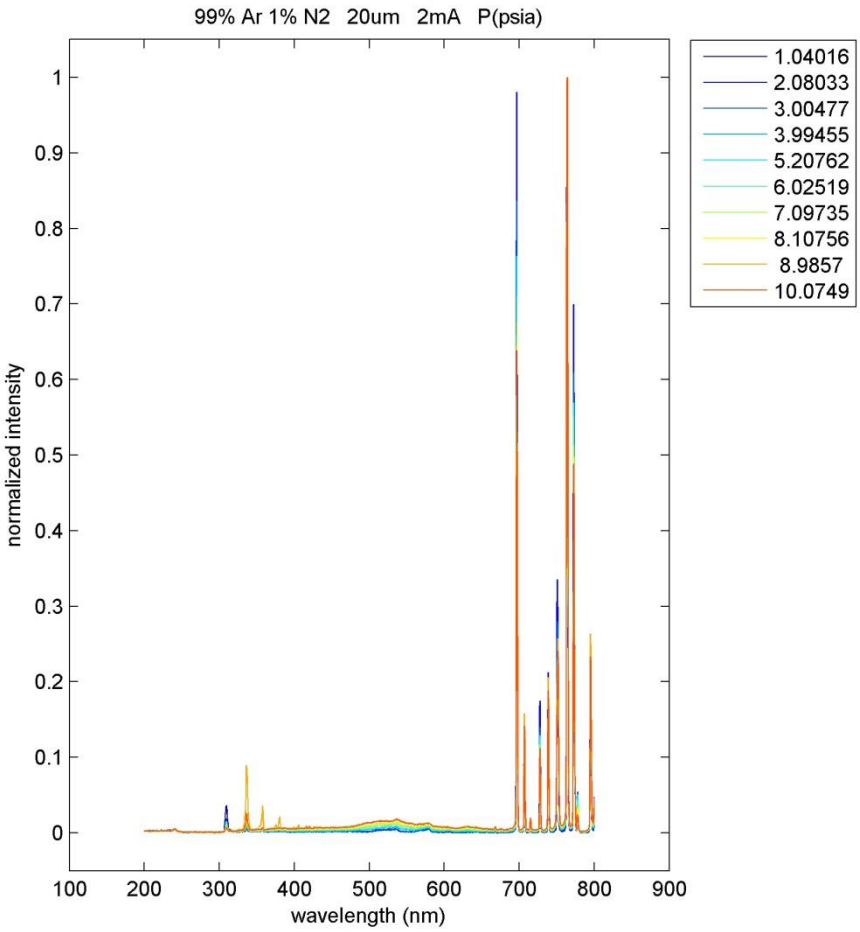

Figure 44: 99% Ar - 1% N2 OES, 0.104 MPa to 1.01 MPa

7.2.3 OES of 1% H2 99% N2, He and Ar

OES of plasma discharges in mixtures of gases with 1% H2 was taken and compiled in the following figures. As was the case with 100% Nitrogen OES and 1% N2 mixture OES, it is evident that the relative intensities of the emitted wavelengths drops as the pressure was increased from 0.104 MPa to 1.01 MPa due to the decrease in the discharge diameters. In very much the same way, the 300 to 400 nm wavelength bands are due to

the N2 2nd positive column. Peaks in the 656 nm region apparent in figure 45 below are due to the excitation of atomic Hydrogen. In figure 47 with 99% Ar - 1% H2, the peaks in the 700 nm to 800 nm range are attributed to the atomic excitation of Argon.

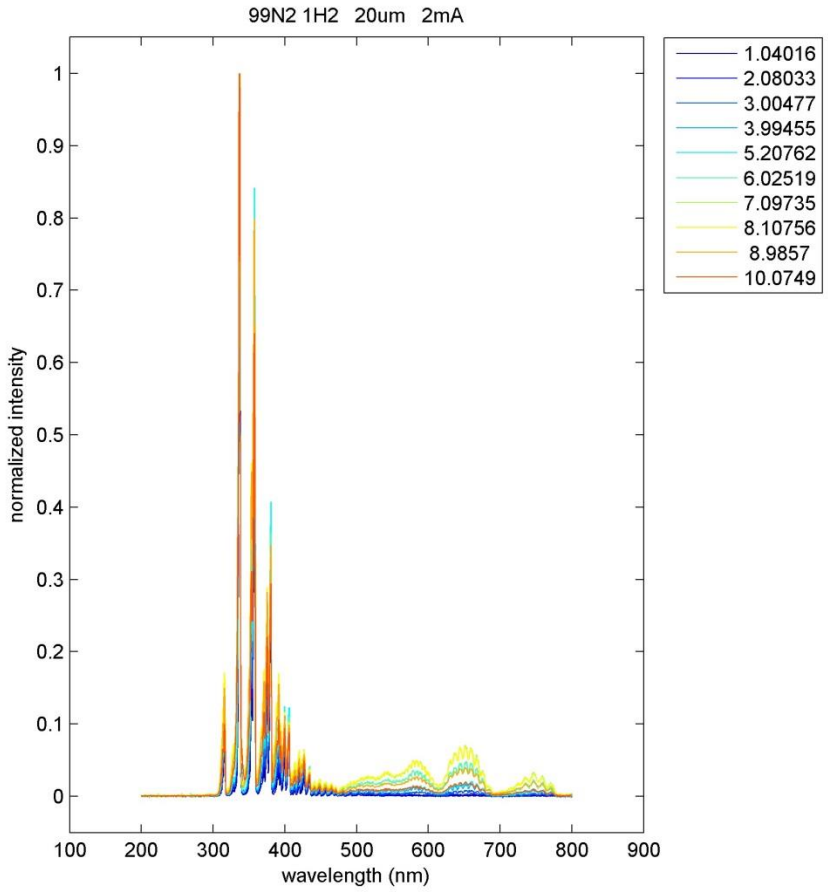

Figure 45: 99% N2 - 1% H2 OES, 0.104 MPa to 1.01 MPa

In the 99% He - 1% N2 OES seen in figure 46, varying intensities of light emitted may be due to impurities in the gas mixture. Impurities may have occurred during the

change of gas lines leading into the chamber and potentially due to improper evacuation old mixtures and recirculation of the new gas inside the chamber.

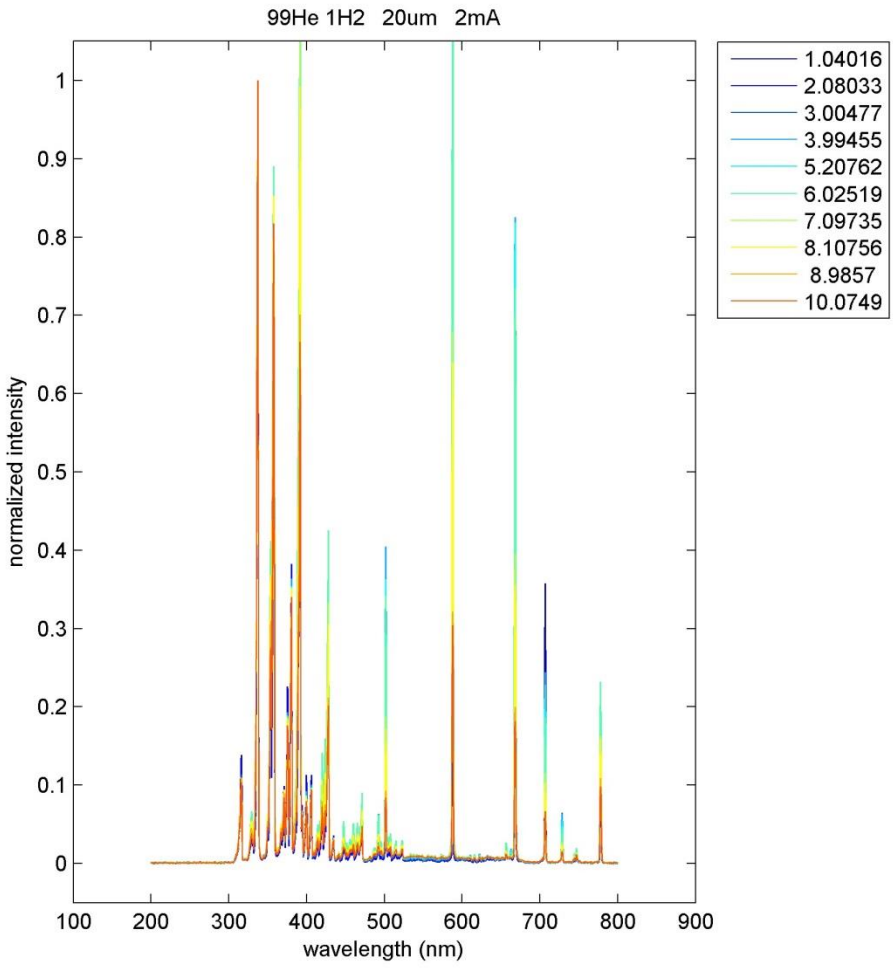

Figure 46: 99% He - 1% H2 OES, 0.104 MPa to 1.01 MPa

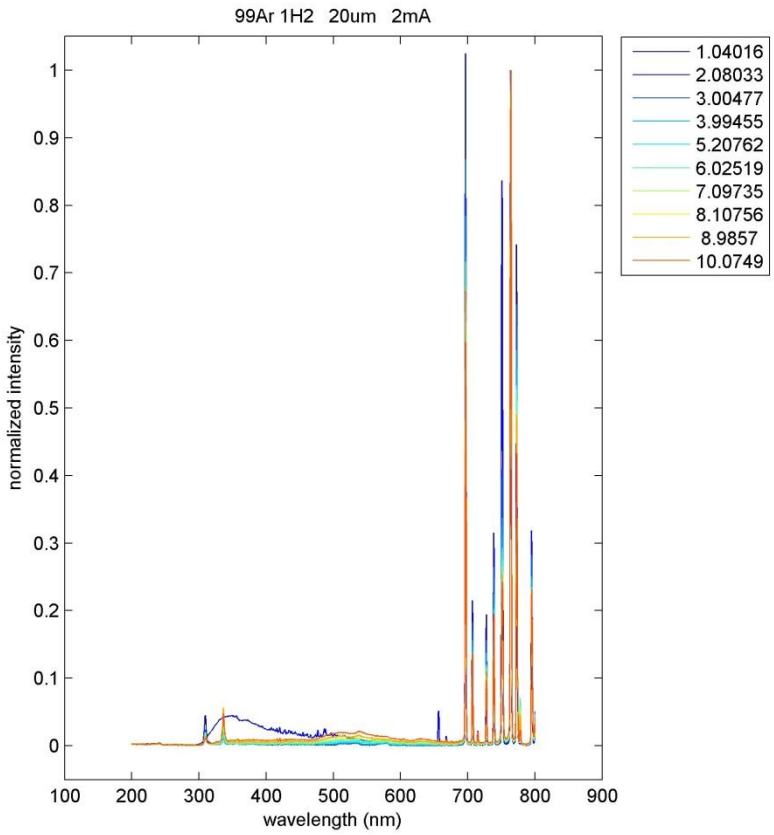

Figure 47: 99% Ar - 1% H2 OES, 0.104 MPa to 1.01 MPa

7.3 Current and Energy Densities

Under similar pressures and similar plasma discharge currents, discharges in Helium have larger diameter negative glows. Similar currents with larger negative glow diameters mean lower current densities. Previous experimentally collected data pertaining to discharge current densities and the varying pressure in both Helium and Nitrogen are presented in figure 48 and figure 49 below and compared. Looking at the

change in discharge voltage with the change in pressure, it can be seen that the discharge voltage changes were minimal, showing that the discharge is still in the Glow Regime.

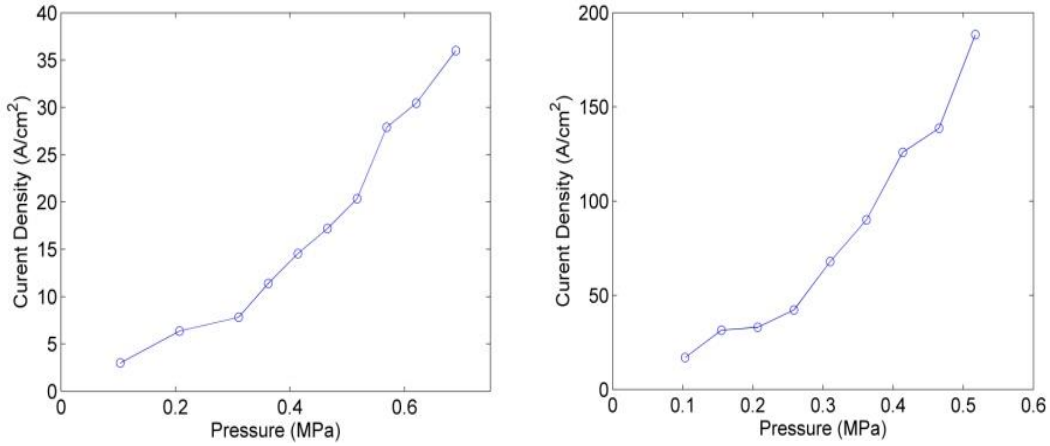

Figure 48: Effects of gas on discharge current density (He left and N2 right) [16]

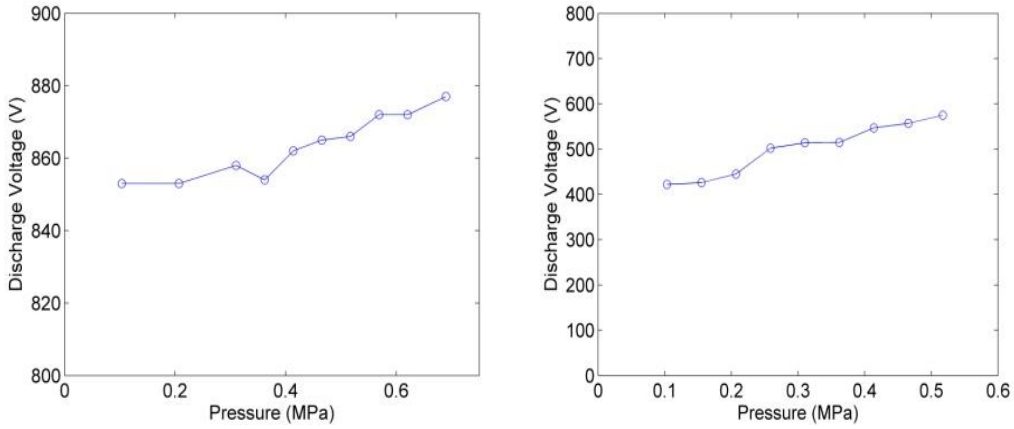

Figure 49: Effects of gas on discharge voltage (He left and N2 right) [16]

7.4 Discharge Stability and Transients

As pressure was increased from 0.104 MPa to 1.01 MPa, varying gases caused the discharge to become unstable and somewhat self-pulsing. This yields the trend that some

gases such as H2 may cause the discharge to transition into an unstable regime. Further testing in the future will take a closer look at the effects of varying gases and gas mixtures on discharge transients.

7.5 Discharge Temperatures

The use of N2 2nd positive system allowed temperature measurements to be made for the discharge occurring in varying gases and gas mixtures. As is the case with many materials such as solids and liquids, different gases have differing thermal conductivities. As an example, similar powered discharges in Helium are of a lower temperature than those in Argon due to Helium's higher thermal conductivity. Energy transfer due to molecular modes and also has its effects on the temperature of the plasma discharges. In Argon mixtures, the difference between the relative peaks at 700 nm and 770 nm can yield information about discharge temperatures.

8. SUMMARY

8.1 Research Objectives

a) A microscale plasma transistor capable of high speed switching was manufactured using microfabrication techniques and operated using microplasma discharges. Such a device must be robust against spikes in power and high temperatures as well as electromagnetic interference and capable of low cost production through microfabrication.

b) Small diameter wires placed on substrate surfaces will be used as electrodes. This will serve the purpose of testing the microplasma discharges while making substrate and electrode material selections.

c) Device feature sizes are on the order of 20 μm and will be achieved utilizing microfabrication techniques. Photolithography coupled with thin film deposition using metal evaporation and electroplating will be used to achieve small device feature with great consistency.

d) Direct Current (DC) plasma discharge characteristics will be investigated under varying pressures from atmospheric to 1.65 MPa while varying current and electrode gap spacing. Testing will be carried out in a high pressure test chamber fitted with a micrometer for variable electrode spacing and gas inlets and outlets for varying the working gas and pressure

e) Discharge V-I measurements along with micrographs and optical emission spectroscopy will be taken for discharges in the varying gases and pressures. These

will be used as diagnostic tools for discharge electrical characteristics, size measurements and temperature measurements.

Robust substrate and electrode materials must be used to insure long device lifetime. High temperature ceramics with high thermal conductivity and high electrical resistance will serve as sufficient substrate material capable of withstanding discharge temperatures. High temperature metals with high thermal and electrical conductivity will serve as device electrode. Superficial oxide layers will increase electrode robustness to discharge temperatures and act as a dielectric barrier to stabilize the discharges and compensate for stray capacitance

8.2 Work Accomplished and Results

The work accomplished throughout this research was a combination of both aspects of the project; (1) the Microplasma properties and (2) manufacturing of the Microscale Plasma Device. The following is a brief summary of work accomplished and results obtained.

(1) The Microplasma and its properties:

a) Stable self-sustaining microplasma discharges exhibiting glow discharge-like characteristics were achieved in various gases and gas combinations, as presented in Chapter 6, in pressures ranging from atmospheric to 1.65 MPa.

b) Discharges with diameters as small as 7 μm have been achieved in Nitrogen and 16.7 μm in Helium by operating at low current, 0.5mA, and at pressures of 1.65 MPa and 0.34 MPa respectively. Paschen type, Pd, scaling was observed in breakdown

voltages, steady state voltage, and discharge size in the tested pressure range from 0.1 MPa to 1.65 MPa.

c) Discharge voltage and current measurements were taken and V-I plots were constructed at 0.345 MPa and 0.689 MPa in Nitrogen. As can be seen in the V-I plots (figure 32 and figure 33) the discharges operated in a normal glow regime, without entering an abnormal glow regime or transitioning to an arc. The discharges exhibited approximately constant normalized current densities and relatively flat voltage current characteristics again indicating normal glow discharge behavior in the microplasmas.

d) Testing was carried out at gap lengths of 5 μm up to 1000 μm at pressures of 0.101 MPa, 0.474MPa, 0.819MPa, 1.508MPa and 1.853 MPa. Breakdown voltages were collected for each pairing of pressure and gap length resulting in a Pd value which would be used to plot the Paschen curve. The data obtained is represented in the Paschen Curve in figure 31. Pd values constituting of extremely high pressures and incredibly small electrode gap sizes, achieved breakdown voltages that were similar to breakdown voltages achieved in Pd values consisting of low pressure and larger electrode spacing. This shows the microplasma discharges achieved in the high pressure chamber at small electrode spacings are scaled down versions of lower pressure glow discharges.

e) Experiments were carried out in both Helium and Nitrogen and show the change in discharge diameter with the change in ambient pressure. As pressure was increased from 0.1 MPa to 0.689 MPa in Helium the discharge diameter shrunk from 350 μm to 100 μm at a near linear rate. Nitrogen testing indicated a decrease in discharge

diameter from 88 μm to 26 μm as pressure again was increased between 0.1 MPa to 0.689 MPa, while further Nitrogen testing with increasing pressure, up to 1.66 MPa, shows a minimum diameter of the plasma discharge in Nitrogen of 7 μm.

f) Related previous testing indicates the attainment of thermal equilibrium in the discharge between Rotational and Vibrational temperatures, ~2800 K, with increasing pressure from atmospheric to 1.65 MPa. Thermal equilibrium was achiever without a Glow-to-Arc transition occurring.

(2) Manufacturing of the Microscale Plasma Device:

a) During the device material selection phase of the project, Aluminum Oxide (Alumina, Al_2O_3) was the initial choice to be used as a suitable substrate due to its low electrical conductivity and a high melting point.

b) Initial testing for electrode material started off by using 50 μm gold, silver, platinum and tungsten (Au, Ag, Pd, and W) wires. The wires were placed on the substrate surface and aligned with one another with an electrode gap spacing of 20 μm to 200 μm. Early testing revealed that the wires over heated and deposited material onto the substrate surface. An alloy consisting of Pt-13%Rh (87% Platinum and 13% Rhodium) was eventually chosen as the material to be used for small diameter wire testing due to its high melting point and high thermal and electrical conductivity. Three electrode configurations, a high voltage source electrode, a gate electrode and a source drain electrode were eventually assembled out of Pt-13%Rh wires and used to have control over the switching initiation, i.e frequencies.

c) In the move towards accurate and consistent microfabrication techniques, photolithography coupled with metal vapor deposition and electroplating were utilized.

d) Aluminum, Nickel, Copper and Titanium were deposited onto Alumina (Al_2O_3) and Ceria Stabilized Zirconia (CSZ) ceramic substrates. Where only CSZ substrates were used during thick film deposition, over ~0.8 μm film thicknesses, due to film delamination on Alumina substrates as a result of higher surface roughness and potentially mismatched coefficients of thermal expansion.

e) The photolithography coupled with thin film deposition using metal evaporation and electroplating resulted in electrodes with features and electrode gap spacing on the order of 25 μm and film thicknesses of 35 μm.

f) Superficial oxide layers on the Aluminum, Copper and Titanium electrodes were formed after being placed in an oven. The oxide layers increased electrode robustness and acted a dielectric barrier stabilizing the plasma discharges and compensating for stray capacitance from the external circuit.

Thick film and thick film with superficial oxide layer testing is summed up in table 2. The best results occurred in both Titanium-Titanium Oxide and Copper-Copper Oxide electrodes where currents and voltages achieved were 1 mA - 3 kV and 1 mA - 3.3 kV, respectively. After several minutes (6+ min) of testing, no electrode sputtering or melting was noticed.

8.3 Conclusions

8.3.1 Plasma Discharge

DC plasma discharges were investigated under pressure varying from atmospheric to 1.65 MPa He and N2 while varying both current and electrode spacing from 0.1 mA to 2 mA and 5 μm to 250 μm, respectively. The discharges were diagnosed by looking at OES imaging to obtain temperature measurements as well as obtaining voltage current measurements and plotting Paschen curve data in order to further understand the effects operating pressure has on discharge characteristics. The effects pressure changes had on the plasma discharges were studied and the operational characteristics and temperatures were investigated. The purpose of these investigations was to further understand the effects pressure as well as current have on microplasma discharge size, current densities and voltages in addition to studying the transition of the discharge from a non-equilibrium discharge to being at thermal equilibrium. Vibrational and rotational temperatures were observed in Nitrogen around 0.862 MPa without transition to an arc from a normal glow mode. The experiments also took into account optical emission spectroscopy as a plasma temperature diagnostic tool. The rotational and vibrational temperatures of the microplasma discharge were estimated using a customized temperature model compared with experimentally acquired spectra from the microplasma system.

Breakdown voltages in Nitrogen that were studied under varying pressures and varying gap lengths to observe the effects pressure had on the discharge characteristics at

gap lengths of 5 μm up to 1000 μm at pressures of 0.101 MPa, 0.474 MPa, 0.819 MPa, 1.508 MPa and 1.853 MPa were plotted and can be seen in figure 31. The theoretical Paschen curve for Nitrogen seen in figure 1 was plotted along with the experimentally obtained Paschen curve for comparison and is present in figure 50 below. In order to fit the Paschen curves, the secondary electron emission coefficient of the stainless steel cathode was determined to be 0.03.

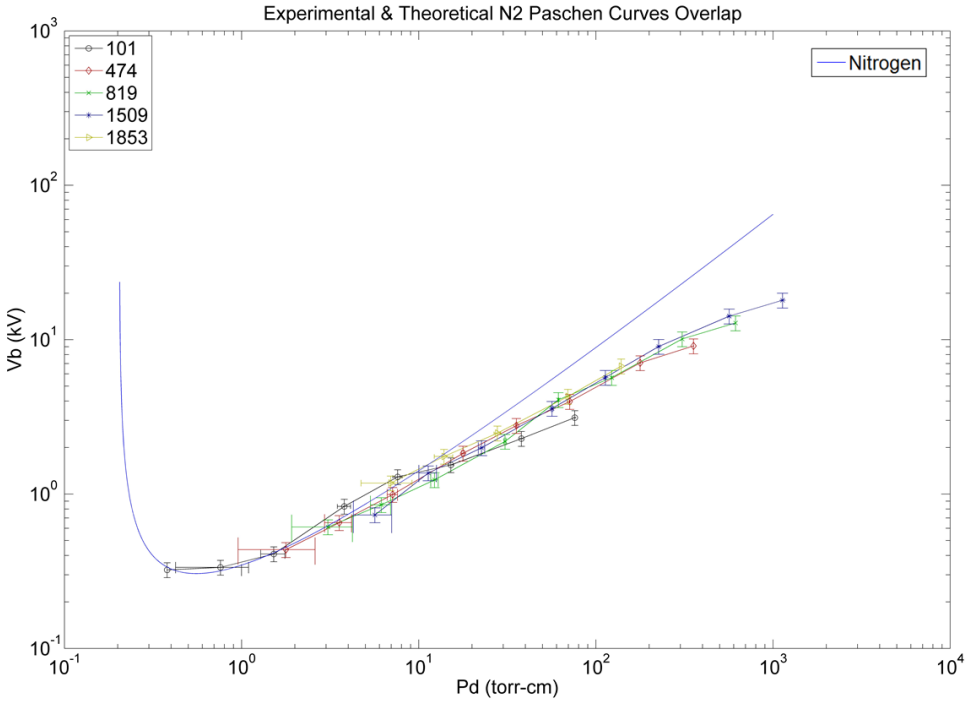

Figure 50: Comparison of mathematically plotted Paschen curve and experimentally obtained Paschen curve

Experiments varying the current to see the effects on the discharge size in Helium were carried out varying the current from 1 mA to 0.1 mA with an overall decrease in

the discharge size occurring, yielding a 16.7 μm diameter discharge at 0.1 mA. This decrease in discharge size, in turn lead to an increase in the current density of the discharge. After setting the current at a constant 3 mA, and varying pressure from 0.103 MPa to 0.689 MPa, the discharge lost its stability as the pressure continued to increase. Variation in discharge size with current at a constant pressure of 0.345 MPa over a gap length of 250 μm gave us a positive sloped relation. The overall change in the discharge size was from 16.7 μm to 80 μm, while little change can be seen in the total voltage change, where the voltage values ranged from 190 to 275 V over the specified current range exhibiting behaviors observed in glow discharges. Pressure variation experiments carried out where the pressure varied from 0.103 MPa to 0.689 MPa over a set gap length of 250 μm and a constant current of 3 mA showed a decrease in discharge size from 360 to 100 μm, while the current density increased from $2\,A/cm^2\ to\ 37\,A/cm^2$ with pressure due to the change in discharge size. Discharge voltage remained fairly similar again only changing from ~855 V to ~878 V.

The Nitrogen experiments were carried out at a pressure variance between 0.103 to 0.517 MPa with an electrode spacing gap of 150 μm at 1 mA current. Unlike Helium, the discharge in Nitrogen does not encounter any problems with instability. The discharge size decreased from 87 to 26 μm with increase in the pressure of the Nitrogen gas thus increasing current density from ~15 $A/cm^2$to 185 A/cm^2. Voltage measurements changed showing a slight increase from 420 V to ~580 V. Overall trends observed in Nitrogen tests were similar to those observed in Helium tests where discharge size had a

negative relation to the change in pressure as current density had a positive relation while the voltage remained relatively unchanged.

The experiments in Nitrogen were carried out further while simultaneously performing spectral analysis on the discharges. The microplasma discharge was imaged by microscopic visualization from one optical window while the light from the discharge was captured by Optical Emission Spectroscopy (OES) through the coaxial optical window. The OES instrumentation was used to acquire the spectrum of the microplasma discharge at each step of the pressure variation experiment in the 375 nm to 381 nm wavelength spans. The experiment was carried out in pressures varying from 0.103 MPa to 1.655 MPa with a constant discharge current of 0.5 mA. At first discharge current was held at a constant 0.5 mA. A decrease in the discharge size was observed with an increase in the pressure. Along with the decrease in discharge size, an increase in the plasma's rotational temperature was observed while the vibrational temperature decreased. The rotational temperature went from 1186 K to 2894 K over the 0.103 MPa to 1.655 MPa pressure range investigated. Vibrational temperature decreased to 3068K at 1.655 MPa after remaining greater than 4000 K till 0.621 MPa. A minimum discharge size of 7 μm was achieved at 1.655 MPa while the current was held constant at 0.5 mA. With increase in pressure, there was an increase in the rational temperature of the plasma while vibrational temperature decreased. After the initial upward sloping region in the rotational temperature, the temperatures converged towards a saturation value almost equal to each other. The decrease in vibrational temperature coincides with an increase

in the rotational temperature and the two temperatures converge towards a saturation value in which the microplasma goes into being categorized as an equilibrium discharge.

8.3.2 Device and Fabrication

Two wire configurations were set up on Alumina substrates in order test the electrode materials. Wires were initially Ag, Au, Pd and W and were selected as such due to their high electrical and thermal conductivity as well as high melting points, in the case of tungsten. Early testing revealed that wires would overheat and start to melt and sputter onto the substrate surface. Pd-13%Rh alloy wires at diameters of 25 μm and 50 μm were eventually chosen as the material to be used for wire testing. These new wire alloys proved to be robust and could handle the temperatures presented by the discharge. Three electrode configurations were then tested with the Pt-13%Rh alloy wires.

Two electrode configurations were manufactured with the use of photolithography techniques and evaporated metal deposition. Initial metal film thicknesses ranged from 50 nm to 150 nm. Slightly thicker film deposition was achieved by increasing metal evaporation time and the number of evaporation runs. Once tested, plasma discharges would disintegrate the electrodes and melt them away due to still relatively low film thickness and insufficient heat shedding. Thicker and more robust metal films deposition on Alumina were achieved, yet once film thickness became thick enough the film started to have enough internal stresses to cause it to peel back and away from the substrate. This was believed to be due to both Alumina's high surface roughness and mismatched coefficient of thermal expansion. Selection of substrate moved from Alumina towards

Ceria Stabilized Zirconia ceramics. Modifications during evaporation process lead to film thicknesses up to 2 μm. Results of these modified evaporation techniques resulted in deposited metal films with increased robustness, but still unable to withstand extended periods of discharges. Metal films were oxidized in an oven in order to promote the development of a protective oxide layer and speed up a natural occurring process. Titanium-Titanium Oxide and Copper-Copper Oxide electrodes proved to be best thin film deposition results, withstanding 1 mA and 3 kV in the case of Titanium-Titanium Oxide and 1 mA and 3.3 kV for Copper-Copper Oxide for relatively long periods of time and showing no signs of deterioration or degradation. The oxide layers served the purpose of compensating for stray capacitance and acted as dielectric barriers stabilizing the discharges.

Electroplating was used on the thin film deposition starting with a thickness of ~2 μm as an initial conductive surface and increasing its thickness, thus achieving film thicknesses 35 μm. Controlled surface oxidation of these copper electrodes added a protective layer with a high electrical resistance. Future work along these lines is to replicate these experiments and achieve similar results with Pt-13%Rh alloys in place of the copper electrodes

8.4 Future Work

Future work for the project consists of a combination of experiments to be revisited in addition to new experiments. Revisited experiments will achieve the goal of verifying existing experimental results and shedding new light on already visited ideas and

concepts. New experiments will carry on with new material deposition and new electrode patterns.

8.4.1 Testing to Revisit

Experiments to be revisited are the deposition of thicker films of Titanium-Titanium Oxide as well as thicker films still of Copper-Copper Oxides. Moreover, additional optical emission spectroscopy is to be taken to verify acquired spectra. This will be done to insure the gases and gas mixtures are accurate with no impurities introduced between experiments of different gases as well as insure the stability of the discharges during the Spectra acquisition.

8.4.2 Further Steps and Experiments

1. Electroplating of substrates pre photoresist removal.
2. Testing of 35 μm + thickness films with superficial protective oxide layer.
3. Testing of new 2-electrode configurations with varied geometries.
4. Testing of new 3-electrode configurations with varied geometries.
5. Testing of 4-electrode configurations with varied geometries.
6. Additional Optical Emission Spectroscopy at higher end pressure (0.7 MPa to 1.65 MPa)

REFERENCES

[1] “Transistor.” Wikipedia. 14 May 2013 <http://en.wikipedia.org/wiki/Transistor>.

[2] “Solid State Electronic.” Wikipedia. 26 February 2013 <http://en.wikipedia.org/wiki/Solid-state_(electronics)>.

[3] Chen, K.-F., and J. G. Eden. "The plasma transistor: A microcavity plasma device coupled with a low voltage, controllable electron emitter." Applied Physics Letters 93 (2008): 161501.

[4] Hoffmann, Volker. "Application of glow discharge optical emission spectroscopy (GDOES) to the analysis of PVD- and CVD-layers." Fresenius' Journal of Analytical Chemistry 346 (1993): 165-68.

[5] Marcus, R. Kenneth, and W. Clay Davis. "An Atmospheric Pressure Glow Discharge Optical Emission Source for the Direct Sampling of Liquid Media." Analytical Chemistry 73 (2001): 2903-910.

[6] Mitra, Bhaskar, Brandon Levey, and Yogesh B. Gianchandani. "Hybrid Arc/Glow Microdischarges at Atmospheric Pressure and Their Use in Portable Systems for Liquid and Gas Sensing." IEEE Transactions on Plasma Science 36 (2008): 1913-924.

[7] Hopwood, J., F. Iza, S. Coy, and D. B. Fenner. "A microfabricated atmospheric-pressure microplasma source operating in air." Journal of Applied Physics 38 (2005): 1698-703.

[8] Kushner, Mark J. "Modelling of microdischarge devices: Plasma and gas dynamics." Journal of Applied Physics 38 (2005): 1633-643.

[9] Yuan, Wen, and Massood Tabib Azar. "Capacitively coupled atmospheric rf microplasma devices." IEEE Sensors Proceedings 20 (2011): 503-507

[10] Park, S.-J., and J. G. Eden. "13–30 Micron Diameter Microdischarge Devices: Atomic Ion and Molecular Emission at above Atmospheric Pressures." Applied Physics Letters 81.22 (2002): 4127. Print.

[11] Angeli, Johann, Arne Bengtson, Annemie Bogaerts, Volker Hoffmann, Vasile-Dan Hodoroaba, and Edward Steers. "Glow discharge optical emission spectrometry: Moving towards reliable thin film analysis?a short reviewInitially prepared as part of the final report of the EC Thematic Network on Analytical Glow Discharge Spectroscopy, contract SMT4?CT98?7517." JAAS 18 (2003): 670-79.

[12] Tochikubo, F., T. Kokubo, S. Kakuta, A. Suzuki, and T. Makabe. "Investigation of the high-frequency glow discharge in Ar at 13.56 MHz by spatiotemporal optical emission spectroscopy." Journal of Applied Physics 23 (1990): 1184-192.

[13] Bogaerts, Annemie, Renaat Gijbels, and Jaroslav Vlcek. "Modeling of glow discharge optical emission spectrometry: Calculation of the argon atomic optical emission spectrum." Spectrochimica Acta Part B: Atomic Spectroscopy 53 (1998): 1517-526.

[14] Yuan, W., K. N. Chappanda, and M. Tabib Azar. "Microfabricated atmospheric rf microplasma devices for gas spectroscopy." International Conference on Miniaturized Systems for Chemistry and Life Sciences 15 (2011): 568-70.

[15] Staack, David, Bakhtier Farouk, Alexander F. Gutsol, and Alexander A. Fridman. "Spectroscopic studies and rotational and vibrational temperature measurements of atmospheric pressure normal glow plasma discharges in air." Plasma Sources Science and Technology 15 (2006): 818-27.

[16] Chitra, Aditya Rajeev. "Microplasma discharges in high pressure gases scaling towards the sub-micron regime" Thesis. Texas A&M University, 2010. Print.

[17] Staack D, Farouk B, Gutsol A, and Fridman A "DC normal glow discharges in atmospheric pressure atomic and molecular gases" Plasma Sources Science & Technology 17 (2008): 025013 1-13

[18] Staack, David, Bakhtier Farouk, Alexander Gutsol, and Alexander Fridman. "Characterization of a DC Atmospheric Pressure Normal Glow Discharge." Plasma Sources Science and Technology 14.4 (2005): 700-11. Print.

[19] Tirumala, Rakshit, and David B. Go. "An analytical formulation for the modified Paschen's Curve." Applied Physics Letters 97 (2010). 151502 1-3. Print

[20] Boyle, W. S., and F. E. Haworth. "Glow-to-Arc Transition." Physical Review 101 (1956): 935-38.

[21] Go, David B., and Daniel A. Pohlman. "A mathematical model of the modified Paschen's curve for breakdown in microscale gaps." Journal of Applied Physics 107 (2010).

[22] "Plasma Physics: Paschen Curve." PHYWE. 15 May 2013. <Http://www.physics.nus.edu.sg/~L3000/Level3manuals/plasma%20physics.pdf>.

[23] Hosokawa, Masato, Chiharu Noda, Seiji Mukaigawa, Koichi Takaki, and Tamiya Fujiwara. "Dependence of Voltage-Current Characteristics of High-Current Nitrogen Glow Discharge on Gap Length and Gas Pressure." IEEE Transactions on Fundamentals and Materials 125.12 (2005): 993-1000. Print.

[24] "The Plasma Sun." The Sun. 25 April 2013 <http://electric-cosmos.org/sun.htm>.

[25] "Plasma Physics: Paschen Curve." PHYWE. 17 May 2013. <http://www.phywe.com/index.php/fuseaction/download/lrn_file/versuchsanleitungen/P2531100/e/P2531100.pdf >.

[26] Becker, K. H., K. H. Schoenbach, and J. G. Eden. "Microplasmas and applications." Journal of Applied Physics 39 (2006): R55-70.

[27] Kogelschatz, U. "Atmospheric-pressure plasma technology." Plasma Physics and Controlled Fusion 46 (2004): B63-75.

[28] Schutze, Andreas, James Y. Jeong, Steven E. Babayan, Jaeyoung Park, Gary S. Selwyn, and Robert F. Hicks. "The atmospheric pressure plasma jet: A review and

comparison to other plasma sources." IEEE Transactions on Plasma Science 26 (1998): 1685-694

[29] Takaki, K., D. Taguchi, and T. Fujiwara. "Voltage–current Characteristics of High-current Glow Discharges." Applied Physics Letters 78.18 (2001): 2646-648. Print.

[30] Fridman, Alexander A. Plasma chemistry. Cambridge: Cambridge UP, 2008.

[31] Tendero, Christelle, et al. "Atmospheric pressure plasmas: A review." Spectrochimical Acta Part B: Atomic Spectroscopy 61.1 (2006): 2-30.

[32] "Plasma Physics." Wikipedia. 14 May 2013 <https://en.wikipedia.org/wiki/Plasma_(physics)>.

[33] Eijkel J C T, Stoeri H and Manz A 2000 "An atmospheric pressure dc glow discharge on a microchip and its application as a molecular emission detector" J. Anal. At. Spectrom. 15 297-300

[34] Machala, Z., Z. Machala, E. Marode, C. O. Laux, and C. H. Kruger. "DC discharge in atmospheric pressure air in the glow and glow-to-arc transition regimes." International Conference on Gas Discharges and their Applications 14 (2004): 1089-092.

[35] Rajasekaran, Priyadarshini, Cornelia Ruhrmann, Nikita Bibinov, and Peter Awakawicz. "Space resolved characterization of high frequency atmospheric pressure plasma in nitrogen applying optical emission spectroscopy and numerical simulation." Journal of Applied Physics 44 (2011): 1-8.

[36] McKay, K, et al. "Excitation frequency effects on atmospheric-pressure helium RF microplasmas: plasma density, electron energy and plasma impedance." The European Physical Journal. D, Atomic, Molecular and Optical Physics 60.3 (2010):497-503.

[37] Yu. P. Raizer, *Gas Discharge Physics,* (Nauka, Moscow, 1992; Springer-Verlag, Berlin, 1991).

[38] “Electric Glow Discharge”. Plasma-Universe. 08 May 2013 <http://www.plasma-universe.com/Electric_glow_discharge>.

[39] Kanazawa, S., M. Kogoma, T. Moriwaki, and S. Okazaki. "Stable Glow Plasma at Atmospheric Pressure." Journal of Applied Physics 21 (1988): 838-40.

[40] Turner, R. "The glow-to-arc transition in a pulsed high-pressure gas discharge." Journal of Applied Physics 52 (1981): 681-92.

[41] Fan, Hsu Yun. "The Transition from Glow Discharge to Arc." Physical Review 55.8 (1939): 769-75. Print.

[42] Massines, Françoise, Ahmed Rabehi, Philippe Decomps, Rami Ben Gadri, Pierre Ségur, and Christian Mayoux. "Experimental and theoretical study of a glow discharge at atmospheric pressure controlled by dielectric barrier." Journal of Applied Physics 83 (1998): 2950-956.

[43] Gherardi, Nicolas, Gamal Gouda, Eric Gat, Andre Ricard, and Franc ois Massines. "Transition from Glow Silent Discharge to Micro-discharges in Nitrogen Gas." IOPScience (2000) 340-346

[44] Arkhipenko, V. I., A. A. Kirillov, Ya A. Safronau, L. V. Simonchik, and S. M. Zgirouski. "Self-sustained dc atmospheric pressure normal glow discharge in helium: From microamps to amps." Plasma Sources Science and Technology 18 (2009): 1-16.

[45] Du, Beilei, Sebastian Mohr, Dirk Luggenhölscher, and Uwe Czarnetzki. "An atmospheric pressure self-pulsing micro thin-cathode discharge." Journal of Applied Physics 44 (2011): 1-8.

[46] Lutz, Michael A. "The Glow to Arc Transition - A Critical Review." IEEE Transactions on Plasma Science 2 (1974): 1-10.

[47] Duan, Xiaoxi, Feng He, and Jiting Ouyang. "Prediction of atmospheric pressure glow discharge in dielectric-barrier system." Applied Physics Letters 96 (2010): 1-3.

[48] Kito, Y., T. Sakuta, and A. Kamiya. "Thomson scattering of laser light from high pressure air arc discharge and its application to electron density measurement." Journal of Applied Physics 17 (1984): 2283-290.

[49] Edels, H., and W. A. Gambling. "Excitation Temperature Measurements in Glow and Arc Discharges in Hydrogen." Royal Society of London. Series A, Mathematical and Physical Sciences 249.1257 (1958): 225-36.

[50] Stark, Robert H., and Karl H. Schoenbach. "Direct Current High-pressure Glow Discharges." Journal of Applied Physics 85.4 (1999): 2075.

[51] Gray, Alexander. "Chapter 6, section 52." Ed. G. A. Wallace. Principles and Practices of Electrical Engineering. 7th ed. New York: McGRAW HILL, 1955.

APPENDIX

Figure 31 Experimental Paschen Curve Plotting

```
clear
clc
close all


Pmeter = [28.47,35.76,42.53,47.39,
52.48,57.48,61.98,67.28,60.16,76.49,82.08] ;
Pgage =  [10,18,23.5,29,32,38.5,42,48,40,58,64];
Ppsi = Pgage + 14.69;

pp = polyfit(Ppsi,Pmeter,1);


plot(Ppsi,Pmeter,'x')
title(['fitting coef=  ',num2str(pp)])
xlabel('gauge')
ylabel('flow meter')



P=xlsread('PCdataREDO.xlsx','P');
Poffset = pp(2);
Pcorr = P+Poffset*760/14.69;
P(P~=760) = Pcorr(P~=760);
d=xlsread('PCdataREDO.xlsx','d');
X=P.*d;
Y=xlsread('PCdataREDO.xlsx','Vb');

 H= 10/1000*ones(size(Y))
 H = 0.11*Y;
% H= [0.005 0.005 0.005 0.005 0.005 0.005 0.005 0.005 0.005 0.005 0.005
0.005 0.005 0.005 0.005 0.005 0.005 0.005 0.005 0.005 0.005 0.005 0.005
0.005 0.005 0.005 0.005 0.005 0.005 0.005 0.005 0.005 0.005 0.005 0.005
0.005 0.005 0.005 0.005 0.005]
%H= 10/1000*ones(1,length(Y))
figure


Ps{1} = [1:8];
Ps{2} = [9:16];
Ps{3} = [17:24];
Ps{4} = [25:32];
Ps{5} = [33:37];
% for i = 1:5
%     plot(P(Ps{i}),d(Ps{i}),'o-')
```

```
%     hold on
% end
% hold off



%E= xlsread('PCdata.xlsx','sheet5')
Ed = 5e-6*100;
Ez = 8e-6*100;
Ep = (5/14.7)*760;
Ey_f = sqrt((Ez./d).^2+(Ed./d).^2 + (Ep./P).^2);
Ey =Ey_f.*Y;

colors = [
0,0,0;
0.7,0,0;
0,0.7,0;
0,0,0.6;
0.7,0.7,0;
];

sym = {'o','d','x','*','>'};
for i = 1:5
p1 = plot(X(Ps{i}),Y(Ps{i}),[sym{i},'-'])
set(p1,'color',colors(i,:))
leg{i} = num2str(round(mean(P(Ps{i}))/760*101.325e3/1e3));
hold on
end



legend(leg,2)
set(gca,'fontsize',13)
for  i = 1:5
p1 = herrorbar(X(Ps{i}),Y(Ps{i}),Ey(Ps{i}),sym{i})
hold on
set(p1,'color',colors(i,:))
p1 = errorbar(X(Ps{i}),Y(Ps{i}),H(Ps{i}),sym{i})
set(p1,'color',colors(i,:))
end
hold off

title('Paschen Curves for Various Pressures (kPa)')
% errorbar(X,Y,'xb')
% figure
% loglog (X,Y,'o')
% set (gca, 'fontsize', 14)
xlabel ('Pd (torr-cm)')
ylabel ('Vb (kV)')
set(gca,'xscale','log')
set(gca,'yscale','log')

xlim([.1,10000])
```

Figure 32 Voltage Current at 0.345 MPa

```
clear
clc
close all

A1=xlsread('0.345MPa.xlsx','sheet1a');
S1= 1:length(A1);
B1=xlsread('0.345MPa.xlsx','sheet1b');

A2=xlsread('0.345MPa.xlsx','sheet2a');
B2=xlsread('0.345MPa.xlsx','sheet2b');
S2= 1:length(A2);

A3=xlsread('0.345MPa.xlsx','sheet3a');
B3=xlsread('0.345MPa.xlsx','sheet3b');
S3= 1:length(A3);

A4=xlsread('0.345MPa.xlsx','sheet4a');
B4=xlsread('0.345MPa.xlsx','sheet4b');
S4= 1:length(A4);

Gaps = [50,100,150,200];
Pressure = 0.69;

Cur = [0:0.1:5];
As = {A1,A2,A3,A4};
Bs = {B1,B2,B3,B4};
Ss = {S1,S2,S3,S4};


cols = {'ro','gd','b<','k*'}

figure
for j = 1:length(As)
    A = As{j};
    B = Bs{j};
    S = Ss{j};
    [BreakdownV(j),k] = max(B);
    BreakdownI(j)=A(k);
    [val2,index2] = min(A(S>200));
    index2 = index2+200;
    [val1,index1] = max(A(S<200));
    %plot(S,A,'.',S(index1),A(index1),'o',S(index2),A(index2),'x')
    A_r1 = A(1:index1);
    A_f1 = A(index1:index2);
    A_r2= A(index2:end);
    B_r1 = B(1:index1);
    B_f1 = B(index1:index2);
    B_r2= B(index2:end);
    %plot(A_r1,B_r1,'.',A_f1,B_f1,'.',A_r2,B_r2,'.')
    for i = 1:length(Cur)
```

```
        Cur1 = Cur(i);
        Tolerance = 0.1;
        inds_f = find(abs(A_f1-Cur1)<Tolerance);
        inds_r = find(abs(A_r2-Cur1)<Tolerance);

        Cur_f(i) = mean(A_f1(inds_f));
        Cur_f_std(i) = std(A_f1(inds_f));
        Vol_f(i) = mean(B_f1(inds_f));
        Vol_f_std(i) = std(B_f1(inds_f));

        Cur_r(i) = mean(A_r2(inds_r));
        Cur_r_std(i) = std(A_r2(inds_r));
        Vol_r(i) = mean(B_r2(inds_r));
        Vol_r_std(i) = std(B_r2(inds_r));
    end
    NormV1(j)=mean(Vol_r(Cur_r>3.8&Cur_r<4.4));
    NormV1_std(j)=std(Vol_r(Cur_r>3.8&Cur_r<4.4));
    NormV2(j)=mean(Vol_f(Cur_f>3.8&Cur_f<4.4));
    NormV2_std(j)=std(Vol_f(Cur_f>3.8&Cur_f<4.4));
    %hold on
    %errorbar(Cur_f,Vol_f,Vol_f_std,'go')
    %errorbar(Cur_r,Vol_r,Vol_r_std,'ro')
    errorbar(Cur_f,Vol_f,Vol_f_std,[cols{j},':'])
    hold on
    errorbar(Cur_r,Vol_r,Vol_r_std,[cols{j},'-'])
    Leg{2*j-1} = [num2str(Gaps(j)),'\mum >>']
    Leg{2*j} = [num2str(Gaps(j)),'\mum <<']
end

legend(Leg)
set(gca,'fontsize',16)
xlabel('Current (mA)')
ylabel('Voltage (kV)')

for j = 1:length(As)
    plot(0,BreakdownV(j),cols{j})
    hold on
end
xlim([-0.1,5])
ylim([0,6.5])

figure

NormVoltage = round((1e3*(NormV1+NormV2)/2)/5)*5 % units volts
pc = polyfit(Gaps,NormVoltage,1);
Efield = pc(1)*1e9 % units V/m
StdNorm = NormV2_std+NormV1_std;
errorbar(Gaps,NormV1,2*NormV1_std)
hold on
errorbar(Gaps,NormV2,2*NormV2_std)
plot(Gaps,BreakdownV)
xlim([0,max(Gaps)])
```

Figure 33 Voltage Current at 0.689 MPa

```
clear
clc
close all

A1=xlsread('0.69MPa.xlsx','sheet1a');
S1= 1:length(A1);
B1=xlsread('0.69MPa.xlsx','sheet1b');

A2=xlsread('0.69MPa.xlsx','sheet2a');
B2=xlsread('0.69MPa.xlsx','sheet2b');
S2= 1:length(A2);

A3=xlsread('0.69MPa.xlsx','sheet3a');
B3=xlsread('0.69MPa.xlsx','sheet3b');
S3= 1:length(A3);

A4=xlsread('0.69MPa.xlsx','sheet4a');
B4=xlsread('0.69MPa.xlsx','sheet4b');
S4= 1:length(A4);

Gaps = [50,100,150,200];
Pressure = 0.69;

Cur = [0:0.1:5];
As = {A1,A2,A3,A4};
Bs = {B1,B2,B3,B4};
Ss = {S1,S2,S3,S4};


cols = {'ro','gd','b<','k*'}

figure
for j = 1:length(As)
    A = As{j};
    B = Bs{j};
    S = Ss{j};
    [BreakdownV(j),k] = max(B);
    BreakdownI(j)=A(k);
    [val2,index2] = min(A(S>200));
    index2 = index2+200;
    [val1,index1] = max(A(S<200));
    %plot(S,A,'.',S(index1),A(index1),'o',S(index2),A(index2),'x')
    A_r1 = A(1:index1);
    A_f1 = A(index1:index2);
    A_r2= A(index2:end);
    B_r1 = B(1:index1);
    B_f1 = B(index1:index2);
    B_r2= B(index2:end);
    %plot(A_r1,B_r1,'.',A_f1,B_f1,'.',A_r2,B_r2,'.')
    for i = 1:length(Cur)
```

```
        Cur1 = Cur(i);
        Tolerance = 0.1;
        inds_f = find(abs(A_f1-Cur1)<Tolerance);
        inds_r = find(abs(A_r2-Cur1)<Tolerance);

        Cur_f(i) = mean(A_f1(inds_f));
        Cur_f_std(i) = std(A_f1(inds_f));
        Vol_f(i) = mean(B_f1(inds_f));
        Vol_f_std(i) = std(B_f1(inds_f));

        Cur_r(i) = mean(A_r2(inds_r));
        Cur_r_std(i) = std(A_r2(inds_r));
        Vol_r(i) = mean(B_r2(inds_r));
        Vol_r_std(i) = std(B_r2(inds_r));
    end
    NormV1(j)=mean(Vol_r(Cur_r>3.8&Cur_r<4.4));
    NormV1_std(j)=std(Vol_r(Cur_r>3.8&Cur_r<4.4));
    NormV2(j)=mean(Vol_f(Cur_f>3.8&Cur_f<4.4));
    NormV2_std(j)=std(Vol_f(Cur_f>3.8&Cur_f<4.4));
    %hold on
    %errorbar(Cur_f,Vol_f,Vol_f_std,'go')
    %errorbar(Cur_r,Vol_r,Vol_r_std,'ro')
    errorbar(Cur_f,Vol_f,Vol_f_std,[cols{j},':'])
    hold on
    errorbar(Cur_r,Vol_r,Vol_r_std,[cols{j},'-'])
    Leg{2*j-1} = [num2str(Gaps(j)),'\mum >>']
    Leg{2*j} = [num2str(Gaps(j)),'\mum <<']
end

legend(Leg)
set(gca,'fontsize',16)
xlabel('Current (mA)')
ylabel('Voltage (kV)')

for j = 1:length(As)
    plot(0,BreakdownV(j),cols{j})
    hold on
end
xlim([-0.1,5])
ylim([0,6.5])

figure

NormVoltage = round((1e3*(NormV1+NormV2)/2)/5)*5 % units volts
pc = polyfit(Gaps,NormVoltage,1);
Efield = pc(1)*1e9 % units V/m
StdNorm = NormV2_std+NormV1_std;
errorbar(Gaps,NormV1,2*NormV1_std)
hold on
errorbar(Gaps,NormV2,2*NormV2_std)
plot(Gaps,BreakdownV)
xlim([0,max(Gaps)])
```